UNIVERSITÀ DI SIENA 1240

Department of Biotechnology, Chemistry and Pharmacy

Research Doctoral School in

Biochemistry and Molecular Biology-BiBiM 2.0

Cycle: 37°

Title:

STUDY OF EFFECTS OF GLYCAEMIC AND PHARMACOLOGICAL TREATMENT IN DIFFERENT CELL LINES

GEMMA SARDELLI

SUPERVISOR: Professor Roberta Moschini

Academic Year: 2024-25

Table of Contents

ABSTRACT

The Aldo-Keto Reductase (AKR) superfamily comprises a group of enzymes which contributes to detoxify reactive aldehydes and ketons produced during oxidative process and exposure to xenobiotics. These compounds include sugar aldehydes, keto-steroids, keto-prostaglandins, retinals, quinones, and lipid peroxidation products. Due to their central role in detoxification, AKRs are associated with various pathological conditions, including:

-Diabetes mellitus, where AKR1B1 is involved in the development of diabetic complications.

-Cancer, with several AKRs differently expressed in various tumours that may contribute to resistance to chemotherapeutic drugs.

A typical feature of diabetes is the elevated blood glucose level (referred as hyperglycemia), which is known to induce a series of metabolic alterations, particularly on insulin independent tissues. Among all the AKR enzymes, AKR1B1 is the most studied because of its pivotal role in mediating hyperglycemic injury and in the development of secondary diabetic complications. Specifically, AKR1B1 promotes inflammation throughs the products of its enzymatic activity on 3-glutathionyl-4-hydroxynonanal (GS-HNE), namely the 3-glutathionyldihydroxynonane (GS-DHN). Moreover, AKR1B1 represents the first enzymes of polyol pathway, an alternative metabolic route of glucose which leads to sorbitol and fructose accumulation in cells under hyperglycemic conditions. Therefore, its inhibition has been proposed as a potential strategy to counteract inflammation and other complications associated with diabetes. Here, the pharmacological inhibition of AKR1B1 has been tested, in order to elucidate its role in inflammation, at the basis of diabetic complications.

On the other hand, AKRs together with oxidoreductase enzymes, participated in phase 1 metabolism of endogenous compounds and xenobiotics bearing carbonylic groups, which are converted to their corresponding alcohol metabolites. Specifically, AKR1A1, AKR1B10, AKR1C3 along with another NADPH-dependent reductase, carbonyl reductase (CBR1), are known for their detoxifying action against a class of chemotherapeutic compounds (e.g. anthracyclines) and consequently associated with chemotherapeutic resistance in cancer. The alcoholic derivative of anthracyclines, indeed, shows reduced cytotoxicity probably due to

a better expulsion from the cells, and is also associated with cardiotoxicity. In this study, the inhibition of these enzymes has been investigated, aiming to enhance the therapeutic efficacy of anthracyclines and simultaneously minimizing side effects.

Finally, the establishment of a novel daunorubicin-resistant cell line has provided the opportunity to investigate the oxidoreductase profile and resistance mechanisms employed by these resistant cells, revealing significant differences in AKR expression and activity compared to non-resistant cells.

CHAPTER 1: INTRODUCTION

1.1 Oxidative stress and antioxidant defence

Cells possess intricate biochemical mechanisms to maintain an appropriate balance between oxidant species and antioxidant defenses, and disruptions in this balance can have significant pathophysiological consequences. Oxidative stress, defined as a relative excess of oxidant species compared to antioxidants, has been implicated in the pathogenesis of neurodegenerative diseases, cardiovascular diseases, diabetes mellitus, and cancer[1][2].

The primary source of oxidative stress originates from mitochondria, where molecular oxygen is reduced to water during aerobic respiration, a crucial process for coping with the cellular energy demands [3]During electron transport through the mitochondrial electron transport chain (ETC), electron leakage can occur, leading to the generation of reactive molecules. Superoxide anion ($O_2^{\bullet -}$) and hydrogen peroxide (H_2O_2) are the most common reactive oxygen species (ROS), being normal by-products of various enzymatic and metabolic reactions. However, more reactive and harmful species, such as the hydroxyl radical ($OH^{\bullet}$) and hydroperoxide radical ($HO_2^{\bullet}$), can also form under certain conditions. In addition to ROS, reactive nitrogen species (RNS), including nitric oxide ($NO^{\bullet}$) and peroxynitrite anion ($ONOO^-$), are produced within cells and may contribute to oxidative stress [4][5].

While H_2O_2 and $NO^{\bullet}$ serve essential roles as signalling molecules, highly reactive species such as $OH^{\bullet}$, $O_2^{\bullet -}$ and $ONOO^-$ can oxidize intracellular macromolecules, including polyunsaturated fatty acids (PUFAs) in cell membranes, proteins, and nucleic acids[6]. Oxidation of PUFAs by ROS leads to lipid peroxidation, with peroxidized PUFAs and their degradation products - particularly 4-hydroxy-2-nonenal (4-HNE), 4-oxonon-2-enal (4-ONE), and malondialdehyde (MDA) - disrupting membrane permeability, interacting with other biomolecules, and functioning as signalling molecules that stimulate inflammation, apoptosis, or ferroptosis[7]. The reaction of reactive species with proteins results in protein oxidation, formation of covalent adducts, and peptide bond rupture, thereby altering protein function. When present in the nucleus, reactive species can damage DNA, causing base oxidation and double-strand breaks, which contribute to genomic instability.

To prevent the accumulation of ROS and mitigate the damaging effects described above, cells employ a broad spectrum of antioxidant systems. Non-catalytic small molecules that directly scavenge ROS and RNS include α-lipoic acid, reduced glutathione (GSH), thioredoxin, vitamin E, vitamin C, β-carotene, and polyphenols [8]. Among these, GSH is particularly noteworthy, and its synthesis is tightly regulated to maintain homeostasis. It can be synthesized de novo or regenerated from its oxidized form via the catalytic action of glutathione reductase (GSR), an enzyme that belongs to the antioxidant enzyme family [9]. Other enzymes involved in antioxidant defence consist of cytosolic or mitochondrial enzymes specifically designed to reduce or eliminate ROS reactivity. Enzymes that detoxify $O_2^{\bullet-}$ include the cytosolic copper/zinc superoxide dismutase (SOD1), mitochondrial manganese SOD (SOD2), and extracellular SOD (SOD3), all of which catalyse the conversion of $O_2^{\bullet-}$ to H_2O_2 and O_2 [10]. Subsequently, other enzymes detoxify H_2O_2, such as catalase (CAT), which converts H_2O_2 into water and oxygen [11], as well as peroxiredoxins (PRDXs) and glutathione peroxidases (GPXs), which reduce H_2O_2 to H_2O using reducing equivalents from thioredoxin and GSH, respectively [12], [13]. Oxidized thioredoxin is ultimately regenerated by thioredoxin reductase (**Figure 1**).

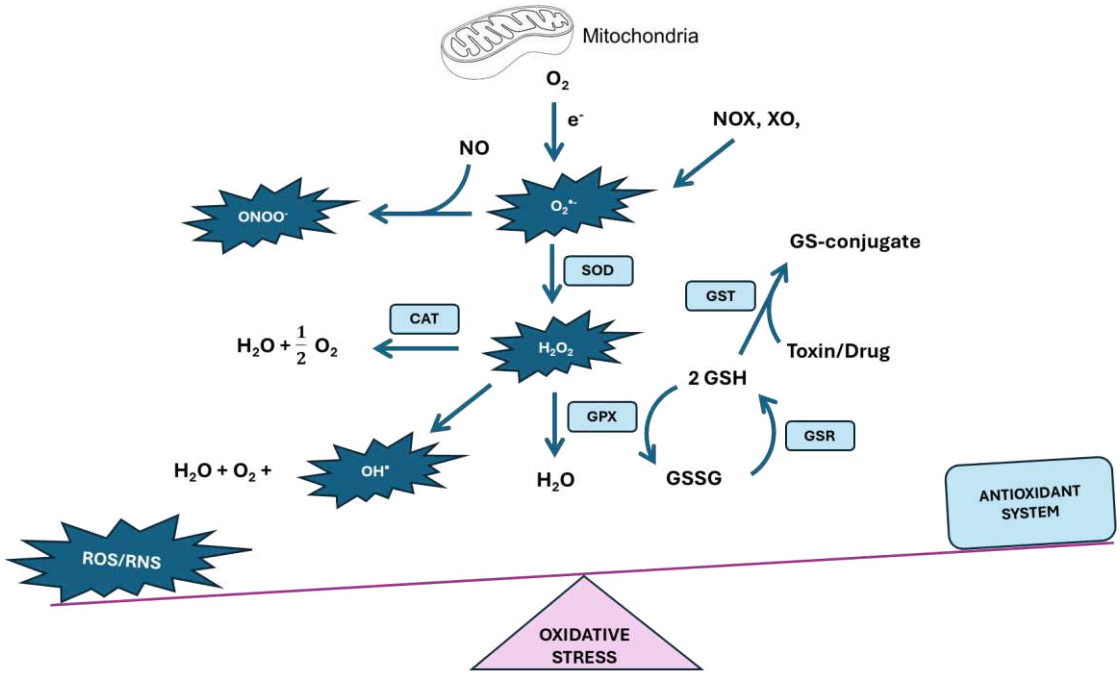

***Figure 1*. The major oxidant and antioxidant systems.** Figure modified from Liu *et al*., 2023 [62].

Additionally, certain enzymes involved in drug metabolism also provide indirect antioxidant defence. These enzymes play key roles in detoxifying xenobiotics and contribute to the broader cellular antioxidant response.

These include the phase I enzymes, such as the aldehyde dehydrogenase (ALDH) family, the aldo-keto reductase (AKR) family, carbonyl reductases (CBRs), NADPH:quinone oxidoreductases (NQO1 and NQO2), and cytochrome P450 (CYP-450) oxidases, as well as phase II enzymes like the glutathione S-transferase (GST) and acetyltransferase families[14], [15], [16], [17] . Many of these detoxification systems are expressed in cells upon activation of the transcription factor NF-E2-related factor 2 (Nrf2) [18]. Nrf2 regulates both the basal and inducible expression of antioxidant and phase II detoxification enzymes, allowing cells to adapt to varying stress conditions. It binds to specific sequences known as antioxidant response elements (ARE) in the promoter regions of target genes[19]. Nrf2 is constantly present in the cytoplasm but is negatively regulated by the protein Keap1, which acts as the primary stress sensor in this pathway. Under normal conditions, Nrf2 binds to two Keap1 molecules, which serve as a bridge between Nrf2 and the ubiquitin ligase Cullin-3 (Cul3), promoting Nrf2 ubiquitination and subsequent proteasomal degradation. Keap1 contains two reactive cysteine residues that are oxidized in the presence of oxidative stress or electrophiles, leading to a significant conformational change in the protein. As a result, Nrf2 is released from Keap1 and is no longer targeted for ubiquitination, enabling it to translocate to the nucleus and activate the transcription of antioxidant and detoxification genes[20]. The Nrf2 pathway is illustrated in **Figure 2**. Among the enzymes involved in cellular defence against oxidative species, the aldo-keto reductase family plays a crucial role by catalysing the reduction of reactive aldehydes and ketones derived from oxidative processes or external sources. This reduces the reactivity of these compounds, thereby protecting cells from oxidative damage. However, in pathological contexts such as diabetes and cancer, the role of these enzymes can be dual: while they protect cells from oxidative stress, their overexpression may contribute to drug resistance and promote the survival of cancer cells in hostile environments [21].

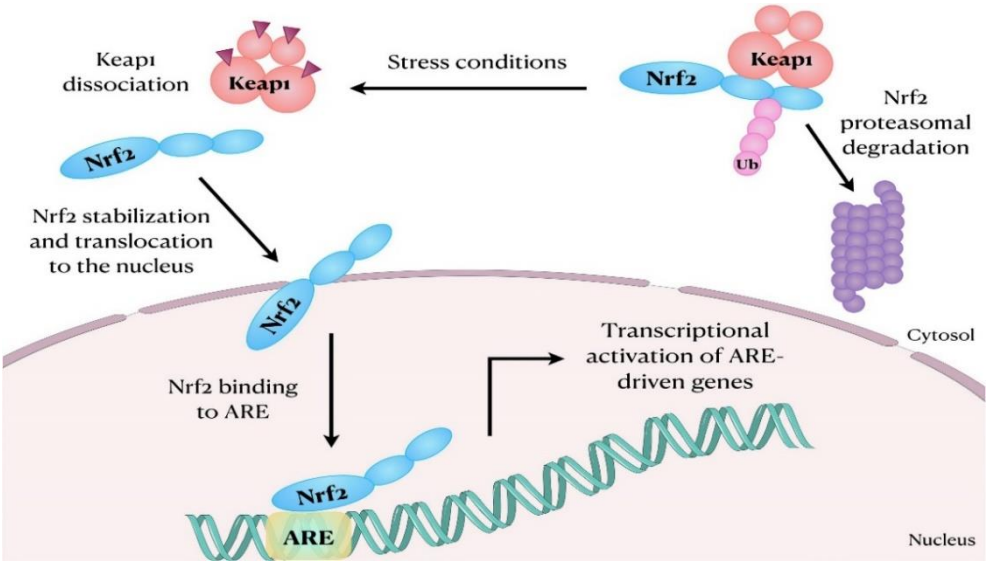

Figure 2. **Nrf2 signalling pathway.** Figure from Seminotti *et al.,* 2021 [246].

1.1.1 The Aldo-Keto Reductase Family 1 (AKR1) Enzymes

The aldo-keto reductase (AKR) superfamily consists of 16 families of monomeric, soluble proteins (~37 kDa) that exhibit NAD(P)H-dependent oxidoreductase activity [15]. These evolutionarily conserved enzymes reduce the carbonyl groups of a wide variety of substrates, including sugar aldehydes, keto-steroids, keto-prostaglandins, retinals, quinones, and products of lipid peroxidation. Structurally, AKRs share a common protein fold, characterised by a central (α/β)8-barrel with the addition of several helices. The β-strands and α-helices are connected by three loops (loops A, B, and C) that play crucial roles in enzyme function. These loops are located at the back of the barrel and determine the specificity of the enzymes. Due to their high flexibility, AKRs can accommodate diverse substrates, conferring them a high degree of functional versatility [22](**Figure 3**).

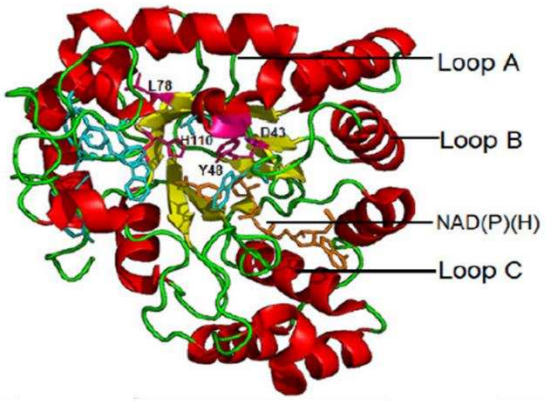

Figure 3. **Structural features of human Aldo-Keto Reductase enzymes.** Figure from Shanbhag and Bhowmik., 2024 [247].

To date, 13 AKR proteins have been identified in humans, 8 of which belong to the AKR1 family, whose key features are summarized in **Table 1**. Despite their sequence similarity, members of the AKR1 family exhibit functional diversity. While AKR1A and AKR1B enzymes are primarily involved in detoxification, AKR1C and AKR1D enzymes play key roles in steroid hormone metabolism[23]. AKR1A1 is predominantly expressed in the liver, and its dysfunction primarily results in alcohol toxicity. This enzyme reduces reactive intermediates such as 3-deoxyglucosone and methylglyoxal, which are involved in glycation reactions[24].

Among the most studied AKRs is AKR1B1, also known as aldose reductase, which plays a crucial role in diabetic pathology as the first enzyme in the polyol pathway (discussed in detail in the following section)[25]. AKR1B1 also reduces glutathione-conjugated carbonyls, specifically glutathione-4-hydroxynonenal (GS-HNE), as well as its unconjugated form, HNE, which is a major product of lipid peroxidation[26]. AKR1B1's activity against GS-HNE leads to the formation of GS-DHN, a signalling molecule involved in the inflammatory response via the NF-κB activation pathway (see **Subsection 1.2.2**) [27].

AKR1B1 shares structural homology with AKR1B10; however, while the former is ubiquitously expressed, AKR1B10 is primarily found in the gastrointestinal tract and adrenal glands[28]. Unlike AKR1B1, AKR1B10 is highly efficient in eliminating free electrophilic carbonyl compounds, as well as dietary-derived carbonyls such as HNE, acrolein, crotonaldehyde, trans-2-hexenal, and trans-2,4-hexadienal [28]. Additionally, AKR1B10 has the ability to convert all-trans-retinaldehyde into retinol, thus playing a key role in regulating the first step of retinoic acid synthesis [29]. Retinoic acid, which is produced through the oxidation of all-trans-

retinaldehyde by aldehyde dehydrogenase enzymes, acts as an antiproliferative and pro-apoptotic molecule, thus exerting potent antitumor effects [30]. Therefore, by promoting retinol formation and opposing retinoic acid production, AKR1B10 is considered a marker of tumour progression and aggressiveness. It is upregulated in many cancer types, particularly in non-small cell lung cancer and colon cancer [31], [32], [33].

The AKR1C enzymes share an 84% amino acid sequence identity with each other [23]. They possess varying ratios of 3-, 17-, and 20-ketosteroid reductase activities, leading to the formation of their respective 3α/β-, 17β-, and 20α-hydroxy-steroids [34]. By catalysing the interconversion of active steroid hormones, such as androgens, estrogens, and progesterone, to their inactive counterparts, AKR1Cs function as molecular switches, regulating the binding and activation of steroid hormone receptors. Except for the liver-specific AKR1C4, the AKR1C1–3 enzymes are expressed in various tissues and participate in diverse biochemical processes [35]. These enzymes are believed to be involved in the development of hormone-dependent cancers, including breast cancer, prostate cancer, and endometrial cancer, as well as hormone-independent cancers and other diseases such as endometriosis, depressive disorders, premenstrual syndrome, and epilepsy[36], [37], [38], [39], [40]. Lastly, AKR1D1 is highly expressed in the human liver, where it generates all 5β-reduced dihydrosteroid metabolites for C19, C21, and C27 steroids, including androgens, glucocorticoids, and bile acids, although much of its role remains to be clarified [41].

AKRs are also linked to resistance against several major classes of chemotherapeutic agents, including anthracyclines, cisplatin, cyclophosphamide, methotrexate, mitomycin, and vinca alkaloids[42]. This resistance arises due to the AKR-catalysed metabolism of chemotherapeutic drugs and steroid hormones, or due to the need to eliminate drug-induced cellular stress caused by electrophiles or ROS. Moreover, drug-induced cellular stress activates the Nrf2/Keap1 pathway, leading to a feed-forward stimulation of AKRs expression[43]. Consistently, AKR upregulation in many tumours is associated with chemoresistance. In this context, pan-AKR inhibitors could be useful in overcoming drug resistance. The role of these enzymes in anthracycline metabolism will be discussed in detail in the following sections.

Gene	Protein	Distribution	Physiological role	natural substrates	Ref
AKR1A1	Aldehyde reductase	Kidney, Liver, Stomach	Energy metabolism; redox homeostasis and detoxification	Carboxyl-group containing negatively charged substrates; aromatic aldehydes, steroid aldehydes, and small 3-carbon aldehydes	[44]
AKR1B1	Aldose reductase	Liver, Muscle, Kidney, Eyes	redox homeostasis and detoxification; polyol pathway	Glucose, AGE precursors, lipid peroxidation products, glutathione conjugates of unsaturated aldehydes	[45]
AKR1B10	Small intestine aldose reductase	Small intestine, colon, adrenal gland, Eyes	Redox homeostasis and detoxification; retinoid metabolism; isoprenoid metabolism	AGE precursors, lipid peroxidation products; all-trans retinal; farnesal and geranylgeranial	[28]
AKR1C1	Hydroxysteroid dehydrogenases	Small intestine, Lung, Mammary Gland, Prostate	Estrogen metabolism; reduction of 20-ketosteroid	Progesterone	[46]
AKR1C2	Bile-acid binding protein	Small intestine, Lung, Mammary gland, Prostate	Transport of bile acids; reduction of 3-ketosteroid	5α-dihydrotestosterone	[47]
AKR1C3	Prostaglandin F synthase	Small intestine, Lung, Mammary gland, Prostate	Prostaglandins biosynthesis; reduction of 17-ketosteroid	Prostaglandins H_2 and D_2; estrone/estradiol, androstenedione/estosterone	[48]
AKR1C4	Chlordecone reductase	Liver specific	Reduction of 3-ketosteroid; hepatic clearance of steroids	5α-pregnane-3,20-dion	[49]
AKR1D1	5β-reductase	Liver specific	Bile acid synthesis; degradative metabolism of sex hormones	Δ4-3 ketosteroids; testosterone, progesterone, cortisol and cortisone	[50]

***Table 1*. Human AKR- family 1 proteins.**

1.1.2 Carbonyl reductases (CBR) family.

Another class of enzymes involved in carbonyl reduction is the Carbonyl Reductase (CBR) family, which belongs to the short-chain dehydrogenase/reductase (SDR) superfamily. Three SDR carbonyl reductases have been identified in humans: carbonyl reductase 1 (CBR1), carbonyl reductase 3 (CBR3), and carbonyl reductase 4 (CBR4) [51]. These enzymes are monomeric, NADPH-dependent oxidoreductases that metabolize a wide range of endogenous and exogenous carbonyl-containing compounds, including aflatoxins, prostaglandins, and steroids [52]. Classified as phase I biotransformation enzymes, CBRs catalyse the conversion

of carbonyl groups to alcohol, increasing their water solubility and facilitating their elimination from the body, either directly or via conjugation reactions [51], [52].

While CBR1 and CBR3 are cytoplasmic, sharing similar three-dimensional structures and functions, CBR4 is located in the mitochondria and has low sequence identity (<30%) with the other CBRs [53]. CBRs contain a conserved Rossmann fold, which is involved in cofactor binding, and the region with the least homology is the C-terminal part, likely contributing to substrate specificity [54].

CBRs metabolize a broad spectrum of substrates, generally leading to detoxification or inactivation of chemically reactive carbonyl groups. Among the three human carbonyl reductases, CBR1 is the most studied and characterised. Its reductase activity targets a variety of substrates, including eicosanoids, steroids, lipid peroxidation-derived carbonyl compounds, and ortho- or para-xenobiotic quinone derivatives[55]. Immunohistochemical staining has revealed the presence of CBR1 in all investigated organs [56], indicating its vital role in the metabolism of endogenous carbonyl substrates. However, the highest concentrations of the enzyme are observed in tissues exposed to exogenous compounds, such as the liver, gastrointestinal tract epithelium, and epidermis, suggesting its involvement in xenobiotic detoxification[55]. CBR1 is particularly efficient in catalysing the reduction of glutathionylated aldehydes, supported by the presence of the GSH binding site. Specifically, CBR1 efficiently metabolizes 3-glutathionyl-4-hydroxynonenal (GS-HNE), functioning both as a dehydrogenase on the hemiacetal hydroxyl group, and as a reductase on the free aldehyde group. This results in the production of 3-glutathionyl-4-hydroxynonanoic-γ-lactone (GSHNA-lactone), which is ready for cellular extrusion, and 3-glutathionyl-1,4-dihydroxynonane (GS-DHN), a pro-inflammatory signalling molecule[57]. Other glutathionylated substrates of CBR1 include S-nitrosoglutathione (GSNO) and glutathionyl-2-trans-nonenal (GSNA) [57], [58].

Oxidative stress in the brain is a major cause of neurodegenerative disorders, as the brain is rich in PUFA, which are highly susceptible to lipid peroxidation. This has been linked to diseases such as Alzheimer's and Parkinson's. Given its central role in metabolizing reactive aldehydes derived from lipid peroxidation, CBR1 is crucial for neuronal survival and protects against oxidative stress-induced neurodegeneration [59], [60].

Finally, CBR1 is of clinical interest due to its prominent role in the metabolism of anthracyclines, which will be discussed in detail in **Section 1.3**.

1.2 High glucose

Under normal conditions, blood glucose concentration is approximately 80 mg/dl (normoglycemia), and it is maintained within this range through the actions of glucose-regulating hormones such as insulin and glucagon. After a meal, blood glucose levels rise significantly, triggering insulin production by pancreatic β-cells. Insulin acts on insulin-dependent tissues, such as skeletal muscle and adipose tissue, promoting the translocation of glucose transporters, particularly GLUT4, to the cell membrane. This allows glucose to enter cells, thereby lowering blood glucose levels. Insulin-independent tissues, on the other hand, consist of cells that do not require insulin for glucose uptake as they possess constitutively expressed GLUT1 and GLUT2 transporters in their membranes [61]. The major insulin-independent tissues include nervous tissue, intestinal epithelium, liver, kidney, retinal tissue, and lens cells. In these cells, persistent hyperglycemia leads to intracellular glucose accumulation. Elevated glucose levels activate multiple pathways, each contributing to ROS accumulation until the occurrence of authentic oxidative stress. The primary glucose metabolic pathway is glycolysis, particularly aerobic glycolysis, which serves as the main source of ATP in most human tissues. Under normal conditions, ROS production due to electron leakage from ETC is mitigated by the antioxidant defence systems. However, the higher the glucose level, the higher the rate of aerobic glycolysis, increasing the ETC load. Consequently, more superoxide is produced, saturating the cell's antioxidant defences [62].

Additionally, the accumulation of glycolytic intermediates, due to hyperactivation of glycolysis under hyperglycemic conditions, may be shunted into alternative pathways, ultimately contributing to oxidative stress (**Figure 4**) [63]. Specifically, the accumulation of fructose-6-phosphate and glyceraldehyde-3-phosphate can activate the hexosamine pathway and protein kinase C (PKC) pathway, respectively[64]. The hexosamine pathway begins with the conversion of the glycolytic intermediate fructose-6-phosphate to glucosamine-6-phosphate via a rate-limiting enzyme, glutamine-fructose-6-phosphate amidotransferase. After several enzymatic steps, the final key metabolite of this pathway, UDP-N-acetylglucosamine (UDP-NAcGlcNH2), is produced, which can bind to proteins through O-linked glycosylation. This post-translational modification alters protein structure and function, leading to glycative stress[64].

Furthermore, increased glycolysis results in a higher availability of glyceraldehyde-3-phosphate, a triose that can be reduced to glycerol-3-phosphate for diacylglycerol (DAG) synthesis. DAG is a potent activator of PKC, a family of serine/threonine kinases that regulates numerous cellular responses. Elevated PKC activity has been linked to the activation of ROS-generating enzymes such as NADPH oxidases and lipoxygenases, further exacerbating oxidative stress [65]. Glucose can also undergo less quantitatively significant transformations, which are enhanced in hyperglycemia and closely linked to ROS production. Glucose autooxidation, resulting from its accumulation in cells, leads to the formation of glyoxal, a precursor to advanced glycation end products (AGEs), contributing to cellular oxidative stress.

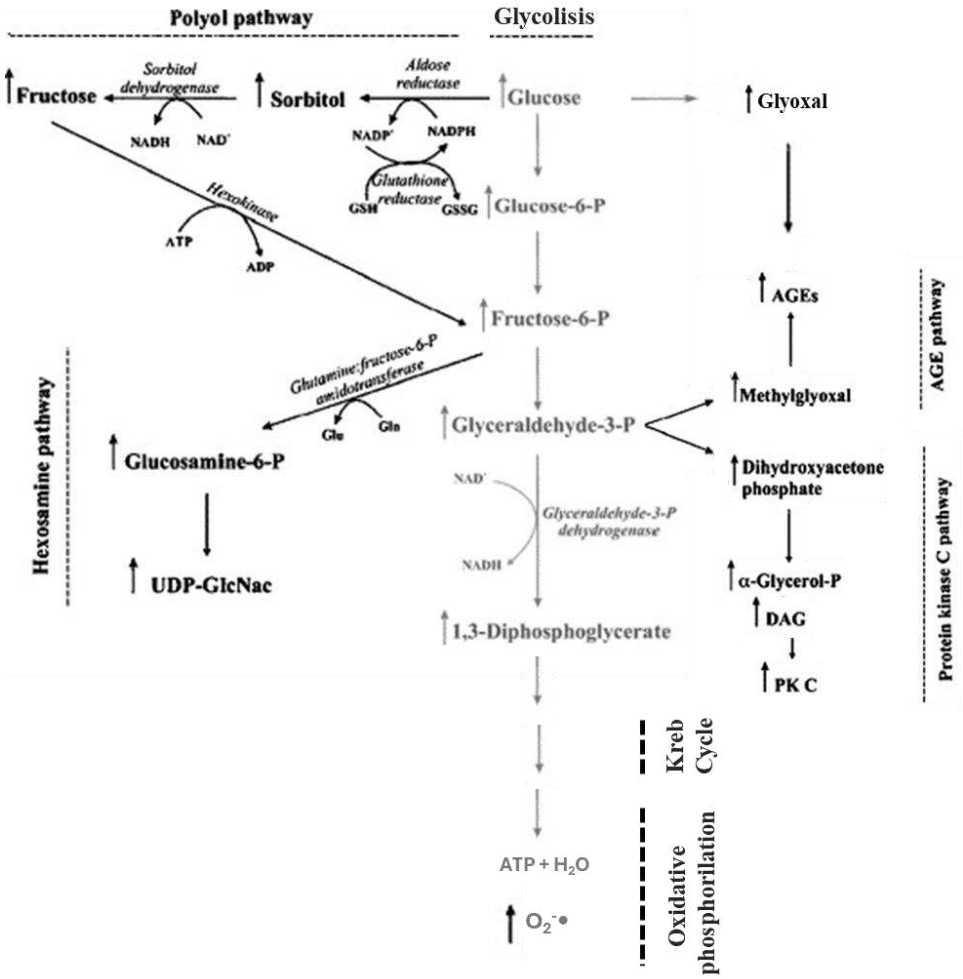

***Figure 4*. Mechanisms of hyperglycemia-induced damage**. Modified figure from Rolo and Palmeira, 2006 [248].

Glyoxal and other precursors interact with proteins to form AGEs, which, once formed, can bind to AGE receptors (RAGE) or abnormally interact with components of the extracellular matrix, further promoting ROS generation and oxidative stress [63]. Other AGE precursors include

methylglyoxal and 3-deoxyglucosone, derived from the non-enzymatic dephosphorylation of the triose phosphates glyceraldehyde-3-phosphate and dihydroxyacetone phosphate or from the breakdown of glucose-derived 1-amino-1-deoxyfructose lysine adducts, known as Amadori products [66].

Another glucose-related pathway of significance in hyperglycemic conditions is the polyol pathway.

1.2.1 Polyol pathway

The polyol pathway plays a minimal role in glucose metabolism under normoglycemic conditions, primarily due to the low affinity of AKR1B1, the first enzyme in the pathway, for glucose, with a very high K_m (50-100 mM, [67]) for this substrate. Under normal conditions, only about 3% of glucose is metabolized through this route. However, in hyperglycemia, the activity of the polyol pathway increases significantly, accounting for up to 30% of intracellular glucose [68]. As a result, this pathway becomes one of the most important collateral routes for glucose metabolism in hyperglycemia, and it is considered a key mechanism in the development of oxidative stress and subsequent diabetic complications. As shown in **Figure 5**, the polyol pathway involves two enzymatic reactions: first, glucose is reduced to sorbitol by AKR1B1, using NADPH as a cofactor. Sorbitol is then oxidized to fructose by the enzyme sorbitol dehydrogenase (SDH) in an NAD^+-dependent reaction [69].

Sorbitol is a polyol, meaning it contains multiple hydroxyl groups, giving it high hydrophilicity. Due to its polarity, sorbitol cannot freely cross biological membranes, leading to its accumulation in the cytoplasm, where it attracts water molecules, causing osmotic stress. The second step of the pathway produces fructose, which can be phosphorylated to fructose-6-phosphate and re-enter the glycolytic pathway or participate in the hexosamine pathway. This occurs particularly in tissues expressing hexokinase isoforms I-III, which can phosphorylate

fructose, albeit less efficiently than glucose [70]. Ultimately, the fructose generated through this process contributes to both glycative and oxidative stress[71].

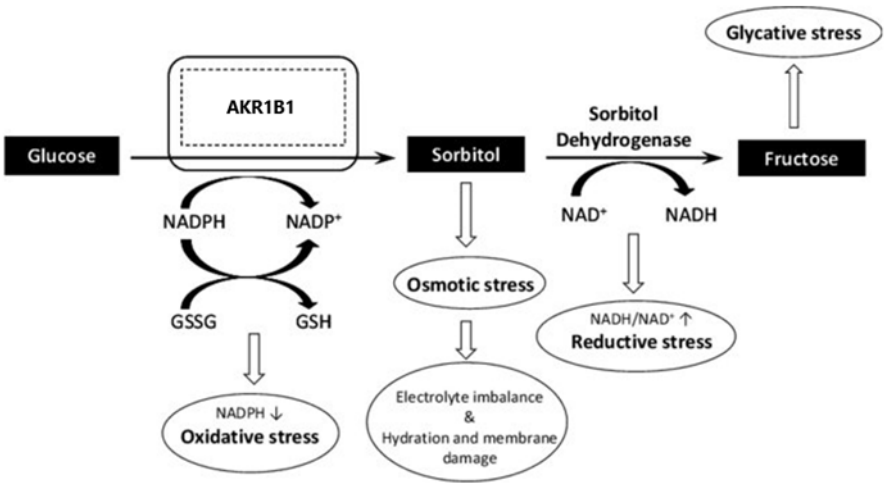

Figure 5. **The polyol pathway and associated stress**. Figure from Grewal *et al.,* 2016 [164].

It is important to note that both reactions in the polyol pathway depend on pyridine nucleotide cofactors. Consequently, these reactions decrease the cytosolic NADPH/$NADP^+$ ratio while increasing the NADH/NAD^+ ratio. NADH promotes oxidative stress by generating reactive oxygen species (ROS) via the overloading of the mitochondrial ETC, as previously described. Furthermore, the depletion of NADPH reduces the levels of GSH, as NADPH is an essential cofactor for glutathione reductase in the reduction of oxidized glutathione (GSSG). This further exacerbates oxidative stress in cells under hyperglycemic conditions [69]. In summary, oxidative, osmotic, and glycative stress increase within cells, culminating in a strong state of inflammation, which underlies the development of diabetic complications. Blocking the entry of glucose into the polyol pathway is therefore considered a potential strategy for mitigating the harmful effects of this pathway. As the first enzyme in the pathway, AKR1B1 is a critical pharmacological target in efforts to prevent diabetic complications. Numerous AKR1B1 inhibitors are currently under investigation, including Sorbinil, Tolrestat, Fidarestat, and Epalrestat, but none have been approved for clinical use due to their side effects and limited clinical efficacy[69].

1.2.2 Inflammatory response

High glucose levels induce oxidative, osmotic, and glycative stress in cells, culminating in a significant inflammatory state that drives the development of diabetic complications. This inflammatory process is primarily regulated by the transcription factor nuclear factor kappa-light-chain-enhancer of activated B cells (NF-κB) [72].

In humans, the NF-κB superfamily consists of five transcription factors that mediate the transcription of target genes by binding to a specific DNA element known as the κB enhancer, forming various hetero- or homodimers. These factors are generally classified into two subfamilies: the NF-κB subfamily (p50 and p52) and the Rel subfamily (RelA, RelB and c-Rel), with their structural organization outlined in **Figure 6** [73].

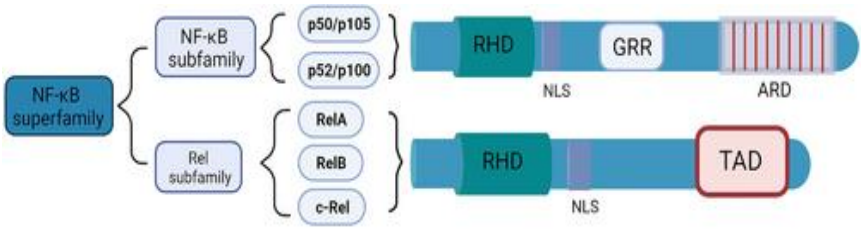

Figure 6. **Schematic structures of nuclear factor of κ-light chain of enhancer-activated B cells (NF-κB) superfamily members.** Figure from Zhang *et al*., 2021 [73].

Under normal conditions, NF-κB proteins are sequestered in the cytoplasm by a family of inhibitory proteins, including IκB family members. NF-κB activation occurs via two main signalling pathways: the canonical and noncanonical pathways, both essential for regulating immune and inflammatory responses, despite their differing signalling mechanisms (**Figure 7**). The primary mechanism for canonical NF-κB activation involves the inducible degradation of IκBα, which is triggered through site-specific phosphorylation by a multi-subunit IκB kinase (IKK) complex. IKK can be activated by various stimuli, including cytokines, growth factors, mitogens, microbial components, and stress agents. Upon activation, IKK phosphorylates IκBα at two N-terminal serine residues, leading to ubiquitin-dependent degradation of IκBα in the

proteasome. This degradation allows for the rapid and transient nuclear translocation of canonical NF-κB members, primarily the p50/RelA and p50/c-Rel dimers[74].

Unlike the canonical pathway, noncanonical NF-κB activation does not involve IκBα degradation but instead relies on processing the p52 precursor protein, p100. A central molecule in this pathway is NF-κB-inducing kinase (NIK), which activates and cooperates with IKKα to mediate p100 phosphorylation, resulting in p100 maturation. This maturation involves degradation of the C-terminal IκB-like domain, generating the mature p52 protein and enabling nuclear translocation of the noncanonical NF-κB complex, particularly the p52/RelB dimer [74]. Functionally, the canonical NF-κB pathway is involved in almost all aspects of immune responses, while the noncanonical pathway serves as a supplementary axis, cooperating with the canonical pathway to regulate specific functions of the adaptive immune system[74].

Once in the nucleus, NF-κB interacts with the promoters of target genes to enhance their transcription. To date, more than 400 different genes have been identified as regulated by NF-κB binding sequences, including those coding for inflammatory cytokines (e.g., TNF-α, IL-1, IL-6), chemokines, adhesion molecules, viral proteins, telomerase, angiogenesis factors (e.g., VEGF), anti-apoptotic proteins, cell cycle-regulatory genes, and inflammatory enzymes such as 5-lipoxygenase (5-LOX) and cyclooxygenase-2 (COX-2) [75].

Regarding hyperglycemia, all the molecular pathways activated in the presence of high glucose levels ultimately lead to the activation of NF-κB signalling, contributing to inflammation. PKC plays a crucial role in the activation of inflammation. PKC can directly phosphorylate and activate the IKK complex, which in turn phosphorylates IκB-α, leading to its degradation and allowing NF-κB nuclear translocation [76]. Lipid peroxidation products generated in response to elevated glucose levels can also activate PKC and promote NF-κB activation. For instance, the glutathionylated derivative of HNE, GS-HNE, is converted to GS-DHN, which is considered a key molecule in inflammatory signal transduction through activation of the kinase cascade and NF-κB. Furthermore, the formation of AGEs and their binding to receptors trigger a series of signalling cascades, including the phosphorylation of p38 MAPK, leading to enhanced NF-κB signalling [77].

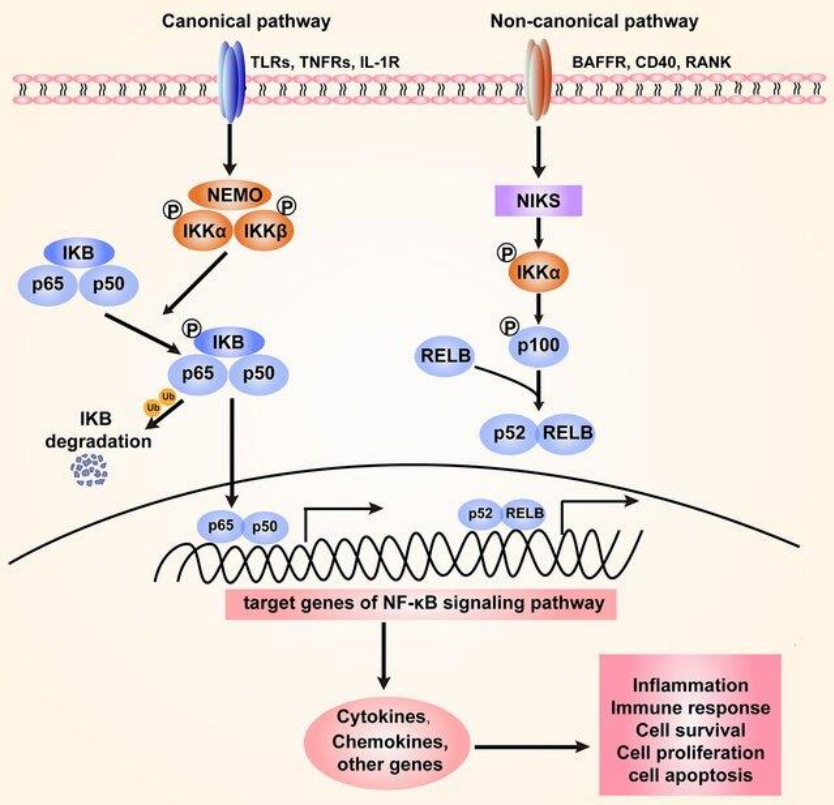

***Figure 7*. The canonical and non-canonical NF-κB signalling pathway.** Figure from Peng *et al*., 2020 [249].

1.2.3 Diabetes and complications

Diabetes mellitus (DM) is a metabolic disorder characterised by persistently elevated blood glucose levels, a condition known as hyperglycemia. The primary subtypes of DM are Type 1 diabetes mellitus (T1DM) and Type 2 diabetes mellitus (T2DM), which arise from defective insulin secretion by pancreatic β-cells and impaired insulin action on target tissues, respectively[78]. T1DM typically manifests in children or adolescents, while T2DM is more common in middle-aged and older adults, often resulting from prolonged hyperglycemia due to unhealthy lifestyle and dietary choices. The pathogenesis of T1DM and T2DM differs significantly; T1DM is marked by the autoimmune destruction of pancreatic beta cells, whereas T2DM involves a complex interplay of genetic and environmental factors, characterised by an imbalance between insulin secretion and insulin sensitivity [79]. Diabetes is associated with a range of complications primarily due to chronic hyperglycemia, which leads to vascular damage. The resulting complications are categorized into "microvascular disease," stemming

from damage to small blood vessels, and "macrovascular disease," resulting from damage to larger arteries [80]. Microvascular complications include retinopathy (eye disease), nephropathy (kidney disease), and neuropathy (nerve damage). Major macrovascular complications encompass accelerated cardiovascular disease, leading to myocardial infarction and cerebrovascular events, such as strokes. Cardiovascular disorders in diabetes are characterized by premature atherosclerosis, which manifests as heart attacks and strokes, alongside impaired cardiac function, particularly diastolic dysfunction[81], [82].

Diabetic nephropathy is characterised by the onset of proteinuria and a subsequent decline in the glomerular filtration rate, which can progress over several decades. If left untreated, this condition can lead to uremia, which is often fatal. Importantly, kidney disease is also a significant risk factor for developing macrovascular complications, including heart attacks and strokes [83].

Diabetic neuropathy encompasses both the somatic and autonomic divisions of the peripheral nervous system. Advanced neuropathy, resulting from nerve fiber degeneration in diabetes, is characterised by altered sensitivity to vibrations and thermal thresholds, eventually progressing to loss of sensory perception[84]. The size of neurons plays a crucial role; longer nerve fibers in diabetic patients exhibit an earlier loss of conduction velocity along with the degeneration of their terminals. Consequently, tingling, loss of sensation, and diminished reflexes are often first observed in the feet before ascending to affect other regions, particularly the hands. This distribution is commonly referred to as a "glove and stocking" pattern[85].

Diabetic retinopathy presents a spectrum of lesions within the retina and is the leading cause of blindness among adults aged 20 to 74 years. It is characterised by changes in vascular permeability, capillary microaneurysms, capillary degeneration, and excessive neovascularization. Additionally, the neural retina can become dysfunctional, resulting in the death of certain cell types, which disrupts retinal electrophysiology and impairs colour discrimination.

Another complication associated with diabetes is diabetic cataract, which refers to the progressive opacification of the lens[70]. The ocular lens is an avascular, transparent structure that serves to transmit light to the retina without distortion. All cells forming the lens derive from the proliferation and differentiation of lens epithelial cells, located in the anterior segment beneath the anterior capsule [86]. These epithelial cells play a vital role in lens growth and

maintenance, differentiating into elongated, anucleate lens fibers to preserve lens transparency[86]. Alterations in the metabolism or structure of these lens fibers, induced by glycemic, osmotic, and oxidative stress typical of diabetic conditions, contribute to cataract development [87]. Three molecular mechanisms appear to be involved in the formation of diabetic cataracts: non-enzymatic glycation of lens proteins, oxidative stress, and the activated polyol pathway[70]. In diabetic patients, elevated blood glucose levels increase lens protein exposure to sugars, facilitating glycation. Consequently, protein solubility may be compromised, leading to aggregation and the formation of opacities within the lens. The accumulation of ROS also causes oxidative damage to lens proteins and cellular membrane lipids, resulting in insoluble aggregates and a loss of transparency. Furthermore, the activation of the polyol pathway leads to the accumulation of sorbitol within lens cells, raising osmotic pressure and drawing in water [88]. This causes swelling of the lens fibers and mechanical stress, further compromising lens transparency[70].

1.3 Anthracyclines

Oxidative stress can also be triggered by reactive xenobiotics, derived from external environmental sources or administered to the body for therapeutic purposes.

Anthracyclines are natural compounds isolated from soil bacteria and are extensively used as chemotherapeutic agents in the treatment of leukemia, lymphomas, sarcomas, and a wide range of solid tumours, including breast, gastric, uterine, ovarian, bladder, and lung cancers[89] [90]. Structurally, anthracyclines are characterised by a polyhydroxy anthraquinone core fused to a fourth saturated and differently substituted ring, which forms the aglycone portion, decorated with one or more sugar moieties (**Figure 8**) [91].

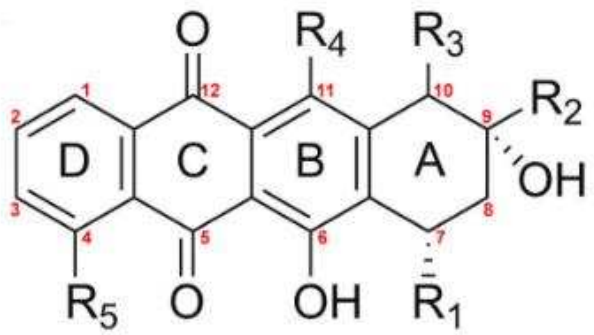

Figure 8. **General structure of anthracycline**.

Daunorubicin (DNB) was the first anthracycline to be isolated from *Streptomyces peucetius* by Arcamone and Di Marco in 1964. This was followed a few years later by the discovery of doxorubicin (DOX), both of which were approved for clinical use shortly after. Since then, several analogues have been identified and tested for therapeutic application; however, only a few, such as epirubicin, idarubicin, and valrubicin, have been introduced into clinical practice (**Table 2**) [91].

Despite their discovery dating back several decades and their known limitations, including side effects and the development of cancer cell resistance, anthracyclines remain a cornerstone of oncology. They continue to rank among the most widely used antineoplastic agents in clinical practice, particularly in combination therapy protocols [89].

ID	COMPOUND	STRUCTURE	CLINICAL CONDITIONS	REFERENCE
A	Daunorubicin	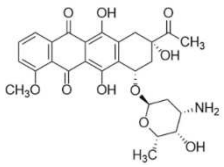	Leukaemias, lymphomas, lymphoproliferative disorders	[92]
B	Doxorubicin	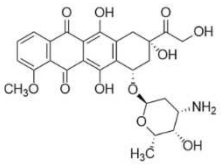	Lymphomas, sarcoma, breast, genitourinary, ovarian, gastrointestinal, liver and hematologic cancers	[93]
C	Epirubicin	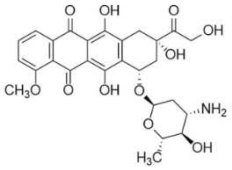	Breast, gastrointestinal, genitourinary, lymphomas and sarcomas	[94]
D	Idarubicin	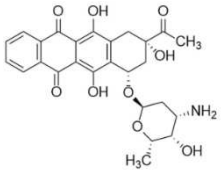	Leukaemias and lymphomas, gastrointestinal and liver cancer	[95]
E	Valrubicin	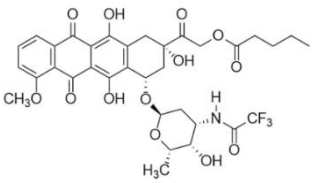	Bladder, urogenital cancers	[96]

Table 2. **Main anthracyclines approved for clinical use as anti-cancer drugs**. Structure and major diseases in which they find application are reported.

1.3.1 Mechanisms of action

Anthracyclines exert their cytotoxic effects primarily in the nucleus, but also at the cytoplasmic and mitochondrial levels (**Figure 9**). These compounds permeate the cell membrane mainly via passive diffusion and enter the nucleus through nuclear pores. Once inside, anthracyclines intercalate into DNA and form adducts with it [97]. Due to their planar structure, anthracyclines insert their aglycone moiety between two adjacent DNA bases, while the sugar moiety is positioned in the minor groove of the DNA double helix. Once intercalated, anthracyclines can form covalent bonds with the DNA, resulting in DNA-anthracycline adducts [98].

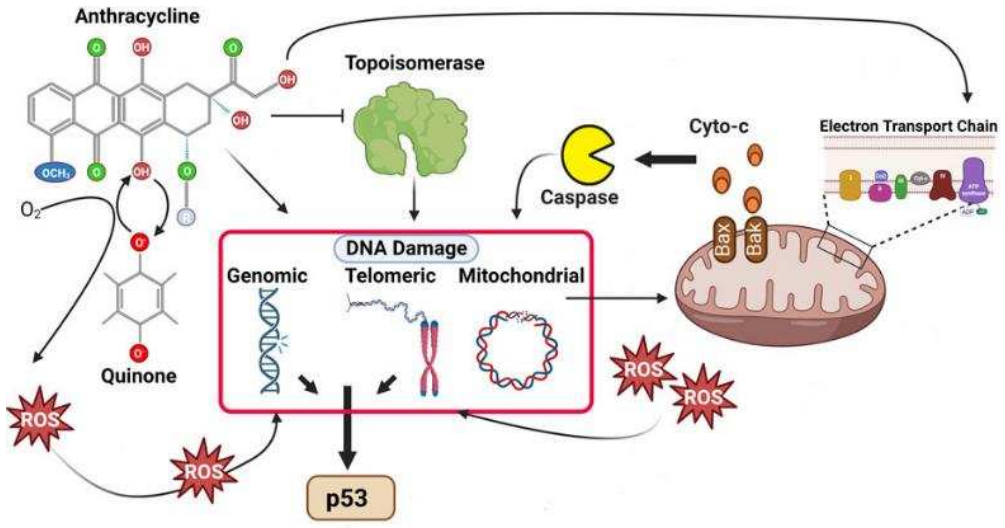

***Figure 9.* Anthracycline multiple contribution to cell toxicity.** *Figure* modified from Booth *et al,* 2022 [134].

The formation of these adducts and intercalation induces torsional stress, disrupts nucleosome structure, leads to histone eviction, and hampers replication and transcription machinery. This results in errors during DNA replication and transcription, alterations to the epigenetic code, and a diminished capacity for double-strand break repair. Intercalation is crucial for the primary cytotoxic mechanism of anthracyclines, which is the inhibition of the enzyme Topoisomerase II (Top2) [99]. Topoisomerases are essential nuclear enzymes that regulate DNA supercoiling and resolve topological stress during replication, transcription, and recombination, making them especially active in rapidly dividing cells, such as cancer cells [100]. Top2 operates by binding to DNA, introducing a transient double-strand

break, passing an intact DNA strand through the gap to relieve torsional stress, and then resealing the break. Anthracyclines inhibit Top2 by trapping the enzyme in a stable ternary complex (Top2-Anthracycline-DNA), preventing the repair of the double-strand break, ultimately leading to widespread genomic instability[90].

Anthracyclines can also exert their cytotoxic effects through the induction of oxidative stress, primarily via the generation of ROS. This occurs through the one-electron reduction of a chelated ferric ion to ferrous ion or the reduction of the quinone moiety to semiquinone. The oxidized species are then regenerated by reacting with molecular oxygen, resulting in the formation of superoxide anion and other ROS (**Figure 10**). This cascade causes damage to biological macromolecules, ultimately leading to cell death, as outlined in **Section 1.1.**

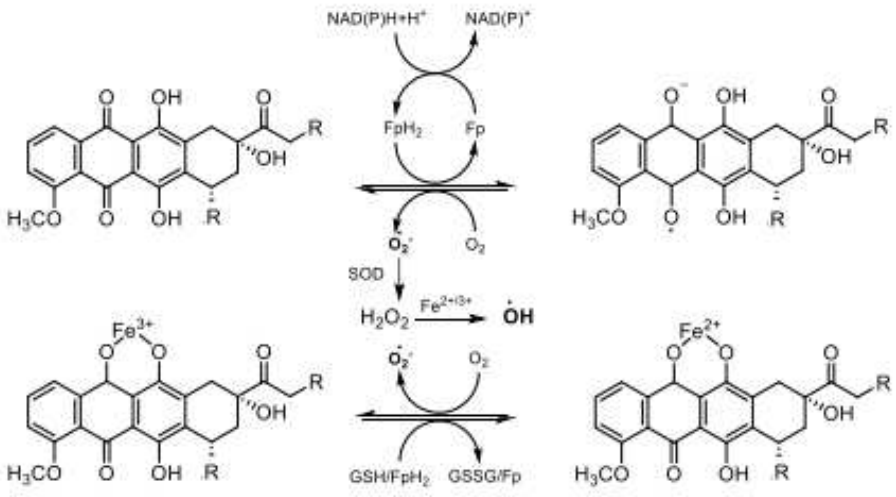

***Figure 10*. Two main pathways of anthracycline-induced ROS production in the cytoplasm**. Figure modified from Martins-Teixeira *et al*., 2020 [90].

Moreover, anthracyclines induce ROS production within mitochondria by disrupting the electron transport chain. Mechanistically, these compounds undergo one-electron reduction by mitochondrial complex I using NADH or by the cytochrome P450 system with reducing equivalents from NADPH, forming a semiquinone radical. This radical rapidly re-oxidizes in the presence of molecular oxygen, generating superoxide anions and regenerating the parent anthracycline (**Figure 11**) [101].

Overall, anthracyclines act by inducing widespread oxidative stress, a key factor contributing to their side effects, particularly cardiotoxicity, which is discussed in the following sections.

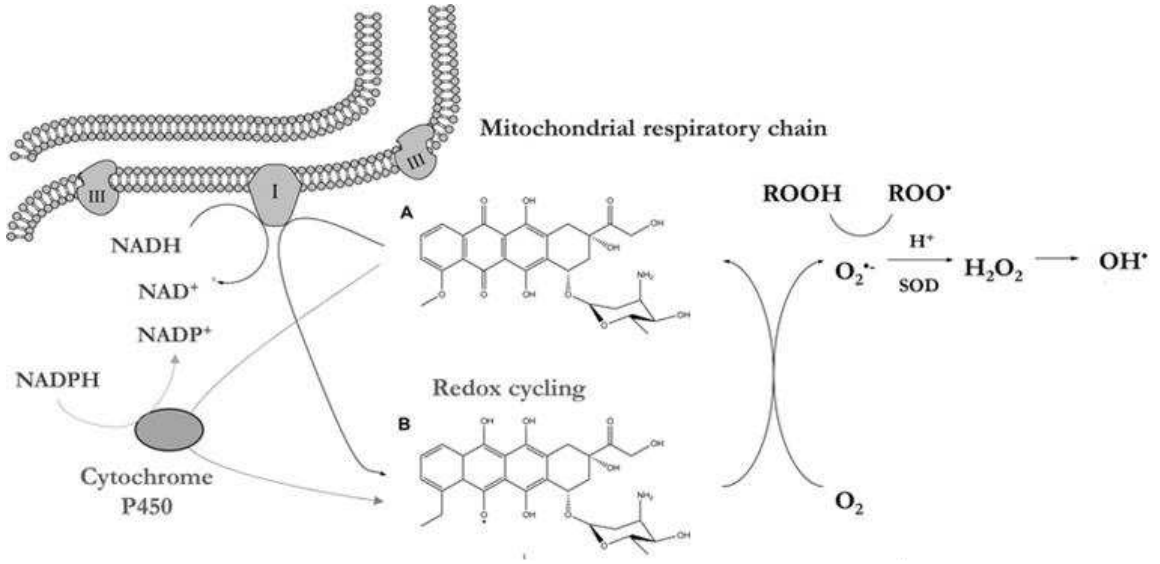

***Figure 11*. Schematic drawing of anthracycline reduction by the mitochondrial electron transport chain.** Figure modified from Wallace *et al*., 2020 [101].

1.3.2 Resistance to anthracyclines

Drug resistance refers to the failure of cells to respond to a therapeutic compound, rendering the treatment ineffective [102]. Cancer cells may develop this resistance after chemotherapy treatment or may possess intrinsic resistance to anthracyclines, which pre-exist prior to drug exposure.

Chemoresistance can emerge following drug exposure due to molecular adaptations that affect the drug's primary targets. For example, mutations and/or abnormal expression of the Topoisomerase II (Top2) enzyme have been identified as key mechanisms driving cancer cell resistance to anthracyclines [103], [104].

The primary mechanism of multidrug resistance (MDR), which also affects anthracyclines, involves altered membrane transport, specifically the active expulsion of drugs from cells. This is mediated by the overexpression of ATP-binding cassette (ABC) transporters [105]. These transporters consist of two transmembrane domains that recognize and translocate substrates

across the cell membrane, and two nucleotide-binding domains responsible for ATP hydrolysis, which powers the transport process.

Anthracycline efflux is primarily facilitated by three key transporters: multidrug resistance protein 1 (MDR1, which corresponds to the ABCB1 protein and is also known as P-glycoprotein), breast cancer resistance protein (BCRP, the ABCG2 transporter), and multidrug resistance protein 1 (MRP1, the ABCC1 pump) [106].

MDR1 is a 170-kDa glycoprotein that functions as an efflux pump for a broad spectrum of anticancer drugs, induced by environmental stress, natural products, heat shock, and other nonspecific stressors[107]. A significant increase in *mdr1* expression has been demonstrated upon exposure to daunorubicin (DNB), epirubicin (EPI), and doxorubicin (DOX) both in vitro and in vivo [108], [109]. Notably, recent findings have shown that the increased expression of MDR1 in chemoresistant cells correlates with enhanced translocation of these transporters to the nuclear membrane, where they facilitate the extrusion of DNB from the nucleus to the cytoplasm, thereby preventing its toxic action, while in the sensitive cell line, it efficiently accumulated in the nucleus[110], [111], [112].

The ABCG2 transporter, identified in 1998 in an MDR breast cancer subline, was named breast cancer resistance protein (BCRP) [113]. Overexpression of BCRP is associated with resistance to a wide range of anticancer agents, including anthracyclines [114]. Recently, Yin *et al*. showed that inhibition of MDR1 and BCRP in liver cancer cell lines using either pharmacological inhibitors or RNA interference increased intracellular DOX concentration and enhanced apoptosis [115].

Another critical player in anthracycline efflux is MRP1, first identified in a DOX-resistant small cell lung cancer line, H69AR [116]. Structurally, MRP1 resembles MDR1, sharing broad substrate specificity. However, MRP1 can also co-transport more hydrophobic or cationic drugs with glutathione (GSH), as well as glucuronide-, sulfate-, or GSH-conjugated products of Phase II drug metabolism [117] [118].

Since one of the cytotoxic mechanisms of anthracyclines is ROS generation and oxidative stress induction, cancer cells can develop resistance by reinforcing their antioxidant defences. Various scavenger molecules (*e.g.*, GSH, N-acetyl cysteine (NAC), GSR, SOD and CAT) are

known to mitigate the cytotoxic effects of anthracyclines and are highly expressed in resistant cells [119].

Anthracyclines can also be subjected to the action of detoxifying enzymes, resulting in the formation of metabolites that either enhance or diminish their anticancer properties. In the context of drug resistance, several cytoplasmic NADPH-dependent carbonyl and aldo-keto reductase enzymes play a crucial role in anthracycline detoxification. Specifically, CBR1, CBR3, and many enzymes from the AKR1 family (AKR1A1, AKR1B10, AKR1C1, AKR1C2, AKR1C3) have been implicated in this process [120][121]. Among these, CBR1 is the primary enzyme responsible for DNB metabolism. Although AKR1B1 also exhibits DNB-reductase activity, it is significantly lower than that of the other enzymes, with a catalytic efficiency (K_{cat}/K_m) approximately 70 times lower than CBR1 [120]. Regarding DOX metabolism, AKR1C3 is the leading enzyme [122], [123].

These enzymes catalyse the two-electron reduction of anthracyclines at the C-13 carbonyl group, leading to the formation of secondary alcohol metabolites (**Figure 12**). While other metabolites are produced in small quantities, these alcohol derivatives are the most abundant [124].

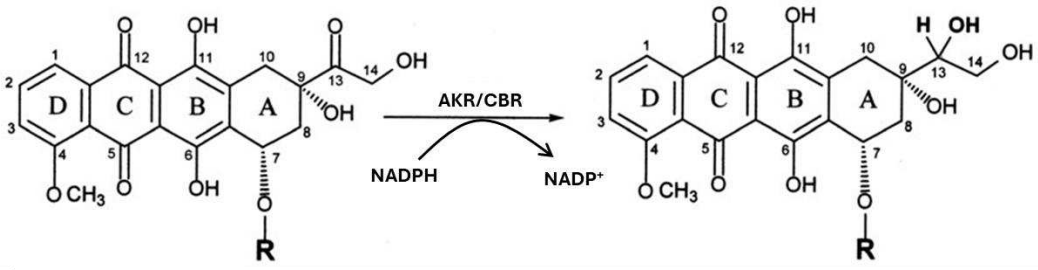

Figure 12. **Two-electron reduction of anthracyclines.**

The secondary metabolites generated by these enzymes are less cytotoxic than their parent compounds. For example, the half-lethal concentration (LC_{50}) values of DOXol are 59–162 times higher than those of DOX[125]. The C-13 secondary alcohol moiety of DOXol is redox-inactive toward oxygen and thus cannot initiate a free radical cascade [126]. Additionally, DOXol is more suitable for ABC-mediated efflux than DOX, implying that its reduced anticancer activity may be related to its higher affinity for ABC transporters, leading to lower intracellular concentrations of the drug[127]. Additionally, DOXol exhibits significantly lower DNA binding

affinity compared to DOX [128]. Moreover, while DOXol is retained in the cytoplasm or lysosomes, DOX predominantly accumulates in the nucleus [129]. In addition to their decreased antineoplastic activity, reduced anthracycline metabolites are linked to cardiotoxicity, as will be discussed in subsequent sections.

Chemoresistance can also be an intrinsic feature of cancer cells, with all the mechanisms mentioned above already hyperactivated prior to the first drug exposure. Due to the high genomic instability characteristic of cancer cells, tumours often consist of heterogeneous cell populations. Minor genetic differences can sometimes ensure the survival of certain cells in the presence of a drug. Cells with advantageous traits that allow them to survive treatment will be selected, clonally expand, and eventually give rise to an entire drug-resistant tumour mass.

Furthermore, the cancer stem cell model is increasingly recognized as a key mechanism of chemoresistance (**Figure 13**). According to this model, tumours contain a subpopulation of cancer stem cells, which share several characteristics with classical stem cells. These include relative quiescence (which may shift toward proliferation in response to stimuli), drug resistance via the expression of various ABC transporters, enhanced DNA repair capacity, and resistance to apoptosis [130]. As a result, a portion of these cancer stem cells can survive chemotherapy and contribute to tumour regrowth. Additionally, recurrences often exhibit multidrug resistance (MDR), particularly to drugs targeting the cell cycle. In the case of anthracyclines, slowly proliferating cancer stem cells may evade treatment by limiting cell proliferation and, thus, Top2 activity and DNA accessibility.

In this view, the epithelial-to-mesenchymal transition has gained considerable attention as a potential mechanism of chemotherapeutic resistance in recent years, due to its ability to convert tumour cells into tumour stem cells and confer resistance to chemotherapy [131]. This aspect will be further discussed in **Subsection 1.3.4.**

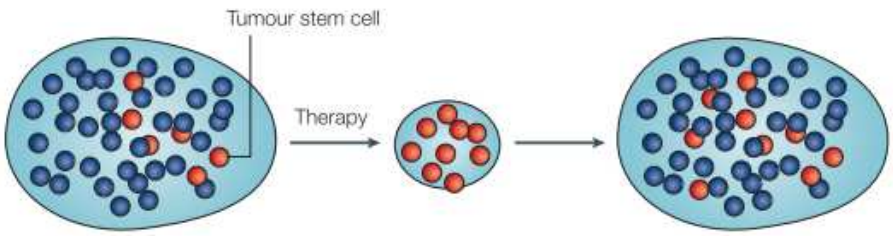

Figure 13. **Cancer stem cells model of tumour chemoresistance.** Figure modified from Dean *et al.*, 2005 [250]

1.3.3 Anthracyclines- associated complications

The use of anthracyclines is associated with a wide range of side effects, varying from acute and generally reversible chemotherapy-related symptoms, such as nausea, vomiting, diarrhea, stomatitis, mucositis, alopecia, gastrointestinal disturbances, rash, and bone marrow suppression, to more severe long-term effects, including cardiotoxicity, gonadotoxicity, and the development of recurrences and metastasis[91]. These long-term effects significantly reduce patients' quality of life and pose substantial limitations on the use of anthracyclines.

Cardiotoxicity is the most significant and well-studied side effect of anthracycline treatment. The therapeutic use of anthracyclines is restricted due to their severe, multifactorial, dose-dependent, and irreversible cardiotoxicity, which can lead to cardiac contractile dysfunction, cardiomyopathy, arrhythmias, and heart failure [132], [133]. As discussed earlier, the two-electron reduction of anthracyclines by NADPH oxidoreductases results in the formation of secondary alcohol metabolites, which are considered key contributors to long-term anthracycline-induced cardiotoxicity[123], [126], [134], [135]. This metabolic conversion occurs predominantly in the heart, where these alcohol metabolites accumulate and are not cleared as efficiently as the parent compound.

The exact mechanisms underlying anthracycline-induced cardiotoxicity are not yet fully understood. However, it is evident that there is a direct correlation between the accumulation of C-13 alcohol metabolites in the heart and progressive impairment of both contractility and relaxation of the myocardium. These effects are largely due to altered myocardial energy metabolism, disrupted ionic gradients, and impaired Ca^{2+} storage, all of which are essential for proper cardiac function[132].

Anthracycline-induced toxicity also affects the gonads, which are among the tissues with a high rate of cell proliferation. Although in many cases gonadal damage may be reversible, with gonadal function often restored within months after treatment, anthracycline-induced gonadotoxicity can result in significant issues such as a shortened reproductive lifespan, complications during pregnancy, and, in some cases, irreversible loss of reproductive function. Additionally, gonadotoxicity is associated with an increased risk of osteoporosis, infertility, and cardiovascular disease. This side effect is primarily attributable to the double-strand DNA

breaks induced by anthracyclines, leading to damage and cell death in both germ cells and somatic cells, including vascular cells and those in the stromal compartments of the gonads [136].

1.3.4 The epithelial to mesenchymal transition

Epithelial-to-Mesenchymal Transition (EMT) programs enhance resistance to cell death through various mechanisms. EMT occurs physiologically during embryonic development, tissue regeneration, and wound healing, and pathologically in conditions such as organ fibrosis and metastasis. EMT-induced multidrug resistance is mediated by several mechanisms, including a slower proliferation rate, elevated expression of anti-apoptotic proteins, and the upregulation of ABC transporters, which facilitate drug efflux [137].

The activation of EMT was first observed in cell cultures after exposure to the Transforming Growth Factor β (TGF-β), which remains the primary inducer of the process[138]. EMT involves complete reprogramming of gene expression that converts epithelial cells into cells with mesenchymal properties, driven by master regulators such as SNAIL, TWIST, and the Zinc-finger E-box-Binding (ZEB) transcription factors, in response to external stimuli[139]. A general scheme of EMT is depicted in **Figure 14**. Epithelial cells typically exhibit apical-basal polarity, where the apical and basolateral surfaces have distinct appearances and functions [140]. These cells are closely associated with one another through specialized cell-cell junctions, such as tight junctions, adherens junctions, and desmosomes. Tight junctions, located near the apical surface, serve as membrane fusions that provide intercellular sealing and help maintain the functional separation between the apical and basolateral surfaces. Occludin and claudins are key components of these structures [140]. Adherens junctions, located adjacent to tight junctions on the basolateral side, link epithelial cells to the cytoskeleton. The transmembrane adhesion protein E-cadherin, which characterises adherens junctions, engages in homotypic interactions via its ectodomain. The cytoplasmic domain of E-cadherin binds to β-catenin, which interacts with α-catenin, anchoring the complex to the actin cytoskeleton [140].

One of the initial events in EMT is the disassembly of tight and adherens junctions, leading to the loss of cell polarity and the initiation of cytoskeletal reorganization[138]. Notably, the loss of E-cadherin is considered a hallmark of EMT, accompanied by the upregulation of N-cadherin, a protein commonly found in non-epithelial tissues, particularly endothelial cells. The acquisition of N-cadherin is critical for enabling mesenchymal cells to interact with non-epithelial tissues, especially with blood vessel cells, thereby facilitating their entry into the bloodstream and subsequent dissemination [141]. Simultaneously, cells undergoing EMT acquire a mesenchymal identity, characterised by the expression of mesenchymal cytoskeletal proteins such as vimentin, and the increased deposition of extracellular matrix (ECM) components, including collagen and fibronectin [141]. These ECM components stimulate integrin signalling and promote the formation of focal adhesion complexes, which are essential for cell migration. Additionally, EMT is associated with the upregulation of several matrix metalloproteases, such as members of the matrix metalloproteinase (MMP) family, the A Disintegrin and Metalloproteinase (ADAM) family, and the A Disintegrin and Metalloproteinase with Thrombospondin Motifs (ADAMTS) family [142], [143], [144]. A comprehensive study of the ADAMTS9 protein, along with a detailed analysis of the ECM proteoglycan syndecan-4, will be provided in **Appendices I** and **II**, respectively. These findings represent the results of research conducted during a period of study abroad at the University of Surrey (Guildford, UK).

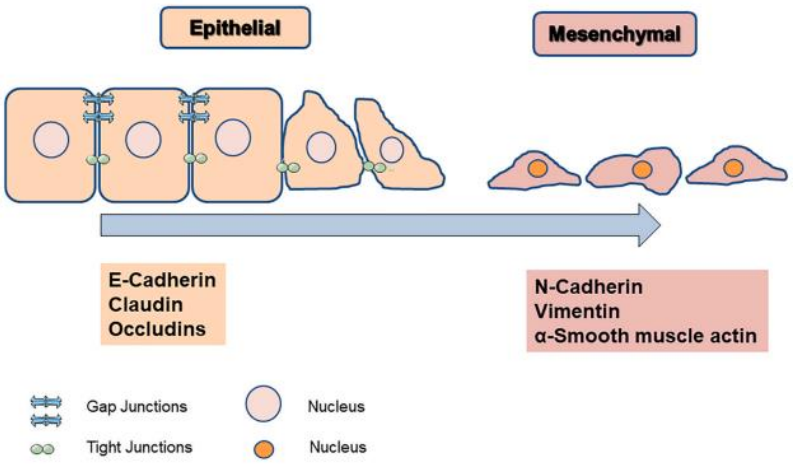

Figure 14. The epithelial to mesenchymal transition. Figure from Jayachandran *et al*., 2021[251].

More recently, AKR1B1 has assumed a significant role in promoting EMT in both tumour and non-tumour contexts [145], [146], [147]. Recent findings demonstrate AKR1B1 is upregulated in numerous tumours and positively correlated with metastatic outcome in pancreatic, breast, gastric[148], [149], [150], [151]

AKR1B1 expression was shown to be a direct transcriptional target of EMT master gene regulator Twist2 and correlated with several other EMT markers [152], although the exact mechanism of action of this enzyme remains unclear. Two main molecular pathways have been proposed to explain its involvement in EMT. According to the first mechanism, Twist2 transcriptionally induces AKR1B1 expression, producing GS-DHN which activates NF-κB (as described in **Subsection 1.2.2**). In turn, NF-κB up-regulates Twist2 expression, thereby fulfilling a positive feedback loop that activates the reprograming[153]. The second mechanism suggests that AKR1B1 plays a noncatalytic role in the TGF-β/SMAD2 pathway. Once bound to the cofactor NADPH, AKR1B1 exposes binding sites for the Small Mother Against Decapentaplegic 2 (SMAD2) protein and the formation of a binary AKR1B1-SMAD2 complex promotes SMAD2 phosphorylation by the activated TGF-β receptor [154]. Consistently, mesenchymal-like cancer cells showed increased AKR1B1 levels, and AKR1B1 knockdown or pharmacological inhibition were sufficient to revert EMT [155]. Overall, these literature findings raise the intriguing question of whether AKR1B1 may represent a link between glucose metabolism, reactive aldehyde detoxification and the onset of the EMT process.

1.4 Aim of the thesis

Oxidative stress is a key factor in the development of numerous diseases and their associated complications, such as diabetes and cancer. Given the variety of pro-oxidant stimuli and the complexity of cellular responses to these stimuli, two important sources of oxidative stress were considered in this thesis: high intracellular glucose levels and daunorubicin, an anthracycline chemotherapeutic. A common feature of these two apparently different molecules is their susceptibility to AKR enzyme action.

The first objective was to investigate the response of human lens epithelial cells (HLEC), used as an *in vitro* model of diabetic cataract, to stimulation with high glucose concentrations. Specifically, this research aimed to clarify the cellular response to 75 mM glucose, focusing on the activation of the polyol pathway and inflammation, while also determining the involvement of the enzyme AKR1B1 in the NF-κB pathway.

The second objective aimed to elucidate the role of oxidoreductase enzymes, particularly AKR1A1, AKR1B10, AKR1C3, and CBR1, in the metabolism of daunorubicin, and to enhance the efficacy of this chemotherapeutic agent through their pharmacological inhibition. For this part of the study, the A549 cell line was employed as a model of non-small cell lung cancer (NSCLC). During this investigation, the generation of a new cell line resistant to daunorubicin and displaying mesenchymal properties led to the additional objective of characterising these cells to understand the mechanisms underlying chemoresistance, drug detoxification, and the promotion of the epithelial-to-mesenchymal transition.

CHAPTER 2: MATERIALS AND METHODS

2.1 Cell Culture Maintenance and Treatments

2.1.1 HLEC_F cell line

The human lens epithelial cell line B3 (ATCC CRL-11421) was obtained from ATCC (Rockville, MD, USA) and stably transfected with the pGL4.32[luc2P/ NF-κB -RE/Hygro] plasmid (Promega, E8491), designed as HLEC_F. This plasmid, illustrated in **Figure 15**, contains a hygromycin resistance gene and five copies of the NF-κB response element (NF-κB-RE). Upon NF-κB binding, this response element drives the transcription of the *luc2P* reporter gene, which encodes the luciferase enzyme from *Photinus pyralis*. This system was selected for its ability to provide a direct, quantitative, and functional measure of NF-κB transcriptional activity in living cells. While reporter plasmids are widely used in the field, their introduction into cells can potentially influence physiological responses. To address these concerns, the host laboratory previously conducted the appropriate control experiments, involving cells transfected with an empty plasmid (namely lacking functional reporter gene) designed as HLEC_NO.

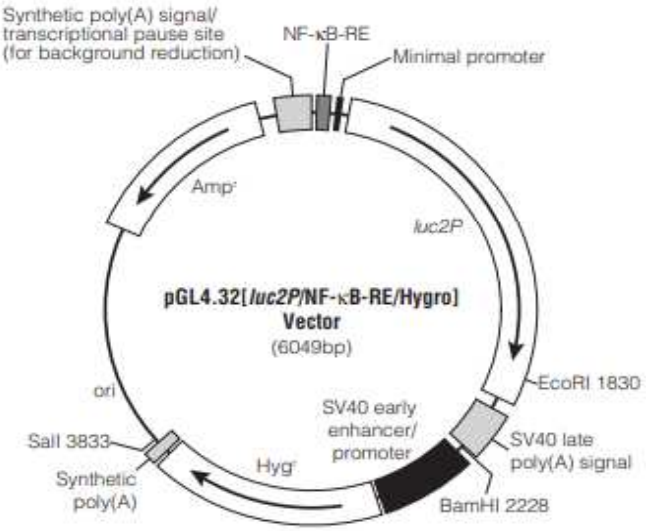

***Figure 15.* pGL4.32[luc2P/ NF-κB -RE/Hygro] plasmid map**. The plasmid contains the *luc2P* transgene which encodes the luciferase enzyme from *Photinus pyralis*, under the control of 5 copies of NF-κB responsive element (RE). It also includes the hygromycin resistance gene (Hyg^r) for selection in mammalian cell.

Prior to initiating experimentation on HLEC_F, proliferative and enzymatic characterisation were performed on HLEC_F, HLEC_NO and wild type HLEC lines, confirming all of them retained nearly unchanged properties (data not shown in this thesis).

HLEC_F cells were routinely cultured at 37 °C in a humidified atmosphere with 5% CO_2, using Eagle's modified minimum essential medium (MEM) supplemented with 5.5 mM D-glucose, 20% (v/v) fetal bovine serum (FBS), 50 mU/mL penicillin/streptomycin, 2 mM glutamine, and 100 µg/mL hygromycin (complete medium). Cells were grown in the indicated medium until they reached 70% confluence, then washed with PBS and sub-cultured using a Trypsin/EDTA solution. 72 h before the treatments described below, cells at passages 15–20 (30–40 residual doublings) were plated at a density of 20,000 cells/cm^2 in growth medium. Prior to the cell treatments, cells were growth-arrested for 24 h by incubation in MEM containing 0.5% FBS, 50 µg/mL gentamicin, 2 mM glutamine, and 100 µg/mL hygromycin.

For emulating the hyperglycemic stimulus, increasing concentrations (20-100 mM) D-Glucose in PBS solution was added to HLEC_F cells and incubated for 24, 48 or 72 h, as indicated. An equal volume of PBS was added to the control cells, with the same time of incubation. To investigate the effects of specific AKR1B1 inhibition on the cellular response to hyperglycemia, particularly regarding the activation of inflammatory and polyol pathways activation, as well as cell viability, Sorbinil was administered to HLEC_F cells. The day before treatments with high glucose levels, HLEC_F cells were incubated with Sorbinil at the indicated concentration. Unless otherwise specified, Sorbinil was dissolved in dimethyl sulfoxide (DMSO) and administered to the cells following a 2,000-fold dilution in growth medium, ensuring cells were always exposed to the same, inert, percentage of DMSO, namely 0.05% (v/v). As a positive control of activation of inflammatory response, HLEC_F cells were treated with 0.2 nM of the pro-inflammatory cytokine Tumor Necrosis Factor-alpha (TNF-α) dissolved in a solution of human serum albumin (HSA) or, as control, 0.35 µg/ml HSA alone, for the indicated time of incubation.

2.2.2 A549 cell line

The human alveolar basal adenocarcinoma A549 cell line (ATCC- CCL-185) was obtained from ATCC (Rockville, MD, USA). Cells were routinely maintained in low glucose Dulbecco's modified Eagle's medium (DMEM), supplemented with 10% FBS (v/v), 50 mU/mL penicillin/streptomycin and 2 mM glutamine, at 37° C in a humidified atmosphere, in the presence of 5% CO_2. Cells were cultured in the indicated medium until they reached 80% confluence, then washed with PBS and sub-cultured using Trypsin/EDTA solution. 24 h before the treatments, described below, cells at passages 10–20, were plated at a density of 15,000 cells/cm^2 in growth medium. Simultaneously with the treatments, the concentration of FBS in the growth medium was reduced to 0.5% to prevent interferences between the administered chemicals and FBS components.

To test the cell sensitivity to DNB, A549 cells were incubated with increasing concentrations of DNB, prepared as reported in **Subsection 2.9.3** and diluted in sterile water, for 24 or 48 h. To evaluate the effectiveness of synthetic inhibitors of oxidoreductase enzymes in increasing the DNB toxicity, cells underwent preincubation of 4 h with inhibitors, before 24 h DNB treatment.

2.2.3 A549^{DNB} cell line

The daunorubicin-resistant cell line (designated as A549^{DNB}), established from the A549 cell line, was cultured in low-glucose DMEM containing 10% FBS, 50 mU/mL penicillin/streptomycin, 2 mM glutamine, and 50 nM daunorubicin (DNB) dissolved in <0.001% DMSO for at least 4 weeks. The medium was refreshed every other day until the cells reached 90% confluence. At that point, the cells were washed with PBS, detached using a Trypsin/EDTA solution, and seeded at a specific density of 10,000 cells/cm^2. Simultaneously, the corresponding control cells (A549^{CONT}) were cultured under the same conditions, but in the presence of an equivalent percentage of DMSO (without DNB). Cell growth was routinely monitored microscopically, and representative images were weekly captured using the JuLI Br Live Cell Movie Analyzer (NanoEnTek USA Inc., Waltham, MA, USA). After one month, cells were plated at a density of 15,000 cells/cm^2 and used for experiments.

2.2 *In vitro* Cell Assay

2.2.1 MTT Assay

Cell viability of HLEC_F, A549 and A549^{DNB} was evaluated using the 3-(4,5-dimethylthiazol-2-yl)-2,5-diphenyltetrazolium bromide (MTT) assay, according to the general procedure [156]. Briefly, at the designed time points, cells were incubated with a final concentration of 0.5 mg/ml MTT dye (Sigma-Aldrich, cat. M2003) dissolved in sterile PBS, for 30 min at 37°C. During this incubation, cells reduced the tetrazolium salts to the chromogenic, formazan crystals, proportionally to their dehydrogenase activity. The resulting formazan was solubilized in an equal volume of a 2-propanol/ 0.04 N HCl solution, optic density (OD) was determined at 563 nm using the EL808 Ultra Microplate Reader (Bio-Tek Instrument INC) to quantify cell viability, which was expressed as % with respect to the untreated control. Blank value, resulting from the incubation of MTT solution in a medium in the absence of cells, was subtracted to each experimental value.

2.2.2 Sulforhodamine B Assay

Cell proliferation was monitored using the sulforhodamine B (SRB) assay, based on the capacity of SRB to tightly bind proteins [157]. Briefly, at the designed time point, cells were fixed with 10% (w/v) trichloroacetic acid (TCA) incubated for 30 min at 4°C. Plate was then rinsed twice with water and let dry at room temperature (RT). Finally, fixed cells were incubated with 0.057% (w/v) SRB solution (Sigma-Aldrich, cat. 283924) for 30 min at RT, washed repeatedly with 1% (v/v) acetic acid for removing excess dye, and the protein-bound dye dissolved in 10 mM Tris Base buffer. OD was determined at 510 nm using a microplate reader and the proliferation rate was calculated with respect to the first measured time point (24h). Blank was measured reading the OD at 510 nm of the Tris Base buffer alone and subtracted to each experimental value.

2.2.3 Wound Healing Assay

$A549^{DNB}$ and $A549^{CONT}$ were seeded in well of a 6-Multiwell plate in 2.5 mL completed medium in the presence of 50 nM DNB or DMSO, respectively. Once at confluence, cell monolayer was scraped in a straight line with a sterile 10 µl pipette tip. Thus, culture medium was discarded, cells were gently washed with PBS to remove debris, and fresh medium was added. Cells were allowed to migrate for 48 h. Images were captured immediately after the wound formation (t0) and at different time point (8, 24, 48 hours) using the JuLI Br Live Cell Movie Analyser (NanoEnTek USA Inc., Waltham, MA, USA). The wound closure was measured using the Wound Healing Size Tool Plugin of ImageJ software, and the percentage of area recovery was calculated with respect to t0, using the equation:

$$\% \, Area \, Recovery \, = \left(\frac{A_{t0} - A_{tx}}{A_{t0}}\right) \times 100 \, ,$$

where A_{t0} is the wound area at t0, and A_{tx} is the wound area at a specific subsequent time point.

2.*3* Immunofluorescence

$A549^{DNB}$ and $A549^{CONT}$ cell were seeded in an 8-well Chamber slide removable (Ibidi). The day after, cells were fixed incubating with 4% (w/v) paraformaldehyde in PBS for 10 min, permeabilized with 0.1% Triton X-100 in PBS for 5 min, and blocked in 5% BSA (w/v) in PBS with Tween20 0.1% (PBS-T) for 30 min. Thereafter, cells are incubated overnight (ON) at 4°C with mouse anti-vimentin antibody (Santa Crutz Biotechnology, cat. sc-6260) diluted 1:1000 in 2% BSA/PBS-T, then stained with anti-mouse Alexa Fluor 594 antibody (Invitrogen, cat. A32742) used 1:1000 in 2% BSA/PBS-T. Chambers were finally removed, glass slide mounted with Fluoreshield Mounting Medium with DAPI (Abcam, cat. ab104139) and stored in the dark at 4°C. Images were acquired with Nikon Confocal Ax, using Plan Fluor 40 X Oil objective (Lens NA = 1.3; laser: 405, 488, 561 and 640 nm).

2.4 Recombinant Enzymes Expression and Purification

2.4.1 Transformation and Expression of Human Recombinant Enzymes

The coding sequences of the human enzymes AKR1A1, AKR1B10, AKR1C3 and Sorbitol Dehydrogenase (SDH), optimized for expression in bacteria, were cloned into pET30 plasmids by Eurofins, under the control of an inducible promoter activated by Isopropyl-β-D-1-thiogalactopyranoside (IPTG). The construct also contained a gene conferring resistance to kanamycin, which was required for the selection of transformed bacteria. The BL21 strain of *E. coli* competent cells (Agilent, cat. 230240), was used for transformation with each plasmid. BL21 cells were incubated with the pET30 vector for 1 h on ice, followed by heat shock treatment for 60 sec at 42°C and immediate transfer back to ice for 5 min. Afterward, 10 volumes of Luria-Bertani (LB) broth (10 g/L tryptone, 5 g/L yeast extract and 10 g/L NaCl) were added to the cells, which were further incubated at 37°C for 1 h in agitation. Transformed cells were grown ON at 37°C in LB broth supplemented with 30 µg/mL kanamycin. When the culture had reached an OD of 0.8 at 600 nm, recombinant enzyme expression was induced by the addiction of 0.4 mM IPTG (final concentration), and the culture was incubated for 3 h at 37°C in agitation. Thus, cells were centrifugated at 3,500 × *g* for 15 min at 4°C. The resulting pellet was resuspended in 20 mM Tris HCl buffer, pH 7.4, containing 2 mM D, L-dithiothreitol (DTT) and 1 mM Phenylmethanesulfonyl fluoride (PMSF, 4 ml buffer per gram of pellet). The resulting suspension underwent three freezing (-20°C for 30 min) and thawing (37°C for 90 sec) cycles and sonicated 5 times for 10 sec with intervals of 20 sec (50% amplitude). Homogenate was finally centrifuged at 10,000 × *g* for 90 min at 4°C and supernatant, containing the expressed protein in soluble form, was referred to as the crude extract.

2.4.2 Purification of Recombinant Enzymes

The crude extract of each recombinant enzyme was subjected to a general purification procedure consisting of two sequential chromatographic steps.

Initially, an aliquot of crude extract, containing approximately 85 mg of protein, was applied to a DEAE Sepharose column (Ø 3,5 cm x h 15 cm), previously equilibrated with 50 mM sodium phosphate buffer, pH 7 containing 2 mM DTT. The sample was eluted with the same buffer at a flow rate of 20 mL/h. Fractions of 3 mL were collected, and the absorbance at 280 nm was monitored. Once the absorbance at 280 nm returned to baseline level, the elution buffer was supplemented with 0.37 M NaCl for further elution. Each fraction was assayed for the enzymatic activity using appropriate enzymatic assay detailed in **Subsection 2.5.1**. Fractions displaying activity were pooled ad concentrated using a YM10 (or YM30 for SDH) Amicon ultrafiltration membrane.

The pool sample from DEAE column (Pool DEAE) was then applied to a Blue Sepharose column (or Affi Blue for SDH) (Ø 1,6 cm x h 6,5 cm,) pre-equilibrated with 50 mM sodium phosphate buffer, pH 7 at a flow rate of 20 mL/h. Fractions of 2 mL were collected and monitored for absorbance at 280 nm. When the absorbance reached baseline levels, recombinant enzyme was eluted with 50 mM sodium phosphate buffer, pH 7 containing 2 mM DTT, 0.37 M NaCl and the 0.1 mM NADPH (or 0.1 mM NAD^+ for SDH). Each fraction was assayed for enzymatic activity using the appropriate enzymatic assay detailed in **Subsection 2.5.1**. Active fractions were collected in a pool (Pool Affinity) and concentrated using a YM10 (or YM30 for SDH) ultrafiltration membrane.

The entire purification procedure was carried out at 4°C. At the end of each purification step, aliquots were taken for protein content determination (see **Subsection 2.9.1**) and purity assessment through electrophoretic separation followed by Comassie Brilliant Blue staining.

Purified enzymes were stored at -80°C in elution buffer with 20% glycerol (v/v), except for AKR1B10 which was stored at -20°C in elution buffer containing 30% glycerol (v/v).

2.5 Enzyme Activity Assay

2.5.1 Recombinant Enzyme Activity Assay

Prior to the enzymatic assays, each purified enzyme was extensively dialyzed at 4°C against 10 mM sodium phosphate buffer pH 7 containing 0.5 mM DTT, using dialysis tubing. Purified recombinant AKR1B1 and CBR1 were already available in my laboratory and obtained as reported by Balestri *et al.*[158] and Rotondo *et al.*[159], respectively. Enzymatic activity was monitored spectrophotometrically by following the variation in absorbance of cofactor at 340 nm per minute, with the molar extinction coefficient of NADH and NADPH at this wavelength being 6.22 mM^{-1} cm^{-1}. Reaction mixtures were prepared in a final volume of 700 µL, with a specific composition for each enzyme reported in **Table 3**. Before initiating the reaction, the variation in absorbance per minute in the absence of the substrate was monitored and recorded as the blank. One Unit of enzyme activity (U) is defined as the amount of enzyme required to convert 1 µmol of substrate/min under the indicated conditions. The Specific Activity (SA) is calculated dividing the Unit of enzyme activity by the mg of protein assessed.

Enzyme	Substrate	Cofactor	Buffer	Other components
AKR1A1	0.720 mM 4-Nitrobenzaldehyde	0.18 mM NADPH	100 mM sodium phosphate, pH 7	-
AKR1B1	10 mM L-Idose	0.18 mM NADPH	250 mM sodium phosphate, pH 6.8	0.38 M ammonium sulfate; 0.47 mM EDTA
AKR1B10	5 mM D, L- glyceraldehyde	0.18 mM NADPH	100 mM sodium phosphate, pH 7	-
AKR1B10	0.04 mM HNE	0.18 mM NADPH	100 mM sodium phosphate, pH 7	-
AKR1C3	0.012 mM 9,10-Phenanthrenequinone	0.18 mM NADPH	50 mM sodium phosphate, pH 6	-
CBR1	0.03 mM GS-nonanal	0.18 mM NADPH	50 mM sodium phosphate, pH 6.2	-
CBR1	0.1 mM GS-HNE	0.18 mM $NADP^+$	50 mM sodium phosphate buffer, pH 8.4	-
SDH	400 mM D-Fructose	0.18 mM NADH	100 mM Tris Base, pH 7.4	-
SDH	100 mM L-Sorbitol	0.18 mM NAD^+	100 mM Tris Base, pH 8	-

***Table 3.* Composition of reaction mixtures used for the spectrophotometric assay for each recombinant enzyme.** The final assay volume is 700 µL, and the reaction is initiated by the addition of the specified substrate.

Inhibition experiments were conducted using the assay specified for each enzyme, with the addition of the indicated concentration of inhibitor dissolved in DMSO. As a control, the same volume of DMSO (without inhibitor) was used, ensuring that DMSO did not exceed 0.5% of the final reaction volume.

2.5.2 Oxidoreductase Activities Assay in cellular extract

Oxidoreductase activity in cellular extract was evaluated in A549, $A549^{DNB}$ and $A549^{CONT}$ cells. Cells were seeded in 100 mm diameter plates. Once confluent, cells were rinsed with PBS with the addiction of 1 mM PMSF, harvested using a cell scraper and transferred in an Eppendorf tube. Cell lysis was performed using three rapid freezing/thawing (F/T) cycles, consisting of freezing at -80°C for 5 min and thawing at 37°C for 1 min. The resulting lysate was then centrifuged at 14,000 × *g* for 30 min at 4°C and supernatant was extensively dialyzed at 4°C against 10 mM sodium phosphate buffer, pH 7 in dialysis tubing. Protein content was determined, and its NADPH/NADH-dependent activities were assessed using different substrates. Specifically, the same assay conditions reported in **Table 3** for recombinant enzymes were applied with 50-100 µg protein per assay. Activities for each substrate were reported as SA.

2.5.3 DNB-reductase Activity Assay of recombinant enzymes

Due to the interference of DNB with measures at 340 nm, the DNB-reductase activity of the purified enzymes could not be evaluated spectrophotometrically. To overcome this limitation, a fluorometric assay was developed to assess DNB-reductase activity, leveraging the fluorescent properties of NADPH, which has an emission peak at 450 nm when excited at 340 nm. Before initiating the reaction, recombinant enzymes were extensively dialyzed as described previously and spectrophotometrically titrated using the standard assay outlined in **Table 3**. The reaction mixtures for the evaluation of DNB-reductase activity were prepared in wells of a 96-well Greiner Black flat bottom fluorescence plate and consisted of 170 µM DNB, 25 µM NADPH, increasing amounts of purified AKR1A1, AKR1B10, AKR1C3, or CBR1 enzymes,

in 50 mM sodium phosphate buffer pH 6, within a final volume of 200 µL. The consumption of NADPH per minute was monitored at 450 nm using a FLUOstar® Omega Plate Reader (BMG Labtech) for up to 20 min, and the slope of the resulting curve was plotted against the respective amount of enzyme used in the assay.

2.5.4 DNB-reductase Activity Assay in cell crude extract

DNB-reductase activity in A549 cellular extracts in the presence of oxidoreductase inhibitors was determined by measuring the residual DNB content and the amount of formed daunorubicinol (DNBol) in the assay mixture using Liquid Chromatography- Mass Spectrometry (Orbitrap LC-MS, Thermo Fisher). The cellular extracts were extensively dialyzed as described previously, and their protein content was quantified. The assay mixture was prepared as follows and incubated at 37°C for 24 h: a volume of crude extract containing 150 µg of protein was incubated with 170 µM DNB, 0.2 mM NADPH, and 15 µM of each inhibitor dissolved in DMSO (or DMSO alone for the control), in 10 mM sodium phosphate buffer, pH 7. The volume percentage of DMSO added was always less than 3% of the final volume of 90 µL. A 26 µL aliquot of the reaction mixture was taken at the start of the reaction (representing the reference at starting time, t0) and reaction was stopped by the addition of final 10% (w/v) TCA, incubating on ice for 1 h, and centrifuged at 14,000 × *g* at 4°C for 15 min. The supernatants were collected and used for analysis. After 24 h, the reactions were stopped similarly to t0 and samples were analysed. The analysis was performed using an Orbitrap Exploris 120 mass spectrometer coupled to a Vanquish chromatograph, with a Phenomenex Proteo HPLC column (0.3 x 150 mm). The mobile phases consisted of 0.1% ultrapure formic acid in H_2O and acetonitrile, using a flow rate of 5 µL/min and the following gradient (phases A/B): 85/15 for 0.5 min, gradient to 10/90 in 11.5 min, followed by a wash phase (10/90) for 6 min and reconditioning to the initial conditions for 12 min. The injection volume was 2 µL. The mass conditions (DDA, data-dependent analysis) included MS^2 spectra scanning of compounds with m/z values of 528.1864 and 530.2021 (corresponding to DNB and DNBol, respectively). MS^2 scans were performed at a resolution of 15,000 and a collision energy of 30. Product quantification was carried out using fragments with m/z values of 363.09 and 365.10, respectively.

2.6 Intracellular Sorbitol Content Dosage

To quantify the intracellular sorbitol content, an in-house spectrofluorimetric assay using purified SDH as an ancillary enzyme was employed. Firstly, HLEC_F cells were rinsed with PBS containing 1 mM PMSF, then collected using a scraper and transferred in Eppendorf tube. Cellular lysis was performed by three rapid F/T cycles, followed by centrifugation at 4 °C for 15 min at 14,000 × *g*. The supernatant was retained, and protein content was quantified for the subsequent normalization. Samples underwent protein precipitation with the addiction of 1 M perchloric acid and centrifugation at 4 °C for 5 min at 14,000 × *g*. The resulting supernatant was brought to pH 7 by adding a KOH solution, and again centrifuged at 4 °C for 15 min at 14,000 × *g*. For the determination of sorbitol content, aliquots of the prepared supernatant were added to a reaction mixture (final volume 200 µL) containing 0.24 mM NAD^+ and 150 mU of purified SDH in 100 mM Tris-HCl buffer, pH 8. The reaction was initiated by the addition of NAD^+. Fluorescence was measured at an emission wavelength of 460 nm, with excitation at 355 nm, for a total time of 10 minutes at 37°C. Sorbitol concentration was determined using a calibration curve obtained performing the reaction described with known D-sorbitol concentrations ranging from 5–40 µM (**Figure 16**), and the results were normalized to the protein content of the samples.

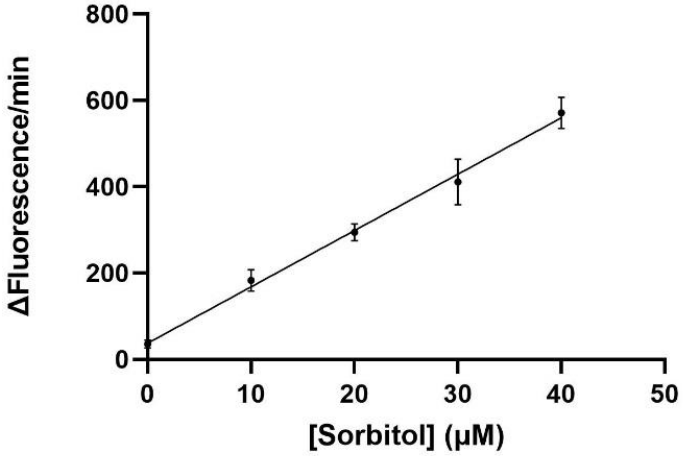

Figure 16. **Sorbitol calibration curve for intracellular sorbitol content quantification**. The reported calibration curve was obtained by performing the SDH-catalyzed oxidation of known sorbitol concentrations and measuring the fluorescence increase per minute due to NADH production. Data are reported as the mean ± standard deviation (SD) of three replicates. A linear regression fit resulted in the following equation: $y=13.05 x + 37.50$; $R^2=0.99$.

2.7 High Performance Capillary Electrophoresis (HPCE)

2.7.1 Intracellular Glutathione Content

To determine the intracellular glutathione content in $A549^{DNB}$ and $A549^{CONT}$, HPCE analysis was performed. Initially, both cell lines were plated in 100 mm diameter plates and, when confluent, washed twice with PBS, harvested by scraping and transferred in Eppendorf tube. Cell lysis was achieved through three rapid F/T cycles. Following lysis, the sample was centrifuged at 4°C for 30 min at 14,000 × g. Supernatant was retained, dosed for its protein content and divided in two aliquots. One aliquot was used to determine the reduced glutathione (GSH) content, thus immediately acidified by the addiction of 0.3 N HCl and ultrafiltrated by centrifugation at 14,000 × g for ~ 1.5 h at 4°C using 3,000 kDa Amicon® Ultra 0.5 mL Centrifugal Filters (Merk Millipore). The second aliquot was used for measuring the total intracellular glutathione content. This sample was firstly incubated with 5 mM DTT for 2 h at RT, then acidified and ultrafiltrated as described above. Metabolites in both samples were separated in 100 mM Tris Borate buffer pH 8.5 at a constant voltage of 30 kV and the elution profile was monitored at 214 nm. Glutathione concentrations were determined using a calibration curve made with standard concentrations of GSH and normalized with respect to its protein content (**Figure 17**).

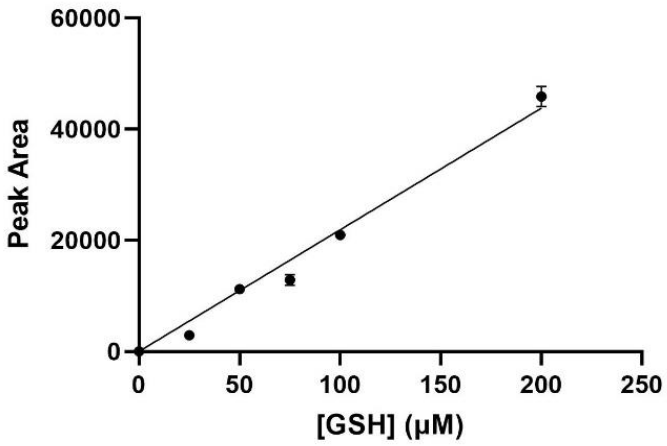

Figure 17. **Glutathione (GSH) calibration curve for intracellular GSH quantification** This calibration curve was generated by subjecting known concentrations of GSH to capillary electrophoresis. The elution peak area was calculated and plotted against the corresponding GSH concentration. Data are reported as the mean ± standard deviation (SD) of three independent replicates. A linear regression fit resulted in the following equation: y= 218.9 x.

2.7.2 Energetic Charge

HPCE analysis was also performed to investigate the variation in adenyl nucleotide profile, which was used to calculate the cellular energy charge. $A549^{DNB}$ and $A549^{CONT}$ were seeded at a density of 11,500 cells/cm^2 in 100 mm diameter plates. When confluent, cells were washed with PBS, trypsinized, and rapidly separated from the medium by centrifugation at 1,000 × g for 2 min. Resulting cell pellets were resuspended in 150 µL 1 M TCA, vortexed and subjected to three rapid F/T cycles to ensure complete cell lysis. The lysates were centrifuged at 10,000 × g for 5 min, and supernatants treated with ethyl ether to remove TCA, until pH was approximately 4.7. The samples were then subjected to electrophoretic separation, following the general procedure described by Cividini *et al*. [160]. Briefly, separation occurred in uncoated silica capillary (75 µM inner diameter x 115 cm total length), using a background electrolyte (BGE) solution consisting of 40 mM citric acid pH 4.8, with 1.2 mM hexadecyltrimethyl-ammonium bromide (CTAB, Sigma-Aldrich). The run was performed at a constant voltage of 30 kV with a ramp time of 0.5 min. Prior to each run, the capillary was washed with water for 1 min, followed by 0.1 M NaOH for 5 min, and water again for 1 min, and finally equilibrated with BGE solution for 2 min and maintained at 25°C. The elution profile was monitored at 254 nm, and area under the peaks corresponding to nucleotides of interest were analysed. The adenylate energy charge (EC) is calculated as follows:

$$EC = \frac{[ATP] + \frac{1}{2}[ADP]}{[ATP] + [ADP] + \{AMP\}}.$$

2.8 Quantification of the Firefly Luciferase Expression

The activation of NF-κB was quantitatively determined by measuring the activity of the Firefly luciferase reporter gene, which resulted in a luminescent signal. Initially, cell samples were prepared: culture medium was removed, cells were rinsed with PBS, and incubated with Passive Lysis Buffer (Promega), according to the protocol provided by manufacturer (Promega, Technical Bulletin 281 Revised 8/15). Then, a 100 µL aliquot of Luciferase Assay System (Promega) was added to 20 µL of the cell lysates, at 37 °C, for assaying luciferase activity. Moles

of luciferase were calculated referring to a standard curve reported in **Figure 18**, obtained by measuring the luminescence of different amounts of a commercially available Firefly luciferase (QuantiLuM, Promega), in the mole range between 10^{-15} and 10^{-19}. The measured moles of luciferase were normalized to the protein content of each sample.

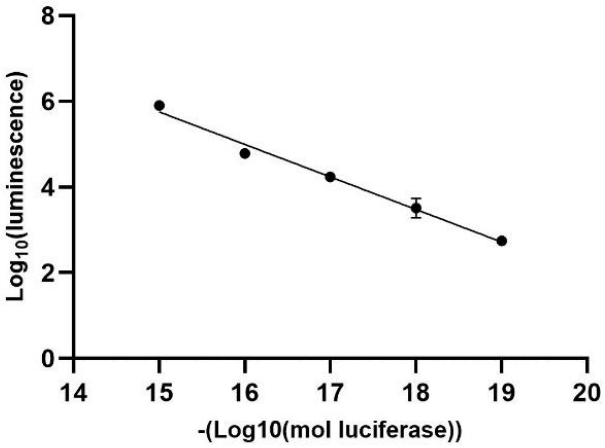

Figure 18. **Luciferase calibration curve for the quantification of the expressed moles of luciferase.** To produce the standard curve of light units versus relative enzyme concentration, serial dilutions of commercial recombinant firefly luciferase (QuantiLum® Recombinant Luciferase, Promega) were performed and reported in logarithmic scale. Data are reported as the mean ± standard deviation (SD) of three replicates. A linear regression fit resulted in the following equation: $y = -0.76x + 17.44$; $R^2 = 0.98$.

2.9 Western Blotting

Western blot analysis was conducted to detect the expression of several target proteins in all the studied cell lines. Cells were cultured in 100 mm diameter plates and harvested upon reaching confluence, as follows. Cells were rinsed twice with PBS supplemented with 1 mM PMSF proteases inhibitor. Cells were then collected with a cell scraper and lysed by means of three rapid F/T cycles, except for the cells used for COX2 detection, which were lysed by incubating them with 400 µl of a lysis solution, consisting of Lysis Buffer (Cell Signaling) properly diluted in ultrapure water with the same protease inhibitor used for washes, on ice for 5 min. Lysates were centrifuged at 14,000 × g for 30 min at 4°C, and the resulted supernatants were quantified for protein content and prepared for western blotting. A total of 10 µg of each sample (except for COX2 detection, which required 25 µg of protein) was diluted in sample buffer (250 mM Tris-HCl, pH 6.8 with 10% (w/v) sodium dodecyl sulfate (SDS), 30% (v/v)

glycerol, 0.05% (w/v) bromophenol blue salt) and 0.7 M β-mercaptoethanol, followed by incubation at 70°C for 10 min. Protein samples were loaded on 12% TGX Stain-Free™ FastCast™ Acrylamide Gels (Bio-Rad Laboratories, Hercules, CA, USA) and separated by electrophoresis at a constant voltage of 200 mV for 45 min. The gels were then exposed to UV light for 5 min using Chemidoc Image System device (Bio-Rad) for Stain-Free gel activation. Proteins were transferred to a 0.2 µm PVDF membrane, using precast Trans-Blot Turbo Transfer Pack Midi kit (Bio-Rad), by applying a constant current of 1.3 A with a maximum voltage of 25 V for 6 min, using a Trans-Blot Turbo Transfer System (Bio-Rad). Membranes were blocked for 1 h at RT with 5% (w/v) Nonfat dry milk (Cell Signaling Technology) in 50 mM Tris-HCl buffer pH 7.5, containing 150 mM NaCl and 0.1% (v/v) Tween® 20 (TBS-T). Membranes were incubated ON at 4°C with primary antibody. Finally, the appropriate horseradish peroxidase (HRP)-linked secondary antibody was incubated for 1 h at RT and immunoreactive bands were detected using Immobilon™ Western Chemiluminescent HRP substrate (Merck) and captured with the Chemidoc camera. The quantification of the immunoreactive bands was performed by means of the Bio-Rad ImageLab software, with the Stain Free technology (Bio-Rad) serving as a loading control. Utilized antibodies, along with their dilution and their host species are reported in **Table 4**.

TARGET	HOST	DILUTION	SUPPLIER	CAT #
AKR1B1	Mouse	1:1000	OriGene	TA346874
AKR1C3	Rabbit	1:2000	OriGene	TA327176
AKR1B10	Rabbit	1:1000	OriGene	TA344167
CBR1	Mouse	1:1000	OriGene	TA346903
SORD	Mouse	1:2000	OriGene	TA500747S
AKR1A1	Rabbit	1:1000	Antibodies.com	A40367
COX2	Rabbit	1:1000	Cell Signaling	12282T
Vimentin	Mouse	1:1000	Santa Cruz	SC-6260
Hrp-linked Rabbit IgG	Goat	1:1000	Cell Signaling	7074
Hrp-linked Mouse IgG	Mouse	1:1000	Cell Signaling	7076

Table 4. **List of antibodies used for Western Blot analysis.** For each antibody, the host species, dilution (in 5% Milk/TBS-T), and supplier with catalog number are provided.

2.10 RNA Extraction and Real-Time PCR

$A549^{DNB}$ and $A549^{CONT}$ cells were seeded in 100 mm diameter dishes and RNA was isolated using PerfectPure RNA Cultured Cell kit (5PRIME). Briefly, culture media were removed, cells were washed twice with PBS and lysed by incubation for 5 min at RT with Lysis Solution provided in the kit. To improve cell lysis, cell homogenate was passed through a syringe needle. RNA was isolated following the manufacturer protocol, and its concentration and purity were measured using Eppendorf BioSpectrophotometer. RNA integrity was evaluated through 1% (w/v) agarose gel electrophoresis. 500 ng of isolated RNA were reverse transcribed in a final volume of 20 µL, using Wonder RT cDNA Synthesis kit (Euroclone, cat. EME037050), following the manufacturer protocol. The cDNA synthesis was performed by the incubation of the reaction mixture in the MiniOpticon System (Bio-Rad), at 42° C for 30 min.

Real-time PCRs were carried out using the SensiFAST SYBR no-ROX kit (Meridian Bioscience, cat. BIO-98050) and the MiniOpticon System (Bio-Rad) in a final volume of 10 µL, following the general protocol provided by suppliers. The thermal cycling conditions were: 15 sec at 95°C and 30 sec at the primer-specific temperature (see **Table 5**) for 30 sec, repeated for 40 cycles.

Genes whose expression level was examined are reported in **Table 5**, along with the corresponding primer sequences and the annealing temperatures. Relative mRNA levels (Fold Change) of indicated target genes were calculated normalizing on the expression of two selected housekeeping genes, namely actin-β (ACTB) and Glyceraldehyde-3-Phosphate Dehydrogenase (GAPDH), through the ΔΔCt method.

Target	Forward primer (sequence and Ta in °C)		Reverse primer (sequence and Ta in °C)		Used Ta (°C)
AKR1A1	CTCAGATCTTGCTCAGGTGGC	60.7	TGGGACTCTCTTCCCATCCAC	60.9	60.8
AKR1B1	TTTTCCCATTGGATGAGTCG	55.7	CCTGGAGATGGTTGAAGTTGG	58.6	57.2
AKR1B10	AAAGCAACGTTCTTGGATGC	57.6	TGGAAGTGGCTGAAATTGG	56.7	57.1
AKR1C3	AAACTTCAACCGCAGGCAGC	62.1	TTCGGGTCCACCCATCGTTT	61.8	61.9
CBR1	AGCTGGACATCGACGATCTG	59.6	GTGCACACATCTCGGGTAC	58.2	58.9
SDH	GACTTGCGCCTGGAGAACTA	59.7	GCTTCATGTCCCAGCACCAT	60.7	60.2
E-Cadherin	AATCCCACCACGTACAAGGG	59.7	GGTATTGGGGGCATCAGCA	60.2	59.9
N-Cadherin	TGCATGAAGGACAGCCTCTTC	60.3	GCTTCTCACGGCATACACCA	60.4	60.4
GSTA4	CCGCCGGAGTCGAGTTTGAT	65.6	GGGCACTTGTTGGAACAGCA	61.4	63.5
GSTP1	TATTTCCCAGTTCGAGGCCG	59.8	TACAGGGTGAGGTCTCCGTC	60.3	60.1
MRP1	AGGACACGTCGGAACAAGTC	59.9	CGCATCCACCTTGGAACTCT	60.0	60.0
MRP5	AGAGGTGACCTTTGAGAACGCA	61.9	CTCCAGATAACTCCACCAGACGG	62.0	62.0
SOD1	ACTGGTGGTCCATGAAAAAGC	59.0	AACGACTTCCAGCGTTTCCT	59.9	59.5
SOD2	GGCCTACGTGAACAACCTGA	60.0	TTCCAGCAACTCCCCTTTGG	60.2	60.1
ACTB	AGCACAGAGCCTCGCCTTT	64.1	TACTCCTGCTTGCTGATCCA	62.3	63.2
GADPH	ATGGGGAAGGTGAAGGTCG	59.4	GGGGTCATTGATGGCAACAAT	59.6	59.5

Table 5. **List of primer sequences used for Real-Time PCR.** For each target gene, the forward and revers primer sequences alongside its specific annealing temperature (Ta), and the Ta used during reaction are reported.

2.11 Other Methods

2.11.1 Bradford

The protein content was quantified using the Bradford colorimetric assay [161]. Briefly, the samples were appropriately diluted in ultrapure water and incubated for 15 min at RT with 200 µl of Protein Assay Dye Reagent Concentrate (Bio-Rad) in a final volume of 1 ml. Absorbance at 595 nm was measured and converted to µg of protein using a calibration curve, generated by plotting the absorbance at 595 nm against known quantities of BSA (**Figure 19**).

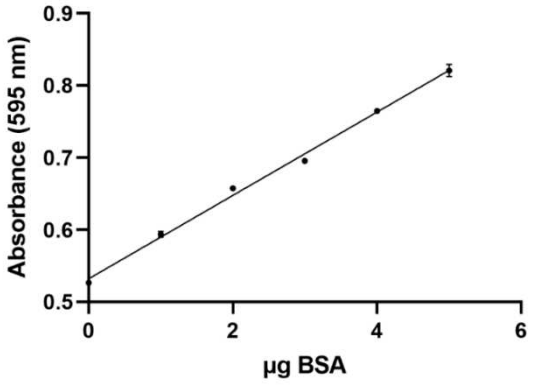

Figure 19. **Calibration curve for the protein content determination through Bradford assay.** The absorbance at 595 nm is plotted as functions of standard BSA quantities, expressed as micrograms of protein. Data are reported as the mean ± standard deviation (SD) of three replicates. A linear regression fit resulted in the following equation: y=0.06x + 0.53; R^2 = 0.99.

2.11.2 Chemicals preparation

DNB was dissolved in DMSO, and the exact concentration was determined by measuring the absorbance at 470 nm, using a molar extinction coefficient of 10.34 $mM^{-1} \cdot cm^{-1}$. The resulting DNB solutions were stored at -20°C. For all cell treatments, 10X DNB solutions solubilized in water were used. DNBol standard was prepared by reducing DNB with sodium borohydride ($NaBH_4$) dissolved in water, incubating the two reagents at a 1:7.2 ratio at 4°C in agitation for 30 min. The resulting standard can be stored at -20°C.

HNE was prepared from its diethyl acetal form, synthesized by Prof. Bellina's laboratory at the Department of Chemistry, University of Pisa, and stored in hexane at -80°C until use. After evaporating the hexane under a nitrogen (N_2) stream, the free aldehyde was obtained via acid hydrolysis of the diethyl acetal, by resuspending HNE in 1 mM HCl and maintaining the solution under agitation for 1 h at 4°C. The concentration of HNE was determined by measuring the absorbance at 224 nm, using an extinction coefficient of 13.75 $mM^{-1} \cdot cm^{-1}$.

GS-HNE and glutathione-nonanal (GS-nonanal) adducts were prepared by incubating HNE and trans-2-nonanal, respectively, with a reduced glutathione solution at a 1:1.5 ratio, in 50 mM sodium phosphate buffer pH 7.4, for 1 h at 37°C. The solution was then incubated ON at 4°C. The concentration of GS-HNE was determined by the difference between the initial and the residual HNE concentration, measured by absorbance readings at 224 nm. The concentration of GS-nonanal was determined by the difference between the initial GSH concentration and its

residual concentration at the end of the reaction, using the Ellman assay [4]. Both aldehyde-glutathione adducts were stored at -80°C.

2.12 Statistical Analysis

The data were statistically analysed using GraphPad Prism 9.0 software. All datasets were initially assessed for normal distribution and variance homogeneity, followed by analysis with the appropriate statistical tests, as specified for each result. For comparisons between two groups, Student's t-test was applied (or Mann Whitney nonparametric test if normality was not satisfied). One-way ANOVA with Tukey's post hoc test or, alternatively, Kruskal-Wallis nonparametric test was used for multiple group comparisons. To analyse the effect of two independent variables (specifically, DNB and the synthetic compound) on cell viability, a two-way ANOVA with Sidak's post hoc test was conducted. Unless otherwise specified, data derive from at least three independent experiments. Differences were considered statistically significant at p-values ≤ 0.05. Significance levels are indicated as follows: *: $p < 0.05$; **: $p < 0.01$; ***: $p < 0.001$; ****: $p < 0.0001$. SD: standard deviation; SEM: standard error of the mean.

CHAPTER 3: RESULTS AND DISCUSSION

3.1 Effects of the exposure to high glucose concentrations: the involvement of AKR1B1

3.1.1 High glucose levels slightly affect HLEC_F cell viability

To investigate the effects of exposure to high glucose concentrations on HLEC_F cells, cellular viability in response to increasing D-glucose concentrations (25–100 mM) over 24 and 48 h was monitored using MTT assay (**Figure 20**). The cell viability at each tested concentration was compared to those of cells cultured in the presence 5.5 mM, which well approximated the physiological blood glucose concentration in human, corresponding to 80-100 mg/dL. After 24 hours, none of the tested concentrations showed significant toxicity. However, at longer exposure times, D- glucose concentrations of 50 mM or higher induced a slight but statistically significant effect in a dose-dependent manner. Specifically, cell viability decreased by 10, 12, and 17% compared to control cells in the presence of 50, 75, and 100 mM D-glucose, respectively.

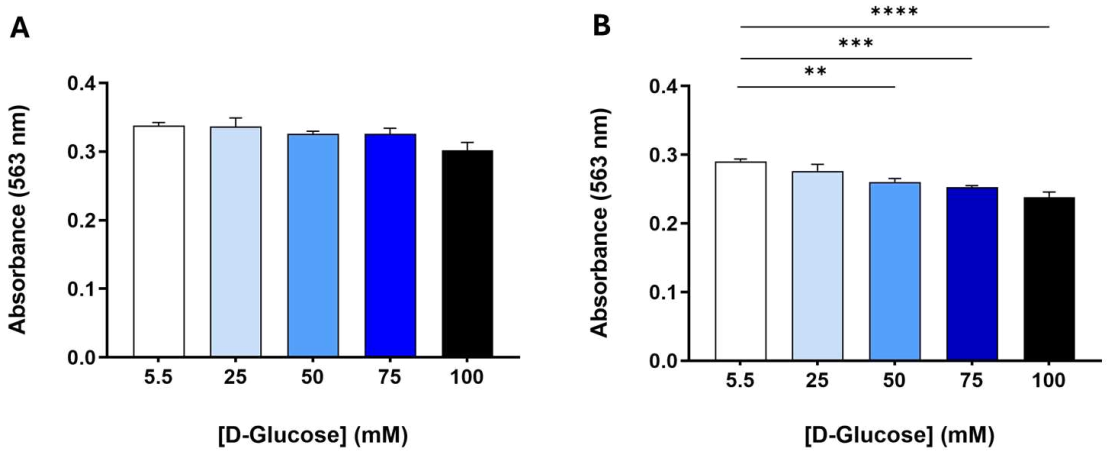

***Figure 20*. Effect of high glucose exposure on HLEC_F viability**. HLEC_F were maintained for 24 h (**A**) and 48 h (**B**) in complete medium supplemented with the indicated D-glucose concentrations. Cell viability was evaluated through MTT assay, monitoring the absorbance at 563 nm. All values are reported as the mean ± SEM of six independent measurements. Statistical analysis was performed using one-way ANOVA with Tukey post hoc test. Significance was evaluated with respect to cells incubated with physiological glucose concentration (5.5 mM). **: $p < 0.01$; ***: $p < 0.001$; ****: $p < 0.0001$

Notably, the general reduction in absorbance values observed after 48 hours of incubation cannot be attributed to a decrease in cell viability compared to cells incubated for 24 hours. On the contrary, referring to two separate experiments, the two graphs shown in **Figure 20** are not directly comparable. The observed difference in values is primarily due to experimental variability.

This result demonstrates the good resilience of this cell system to survive, at least for short periods, in the presence of elevated glucose concentrations. The human eye is highly susceptible to insults of both endogenous and exogenous origin. For this reason, ocular structures, including the lens, possess intrinsic antioxidant capacities and repair systems that protect against oxidative processes [162]. However, prolonged exposure to high glucose concentration induces excessive oxidative and osmotic stress, leading to cell death, which is a key factor in cataract development [163].

3.1.2 Sorbitol progressively accumulates in cells exposed to high glucose levels

High intracellular glucose concentrations drive its flux through the polyol pathway, whose activation in lens cells is considered one of the main mechanisms leading to diabetic cataract formation[164]. The first reaction in this pathway is catalysed by the enzyme AKR1B1, which converts glucose into sorbitol in an NADPH-dependent manner [165]. To assess the activation of the polyol pathway in HLEC_F cells exposed to high glucose concentrations, a fluorimetric method was developed to determine intracellular sorbitol levels and described in **Materials and Methods section**. The quantification of nanomoles of sorbitol, normalized to the milligrams of protein, in cells treated with different glucose concentrations is shown in **Figure 21**. As illustrated, cells cultured for 24 h in the presence of physiological glucose concentrations (*i.e.*, 5.5 mM) exhibit basal sorbitol levels below 20 nmol/mg of protein. These levels remain essentially unchanged when the D-glucose concentration in the culture medium is further progressively increased up to 50 mM. On the other hand, intracellular sorbitol levels result approximately 3-fold higher in cells incubated for 24 h with 75 mM D-glucose compared to cells grown under physiological glucose concentrations, and significantly higher than those in cells incubated with 25 and 50 mM glucose.

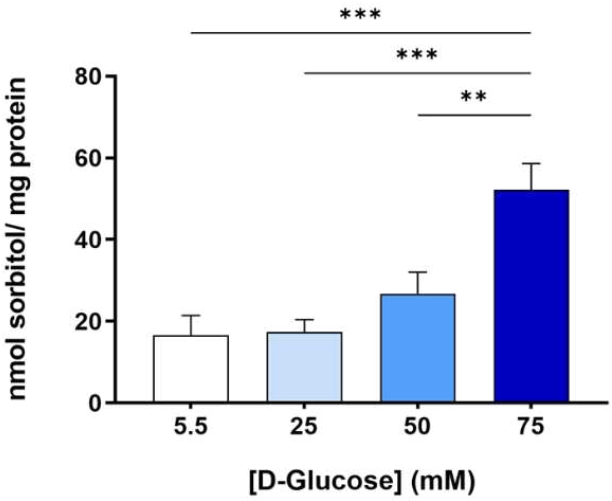

***Figure 21*. Sorbitol formation in response to increasing glucose concentrations.** HLEC_F were incubated in the presence of the indicated concentration of D-glucose, harvested after 24 h and the intracellular sorbitol concentration was measured. Sorbitol content is expressed as nmoles of sorbitol normalized to mg of protein and reported as mean ± SEM of measures of at least six independent experiments. Statistical analysis was performed through one-way ANOVA with Tukey post hoc test. **: $p < 0.01$; ***: $p < 0.001$.

A glucose concentration of 75 mM is extremely high and physiologically rarely achievable, where blood glucose levels of 15 mM already indicate a diabetic state [166]. However, since a 75 mM glucose concentration is slightly toxic only after 48 hours of incubation, and because it allowed for a better visualization of polyol pathway activation, it was used in subsequent experiments to investigate the role of the enzyme AKR1B1, a condition widely used in cultured cells for emulating the hyperglycemic status [167], [168], [169].

To assess whether intracellular sorbitol levels changed with increasing incubation time under high glucose concentrations, HLEC_F cells were cultured in the presence of 75 mM D-glucose for 24, 48, and 72 hours, and sorbitol content was subsequently analysed. As shown in **Figure 22**, while cells maintained under normal glucose concentrations show stable sorbitol level over time (white bars), sorbitol content in cells exposed to high glucose concentrations rapidly increases, reaching over 100 nmol of sorbitol per mg of protein after three days of treatment- approximately 9-fold higher than baseline sorbitol level. This result indicates that under these conditions, glucose flux through the polyol pathway remains active for at least three days after the first exposure to high glucose. Furthermore, this result suggests that sorbitol tends to

accumulate in the cells, implying that its rate of formation exceeds the rate at which it is converted into fructose, in the second step of the pathway.

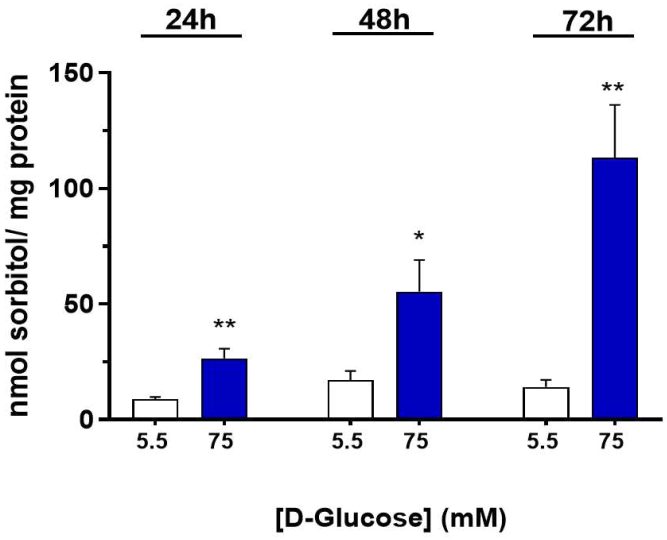

Figure 22. **Intracellular sorbitol accumulation following the exposure to high glucose concentration.** HLEC_F cells were incubated with the indicated D-glucose concentrations, harvested after 24, 48 or 72 h and the intracellular sorbitol concentration was measured. nmoles of sorbitol normalized to mg of protein are reported as the mean ± SEM of measures of at least nine independent experiments. Statistical analysis was performed through Student's T-test. *: $p < 0.05$; **: $p < 0.01$.

3.1.3 High glucose level exerts a pro-inflammatory action on HLEC_F

Hyperglycemic stress is known to trigger inflammatory responses in tissues by upregulating various transcription factors, including NF-κB [170]. The HLEC_F cell line is endowed with a reporter system that allows monitoring of NF-κB activation by measuring Firefly luciferase enzyme activity (see **Materials and Methods**). Before investigating the effect of high glucose stimulation on the activation of the inflammatory pathway, the efficacy of the reporter system was tested using a typical inflammation inducer, the proinflammatory cytokine TNF-α. As shown in **Figure 23**, treatment with 0.2 nM TNF-α resulted in the activation of the reporter system, as well as the overexpression of the NF-κB-regulated protein COX2, suggesting that this cell system responds to proinflammatory stimuli and is suitable for studying NF-κB pathway activation under hyperglycemic conditions.

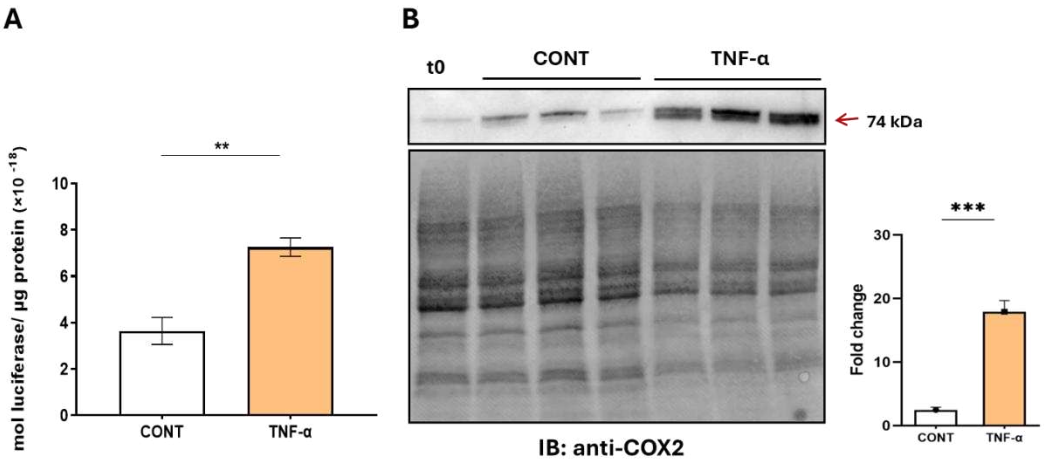

***Figure 23*. Response of the HLEC_F cell line to the classical pro-inflammatory stimulus TNF-α.** HLEC_F cells were incubated with 0.2 nM TNF-α dissolved in a human serum albumin (HSA) solution or with 175 ng/mL HSA (CONT) and harvested after 24 h for luciferase activity detection or after 48 h for COX2 expression analysis. Panel **A** displays the luciferase activation, as a reporter for the NF-κB pathway. Moles of luciferase normalized to µg of protein are reported as the mean ± SEM of measures of at least six independent experiments. Panel **B** shows COX2 expression level determined by Western blot analysis. Band intensities were normalized to the total protein content loaded and reported as fold changes relative to COX2 expression measured at time zero (t0) of incubation. Reported values derive from the mean ± SEM of six independent experiments. Statistical analysis was performed through Student's T-test. **: $p < 0.01$; ***: $p < 0.001$.

The HLEC_F cells were then stimulated with 75 mM D-glucose for 24 h, and NF-κB pathway activation was analysed. As shown in **Figure 24**, high glucose concentrations induce a marked activation of NF-κB and an overexpression of its downstream protein COX2 compared to the control, similarly to the effect exerted by the cytokine TNF-α. This confirms the pro-inflammatory action of glucose under the used experimental conditions.

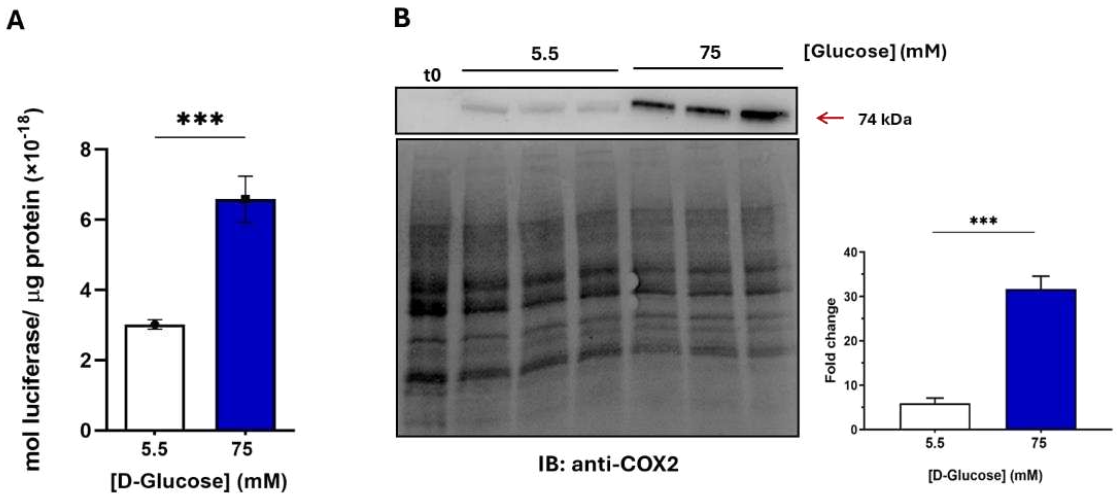

***Figure 24*. High glucose treatment induces inflammation response in HLEC_F cell line.** HLEC_F cells were incubated with the indicated D-glucose concentrations and harvested after 24 h for luciferase activity detection or after 48 h for COX2 expression analysis. Panel **A** displays the luciferase activation, as a reporter for the NF-κB pathway. Moles of luciferase normalized to µg of protein are reported as the mean ± SEM of measures of at least six independent experiments. Panel **B** shows COX2 expression level determined by Western Blot analysis. Band intensities were normalized to the total protein content in each respective lane and reported as fold changes relative to COX2 expression measured at time zero (t0) of incubation. Values derive from the mean ± SEM of six independent experiments. Statistical analysis was performed through Student's T-test. ***: $p < 0.001$.

Overall, these results demonstrate that 24 hours after stimulation with 75 mM D-glucose, HLEC_F cells activate both the polyol pathway and the NF-κB signalling pathway. This dual response raises the question of whether these two pathways are interconnected. Previous studies suggest a proinflammatory role for AKR1B1, although not through glucose reduction, but by means of its catalytic activity on GS-HNE, leading to the formation of GS-DHN, a known mediator of inflammation [171][153], [172]. Therefore, the involvement of AKR1B1 in glucose-induced inflammation in this cellular system was investigated.

3.1.4 The AKR1B1 inhibitor Sorbinil completely abolishes sorbitol accumulation, but it is apparently not sufficient to block inflammation

The role of AKR1B1 in the activation of the polyol pathway and NF-κB signalling pathway was assessed through its pharmacological inhibition. For this purpose, Sorbinil, one of the most potent and well-known inhibitors of AKR1B1, currently in phase III clinical trials for the treatment of diabetic complications [164], was selected. First, the toxicity of this inhibitor was evaluated by treating HLEC_F cells with various concentrations of Sorbinil for 24 and 48 h. As shown in **Figure 25**, no effect of Sorbinil, up to 100 μM, was observed on cell viability at each time point tested.

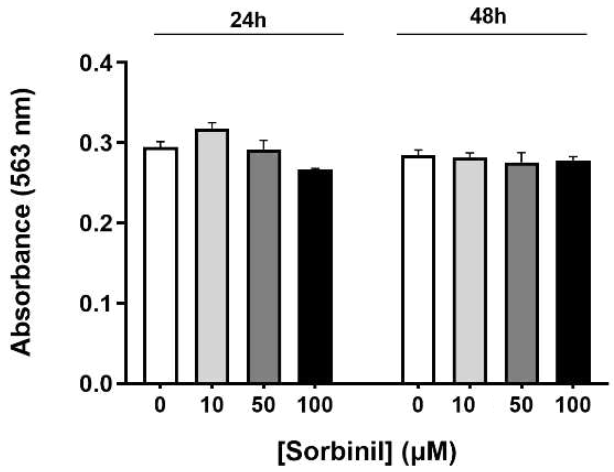

***Figure 25*. Evaluation of Sorbinil toxicity in HLEC_F cells**. HLEC_F were incubated for 24 h and 48 h with the indicated Sorbinil concentrations, in the presence of 0.05% (v/v) DMSO (final concentration) and under physiological glucose concentration (5.5 mM). At the indicated time point, cell viability was evaluated through MTT assay, monitoring the absorbance at 563 nm. All values are reported as the mean ± SEM of six independent measurements. Statistical analysis was performed using one-way ANOVA with Tukey post hoc test and significance was evaluated with respect to control cells (white bars).

Since cell viability was affected neither by the highest tested concentration of Sorbinil nor by 24-hour incubation with 75 mM glucose, it was assumed that the combination of these two factors would likewise not compromise cell viability. Nonetheless, further evaluation of this assumption could be of interest.

Therefore, the effect of AKR1B1 inhibition on intracellular sorbitol accumulation was investigated. HLEC_F cells were pre-incubated for 24 h with the highest non-toxic tested concentration of Sorbinil (100 μM) and subsequently stimulated with 75 mM D-glucose for

different times (**Figure 26**). Analysis of intracellular sorbitol levels revealed that AKR1B1 inhibition by Sorbinil results in the complete suppression of sorbitol formation at all time points tested, restoring sorbitol levels observed in unstimulated cells. This clearly demonstrates that AKR1B1 is the main responsible for sorbitol formation following high glucose exposure.

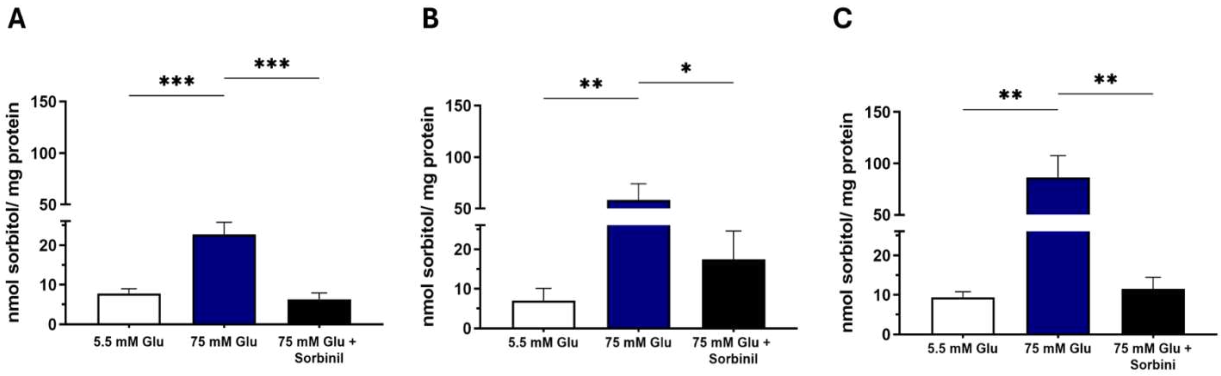

***Figure 26*. Evaluation of sorbitol levels upon AKR1B1 inhibition with Sorbinil.** HLEC_F cells were pre-incubated for 24 h with 0.05% v/v DMSO alone or supplemented with 100 μM Sorbinil (black bars) for 24h, and further treated with the indicated D-glucose concentrations. After 24 (**A**), 48 (**B**) or 72 (**C**) hours cells were harvested, and sorbitol content measured. Sorbitol content is expressed as nmoles of sorbitol normalized to mg of protein and reported as mean ± SEM of measures of at least six independent experiments. Statistical analysis was performed through one-way ANOVA followed by Tukey post hoc test. *: $p < 0.05$; **: $p < 0.01$; ***: $p < 0.001$.

Sorbinil was administered to HLEC_F cells in the presence of DMSO, which facilitates cellular uptake. Given that DMSO is reported to exhibit anti-inflammatory effects[173], [174], [175], it was necessary to determine the maximum concentration of DMSO that would not interfere with the NF-κB pathway. This control enabled the assessment of any impact of DMSO alone on NF-κB pathway activation, which otherwise could potentially confound the effect of Sorbinil. To this end, cells were incubated with increasing concentrations of DMSO (0.02%, 0.05%, and 0.1% v/v) for 24 h, followed by stimulation with 75 mM D-glucose for 24 h, after which luciferase activity was measured. As shown in **Figure 27**, 0.1% DMSO significantly reduced NF-κB activation, restoring the transcription factor to basal levels (indicated by a fold-change value of approximately 1). Thus, at a concentration of 0.1%, DMSO appears to counteract high-glucose-induced inflammation, and this concentration was excluded from further analyses. In contrast, the other two tested concentrations did not significantly reduce reporter gene expression

compared to the control condition without DMSO. The 0.05% DMSO concentration was selected as the final concentration for subsequent experiments with Sorbinil.

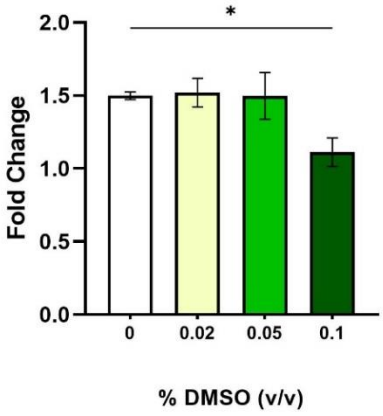

***Figure 27*. Effect of DMSO on luciferase expression induced by high glucose.** HLEC_F cells were incubated for 24 h with the specified DMSO concentrations (as % of final volume) before stimulation with 75 mM D-glucose (or an equal volume of PBS for unstimulated groups). After a further 24 h, cells were harvested, and luciferase activity was measured. Moles of luciferase, normalized to protein content, are shown as fold-changes relative to the unstimulated group containing the same DMSO concentration. Values are reported as the mean ± SEM of six independent measurements. Statistical analysis was performed using one-way ANOVA with Tukey post hoc test and significance was evaluated with respect to control cells (white bars). *: $p < 0.05$.

The effect of AKR1B1 inhibition on the inflammatory response was thus investigated. HLEC_F cells were pre-incubated for 24 h with 100 µM Sorbinil prior to their stimulation with 75 mM D-glucose, and Firefly luciferase activity was measured after 24, 48, and 72 h. As shown in **Figure 28**, AKR1B1 inhibition did not reduce NF-κB activation at any of the time points analysed.

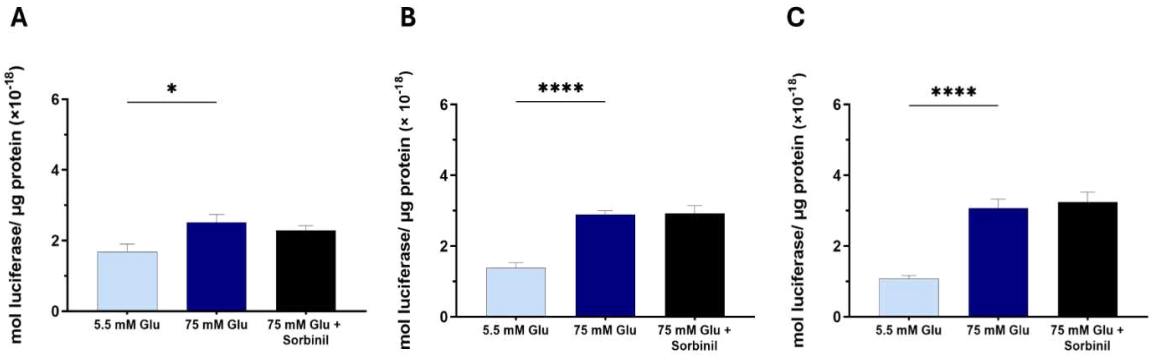

***Figure 28*. Effect of Sorbinil on NF-kB activation upon high glucose stimulation.** HLEC_F cells were pre-treated with 100 µM Sorbinil or 0.05% v/v DMSO for 24h, and then incubated with the indicated D-glucose concentration for 24 (**A**), 48 (**B**) or 72 (**C**) hours. Moles of luciferase normalized to µg of proteins are reported as mean ± SEM of measures of at least six independent experiments. Statistical analysis was performed through one-way ANOVA followed by Tukey post hoc test. *: $p < 0.05$; ****: $p < 0.0001$.

Similarly, COX2 protein expression levels remained unaffected by Sorbinil treatment (**Figure 29**).

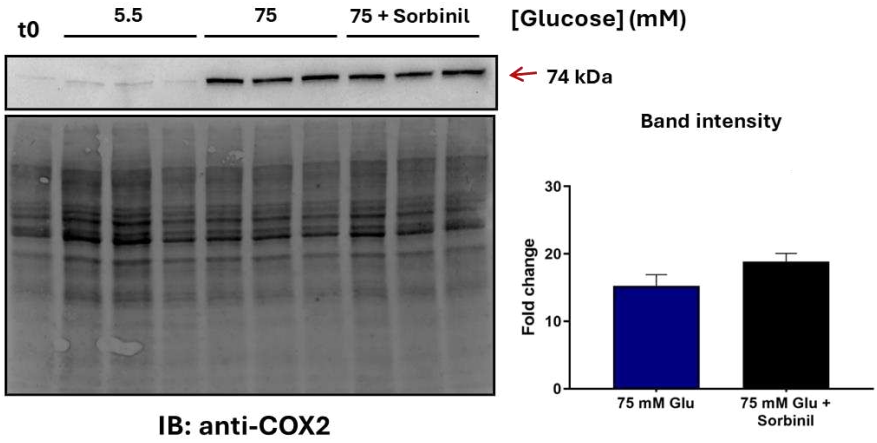

***Figure 29*. Effect of Sorbinil on COX2 expression in hyperglycemic conditions.** HLEC_F cells were pre-incubated for 24 h with 0.05% (v/v) DMSO alone or supplemented with 100 µM Sorbinil and then incubated with the indicated D-glucose concentrations for 48 h. COX2 protein levels were assessed by Western Blot analysis. Band intensities, normalized to the total protein in each respective lane, are expressed as fold changes relative to COX2 expression at the baseline (t0) of incubation. Data are presented as mean ± SEM from at least six independent experiments. Statistical significance was determined using Student's t-test.

Speculating that a D-glucose concentration of 75 mM might be excessively high and trigger an intense inflammatory response, which could mask the contribution of AKR1B1 on the activation of NF-κB pathway, a milder stimulus was investigated. Again, the inhibition of AKR1B1 with 100 µM Sorbinil did not demonstrate efficacy in reducing the activation of the inflammatory pathway when stimulated with a lower glucose concentration of 25 mM (**Figure 30-A**). Furthermore, similar result was obtained using a different pro-inflammatory stimulus, namely the cytokine TNF-α. As shown in **Figure 30-B**, no significant reduction in NF-κB activation induced by 0.2 nM TNF-α was detected in the presence of 100 µM Sorbinil.

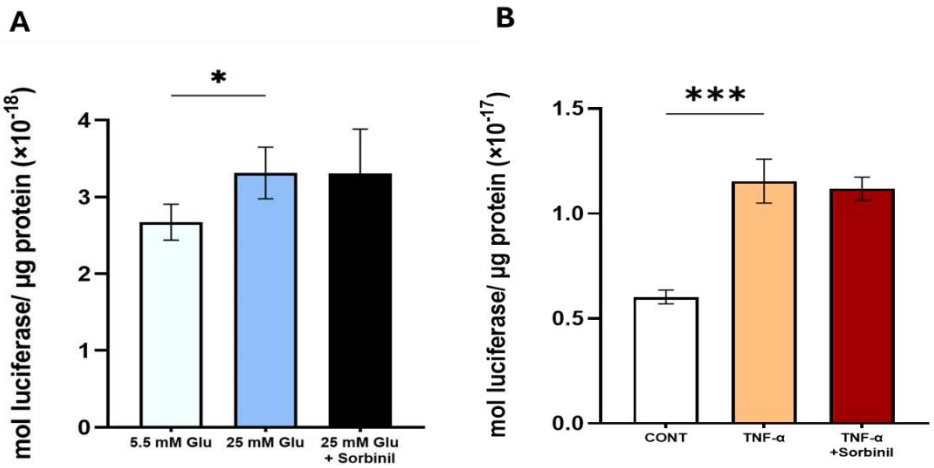

***Figure 30*. Effect of Sorbinil on NF-kB activation upon 20 mM D-glucose or TNF-α stimulation.** HLEC_F cells were pre-treated with 100 µM Sorbinil or 0.05% v/v DMSO (if not indicated) for 24h, and then incubated with the 25 mM D-glucose (**A**) or 0.2 nM TNF-α (**B**) for 24 h. Moles of luciferase normalized to µg of proteins are reported as mean ± SEM of measures of at least six independent experiments. Statistical analysis was performed through one-way ANOVA followed by Tukey post hoc test. *: $p < 0.05$; ***: $p < 0.001$.

Overall, in this cell model and under the reported conditions, complete inhibition of AKR1B1 was insufficient to prevent the onset of the inflammatory response induced by high glucose or TNF-α, contrary to what has been observed in several other cell systems[172], [176], [177], [178]. Interestingly, Ramana *et al*. [179] demonstrated that the AKR1B1 inhibition with Sorbinil in the same cell system used here (HLEC) was able to reduce inflammation induced by both high glucose and TNF-α, although the percentage of DMSO used was not clearly specified. The result presented here, regarding the effect of DMSO on NF-κB activation, underscores the importance of using DMSO-treated cells as controls. A significant reduction in NF-κB activation could be observed when comparing the action of Sorbinil with cells cultured in the absence of DMSO. However, making a proper comparison, no effect of Sorbinil on NF-κB activation was observed.

Apparently, hyperglycemia leads to a more complex response than the merely activation of the polyol pathway, culminating in the onset of a strong inflammatory state that persists, regardless of the impairment of sorbitol accumulation. The hyperglycemia-induced inflammatory process is therefore multifactorial, with AKR1B1 representing only one of the many key factors.

3.2 Effect of pharmacological treatment: the role of oxidoreductase enzymes in daunorubicin metabolism

3.2.1 Purified human AKRs and CBR1 enzymes exhibit daunorubicin-reductase activity in vitro

The clinical use of anthracyclines in oncology is limited by the development of severe side effects and the emergence of resistance mechanisms, which are associated with the metabolism of the anthracyclines themselves. Daunorubicinol (DNBol), an alcohol metabolite formed by the reduction of daunorubicin (DNB), is reportedly generated through a NADPH-dependent reduction catalysed by members of the aldo-keto reductase (AKR) superfamily and by carbonyl reductases (CBRs) [123]. Currently, AKR1A1, AKR1B10, AKR1C3, and CBR1 are considered the most efficient cytosolic reductases acting on DNB [180]. Thus, these four human recombinant enzymes were expressed and purified following the procedure described in the **Materials and Methods section** and tested for their DNB-reductase activity. The reaction rate of the purified enzymes was assessed using a 170 µM DNB solution as the substrate, with the consumption of NADPH monitored via fluorescence (excitation = 340 nm; emission = 450 nm). The results of the reaction rates for each enzyme are shown in **Figure 31**, depicting the change in fluorescence over time in relation to the amount of enzyme used. In all experimental conditions, a linear relationship between the reaction rate and the enzyme amount was observed, confirming the validity of the assay. Notably, a comparison of the graphs reveals a higher reductase activity towards DNB for AKR1A1 and CBR1 compared to AKR1B10 and AKR1C3. The latter enzymes exhibited DNB-reductase activity, but only when present at concentrations approximately 100 times higher than those of AKR1A1 and CBR1.

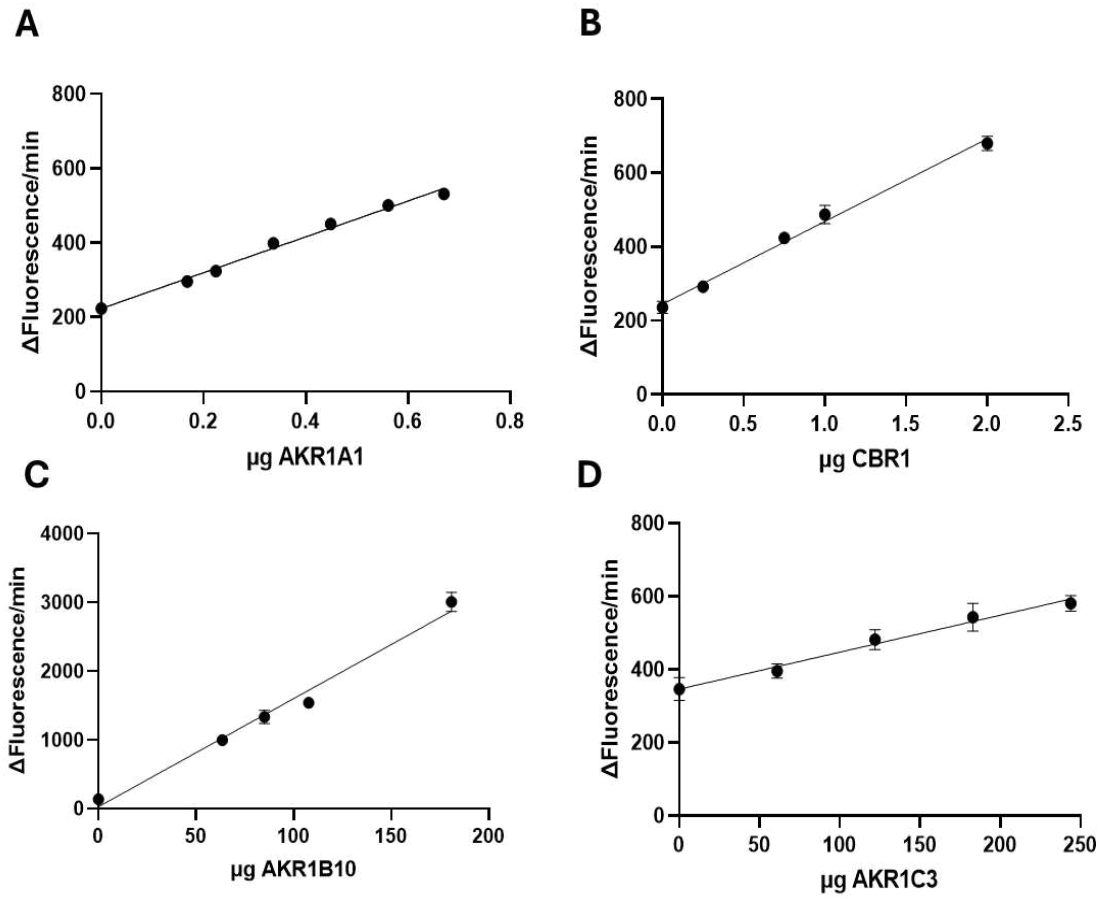

Figure 31. **Evaluation of DNB-reductase reaction rates of recombinant purified enzymes.** Human recombinant AKR1A1, CBR1, AKR1B10 and AKR1C3 were expressed and purified as described. Then, different amounts of each dialyzed enzyme were incubated with 170 µM DNB and 25 µM NADPH in in 50 mM sodium phosphate buffer, pH 6. The coenzyme oxidation was monitored by measuring fluorescence emission at 450 nm (excitation at 340 nm) for up to 20 min. The observed change in fluorescence over time was plotted against the respective µg of AKR1A1 (**A**), CBR1 (**B**), AKR1B10 (**C**) and AKR1C3 (**D**), used in the assay. The experimental values were interpolated using linear regression analysis. Each point represents the mean ± SD from at least three independent assays.

These results are only partially consistent with previous findings, which reported CBR1 as the most effective reductase (with a k_{cat}/K_m = 37,800 $s^{-1}\cdot M^{-1}$, [121]), followed by AKR1C3 (k_{cat}/K_m = 8,937 $s^{-1}\cdot M^{-1}$, [120]), AKR1B10 (k_{cat}/K_m = 2,752 $s^{-1}\cdot M^{-1}$, [120]), and lastly AKR1A1 (k_{cat}/K_m = 2,500 $s^{-1}\cdot M^{-1}$, [181]). The major discrepancy between our findings and those reported in the literature concerns AKR1A1, whose activity under our conditions was similar to that of CBR1. Nevertheless, it can be concluded that all the tested enzymes play a significant role in DNB reduction. Although some enzymes exhibit lower activity towards DNB compared to others,

their contribution cannot be overlooked, especially considering that the expression of these proteins is often upregulated in cancer [42], potentially leading to enhanced activity. Therefore, their inhibition could represent a potential strategy for addressing drug metabolism and chemoresistance.

3.2.2 A series of synthetic thiazolidinone derivatives shows inhibitory activity against human recombinant AKRs and/or CBR1

A group of thiazolidinone-derivative compounds, identified as compound 1, 2, and 3, and detailed in **Table 6**, has been designed and synthesized by Prof. Maccari's group from University of Messina.

Compound	Structure
1	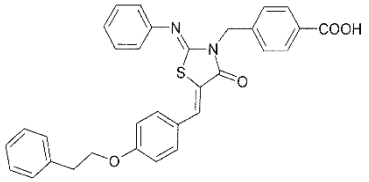
2	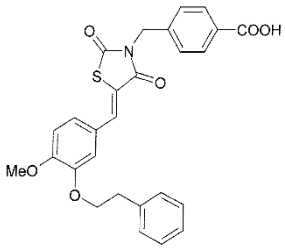
3	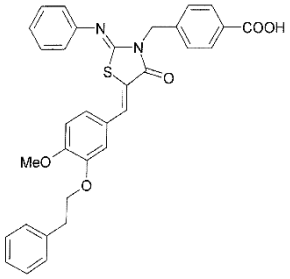

***Table 6.* Structures of novel thiazolidinone-derivative compounds.** The reported compounds 1-3, have been designed and synthetized by Prof. Maccari's group from University of Messina.

The inhibitory efficiency of each compound was tested on purified AKR1A1, AKR1B10, AKR1C3, and CBR1. Specifically, the effect of increasing concentrations of each inhibitor was evaluated by measuring the residual activity using the specific spectrophotometric assay for each enzyme (see **Subsection 2.5.1**). When possible, the concentration of inhibitor required to reduce the enzyme activity by 50% (IC_{50}) was calculated through non-linear regression analysis of the inhibition curves, shown in **Figure 32**. The resulting IC_{50} values are summarized in **Table 7**. Notably, it was not always possible to determine the IC_{50} value due to the structural characteristics of these compounds, which, beyond a certain concentration, interfered with absorbance measurements at 340 nm. In such cases, the residual activity (RA) observed in the presence of the maximum usable inhibitor concentration is indicated (**Table 7**, in brackets). Results indicate that compound 1 was selective toward AKR1A1 and CBR1 but appears less effective against AKR1B10 and AKR1C3. Conversely, compound 2 shows strong inhibition on AKR1B10 and, to a lesser extent, AKR1C3. Lastly, compound 3 demonstrates good inhibitory potential against both CBR1 and AKR1C3, but poor efficacy in inhibiting AKR1B10 and AKR1A1.

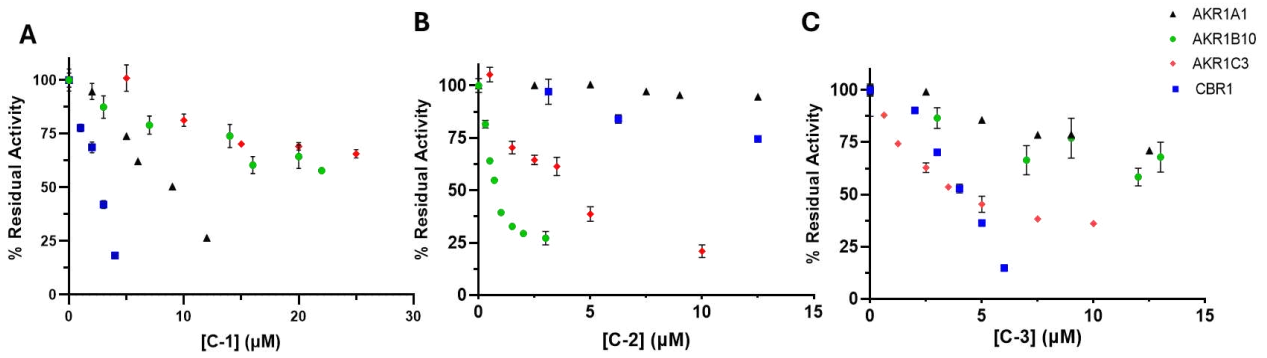

***Figure 32*. Inhibitory effect of compounds 1-3 on purified recombinant enzymes.** The enzymatic assays were performed as detailed in the **Materials and Methods section**. The reaction mixtures contained 0.7% (v/v) DMSO alone or in the presence of the indicated concentrations of compound 1 (**A**), compound 2 (**B**), and compound 3 (**C**). Each value is reported as the mean ± SD of at least three independent assays.

Enzyme	C-1	C-2	C-3
AKR1A1	8.3 ± 0.5 μM	ND (95% RA with 12.5 μM)	ND (71% RA with 12.5 μM)
AKR1B10	ND (68% RA with 22 μM)	0.7 ± 0.1 μM	ND (65% RA with14 μM)
AKR1C3	ND (65% RA with 25 μM)	6.0 ± 3.0 μM	3.0 ± 0.6 μM
CBR1	2.5 ± 0.3 μM	ND (75% RA with 12 μM)	4.0 ±0.1 μM

Table 7. **IC_{50} values of compounds 1-3 on purified recombinant enzymes.** Values were determined through non-linear regression analysis on inhibition curves reported in **Figure 32**, through GraphPad Prism 9.0. Where it was not possible to determine the IC_{50} (ND), the percentage of residual activity (RA) measured at the maximum concentration of inhibitor achievable was-reported.

Overall, these inhibitors exhibit good, albeit variable, efficacy against the different enzymes analysed, making them promising candidates for the inhibition of oxidoreductases in cells with the aim of enhancing the effectiveness of DNB.

3.2.3 Sensitivity to daunorubicin of A549 cell line

The sensitivity of the A549 cell line to the chemotherapeutic agent DNB was evaluated by incubating the cells for 24 hours with increasing concentrations of DNB (0–2.8 μM) and subsequently assessing cell viability using the MTT assay. The results are presented in **Figure 33**, in which the percentages of cell viability (calculated relatively to the control, in the absence of DNB) are shown for the different concentrations of DNB used. The resulting Half Maximal Effective Concentration (EC_{50}), namely, the concentration of the drug that induces a 50% reduction of cell viability, which is an indication of the toxicity of DNB in A549 cells under the experimental conditions, is 1.1 ± 0.1 μM. However, despite the further increases in DNB

concentration, above 2 µM cell viability did not fall below 35%. This suggests that none of the tested concentrations of the chemotherapeutic agent could achieve complete elimination of the cancer cells. Approximately 35% of the cells appear to be resistant to DNB and are able to survive a 24-hour exposure.

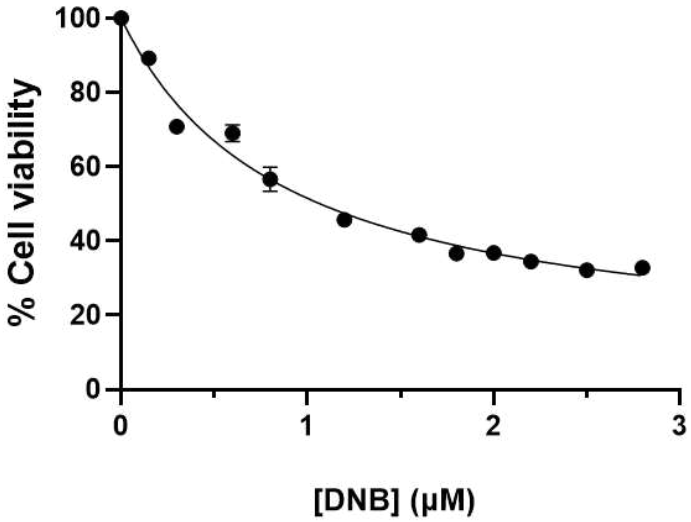

Figure 33. **Effect of DNB on cell viability.** A549 cells were incubated for 24 h with the indicated concentrations of DNB, and cell viability was subsequently evaluated using the MTT assay. The graph shows the percentage of cell viability calculated with respect to the control group (without DNB) as a function of DNB concentration. Each point represents the mean of six independent measurements ± SEM.

3.2.4 Selected compounds strongly improve the toxicity of daunorubicin after 24h

The effectiveness of compounds 1, 2, and 3, previously identified as inhibitors of DNB-reductase enzymes, in enhancing the cytotoxic action of DNB was evaluated. A549 cells were pre-incubated for 4 h with 5 µM of each inhibitor dissolved in DMSO, before exposure for 24 h to different concentrations (0, 200, 400, 800 nM) of DNB solution. At the end of the treatment, cell viability was assessed. The control group, used for normalization of cell viability, was treated in the same conditions in the presence of DNB but in the absence of inhibitors. The results are presented in **Figure 34**. Regarding compounds 2 and 3, they did not exhibit any

toxicity on their own and led to a highly significant improvement in DNB cytotoxic action. Specifically, compound 2, which was demonstrated to inhibit both AKR1B10 and AKR1C3, enhanced DNB toxicity only at DNB concentrations of 400 and 800 nM, decreasing cell viability by 14% and 18%, respectively. Compound 3, an inhibitor of AKR1C3 and CBR1, proved to be the most effective compound in enhancing DNB toxicity, reducing cell viability by 22% at the lowest DNB concentration (200 nM) and by 43% at both 400 and 800 nM of DNB. These results suggest that these inhibitors, particularly compound 3, could act as potential adjuvants, able to enhance the therapeutic effect of DNB even at lower concentrations of the chemotherapeutic agent. Different considerations need to be made on compound 1, since it exerts a toxic effect on A549 cells, as demonstrated by a significant reduction in cell viability even in the absence of DNB (**Figure 34-A**, white bars). Although an increase in toxicity is observed in the presence of DNB, it is difficult to distinguish between the compound's intrinsic toxicity and its efficacy in enhancing DNB cytotoxic effect and further experiments are required.

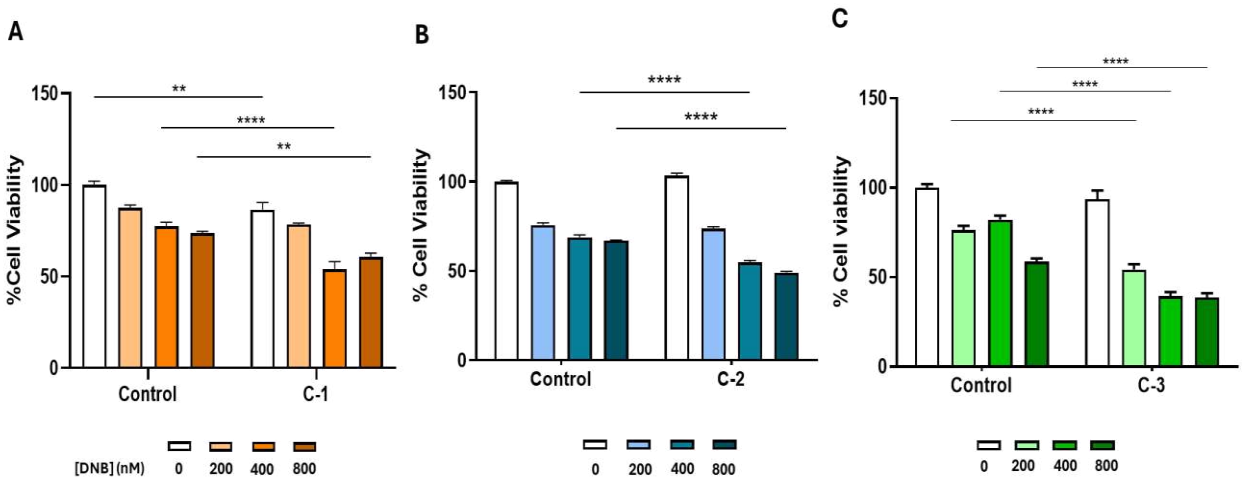

Figure 34. **Evaluation of the efficacy of compounds 1-3 in enhancing DNB toxicity.** A549 cells were pre-incubated for 4 h with 5 μM compound 1 (**A**), compound 2 (**B**) or compound 3 (**C**), followed by incubation with the indicated concentrations of DNB for 24 h. Cell viability was subsequently evaluated using the MTT assay, reported as the % of viability relative to the control condition, which was maintained in the absence of both the inhibitor and DNB. Each value represents the mean of five independent samples ± SEM. Statistical comparisons were performed between control and inhibitor-treated samples at each DNB concentration. A two-way ANOVA test was used for statistical analysis, followed by Sidak's post hoc test. **p < 0.01; ****p < 0.0001.

The effect of compounds 1-3 in inhibiting DNB reduction in crude extracts was also evaluated. Both the residual DNB and the produced daunorubicinol (DNBol) were measured through mass spectrometry analysis in cell crude extracts incubated for 24 hours with the anthracycline (170 μM) in the absence and in the presence of each inhibitor (see **subsection 2.5.4**). The results are shown in **Figure 35** and expressed in terms of fold change of the ratio (DNBol)/ (DNB + DNBol) measured in mixture containing 15 μM of each inhibitor with respect to the control mixture in the absence of inhibitors (in which a transformation of 70% of initial DNB was observed at the end of the incubation). Compounds 1 and 2 did not appear to affect DNB reduction, unlike compound 3, which was significantly effective in inhibiting DNB-reductase enzymes, thereby preventing the formation of DNBol.

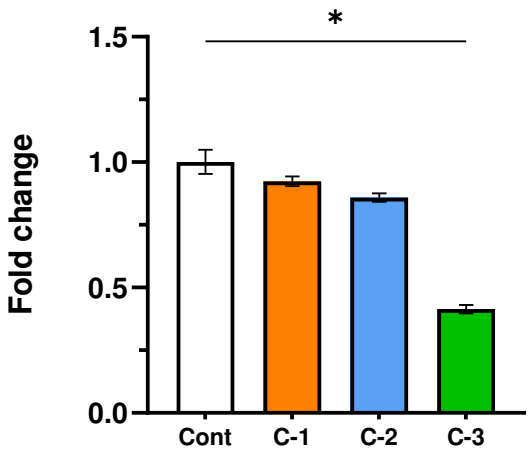

Figure 35. **Inhibition of DNB-reducing activity by compounds 1-3 in cell crude extracts.** The assays were performed as detailed in the **Materials and Methods section.** Briefly, 150 μg of protein from dialyzed A549 cell crude extract was incubated for 24h at 37°C with 3% (v/v) DMSO alone (Cont) or in the presence of 15 μM compounds 1-3. Each value is reported as the mean ± SD of at least three independent assays. Statistical analysis was performed through Kruskal-Wallis nonparametric test. *: $p < 0.05$.

Taken together, these results seem to suggest that the inhibition of the conversion of DNB into DNBol leads to an increased cytotoxicity of the chemotherapeutic agent itself, suggesting a potential therapeutic strategy to enhance DNB efficacy, while simultaneously mitigating the formation of its cardiotoxic metabolite. The three synthesized compounds showed good inhibitory capacity, although with different effectiveness, against all the enzymes tested. When combined with DNB, compounds 2 and 3 provided promising results in enhancing its antineoplastic efficacy, while the effectiveness of compound 1 is difficult to evaluate due to its intrinsic toxicity.

3.3 Characterisations of a DNB-resistant cell line

3.3.1 A549^{DNB} cell line appears morphologically different compared to A549^{CONT}

Given the observation that a subset of cells was capable of surviving in the presence of concentrations of daunorubicin, expected to be lethal for all the cells (see **Subsection 3.2.3**), a DNB-resistant (A549^{DNB}) cell line was generated, in order to preliminary characterise the primary mechanisms underlying this resistance.

The A549^{DNB} cell line was derived from the parental A549 cell line by culturing cells in complete medium with a sublethal concentration (50 nM) of DNB for a minimum of 4 weeks. In parallel, control cells (A549^{CONT}) were cultured under identical conditions, but in absence of DNB. The medium was refreshed every other day, and cells were maintained until they reached 90% confluence. At that point, the cells were detached and reseeded at a density of 9,000 cells/cm^2. Cell growth was monitored routinely through microscopy, and representative images were captured weekly, as shown in **Figure 36**.

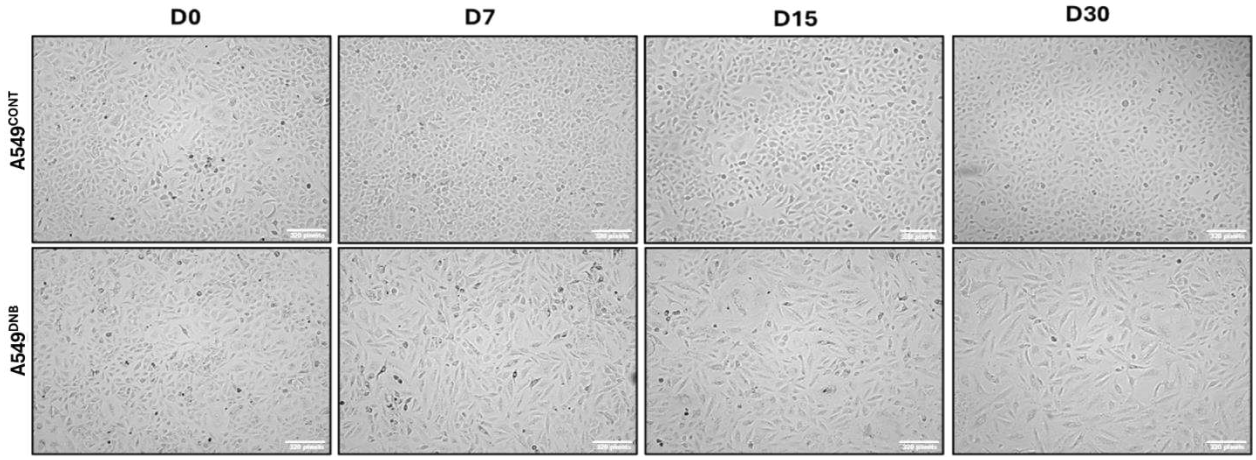

***Figure 36*. Time course of A549 DNB-resistant cell line generation.** The figure shows representative images of A549^{CONT} cells (cultured without DNB, upper images) and A549^{DNB} cells (maintained in the presence of 50 nM DNB, lower images) during the establishment of the resistant cell line. Images were taken at progressive time points: immediately after the first exposure to DNB (or DMSO solution for controls) (D0), after one week (D7), after 15 days (D15), and after 30 days (D30) from the initial exposure, using the JuLI Br Live Cell Movie Analyzer (NanoEnTek USA Inc., Waltham, MA, USA).

One week after the initial exposure to DNB, profound changes in cell morphology were observed when compared to the sensitive A549^{CONT} cells. Specifically, A549^{DNB} cells resulted larger in size and more irregular in shape, although the population remained heterogeneous. As the treatment continued, the A549^{DNB} population became more homogeneous, and cells exhibited more pronounced morphological differences, with a mesenchymal-like phenotype. A period of one month was determined to be the minimum time required to establish a homogeneous A549^{DNB} cell population, on which further analyses were conducted.

First, the resistance of the newly established A549^{DNB} cell line to DNB was assessed. Notably, while the control cells exhibited typical sensitivity to the anthracycline, with an EC_{50} of 1.4 ± 0.2 µM, the A549^{DNB} cells maintained over 75% viability even at 3 µM, the highest tested concentrations (**Figure 37-A**). When exposed to this DNB concentration, A549^{DNB} cells demonstrated a marked reduction in DNB sensitivity, with a 1.7-fold higher survival rate compared to A549^{CONT} (**Figure 37-B**).

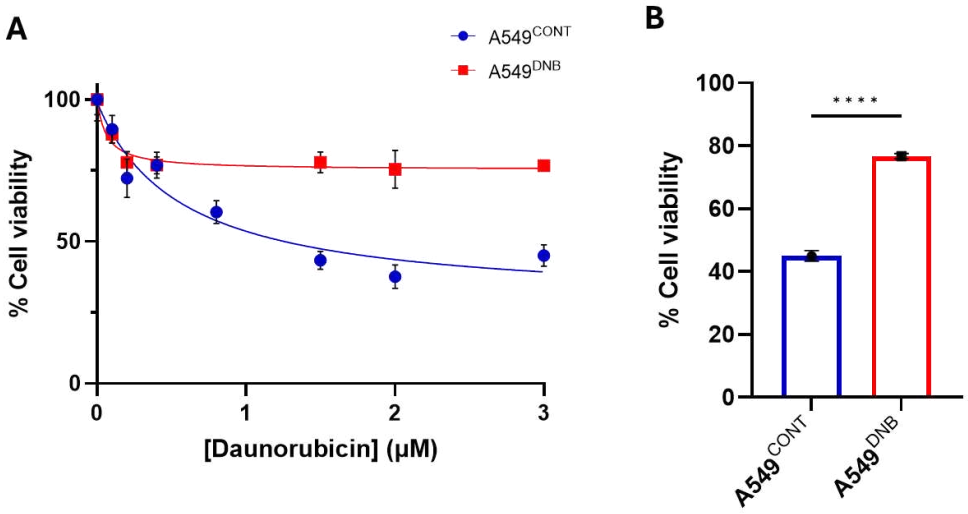

Figure 37. **Comparison of cell sensitivity to increasing concentrations of DNB between the two cell lines.** A549^{DNB} cells (indicated in red) and A549^{CONT} cells (indicated in blue) were incubated with the specified concentrations of DNB for 24 h, after which cell viability was assessed using MTT assay. Results are expressed as a % of the viability measured in cells without DNB exposure (0 µM DNB) for each DNB concentration tested (**A**). Data represent the mean ± SEM of six independent replicates. In panel **B**, the statistical comparison of viability between A549^{CONT} and A549^{DNB} cells exposed to the highest DNB concentration tested (3 µM) is shown, obtained with Student's t-test. ****: $p < 0.0001$.

Since anthracyclines exert their primary cytotoxic effect by interfering with DNA replication, and thus targeting actively proliferating cells, the proliferation rates of $A549^{DNB}$ and $A549^{CONT}$ cells were monitored. $A549^{DNB}$ cells exhibited a significantly lower proliferative capacity compared to $A549^{CONT}$ cells, as reported in **Figure 38**, in which an interval time of 72 h was examined.

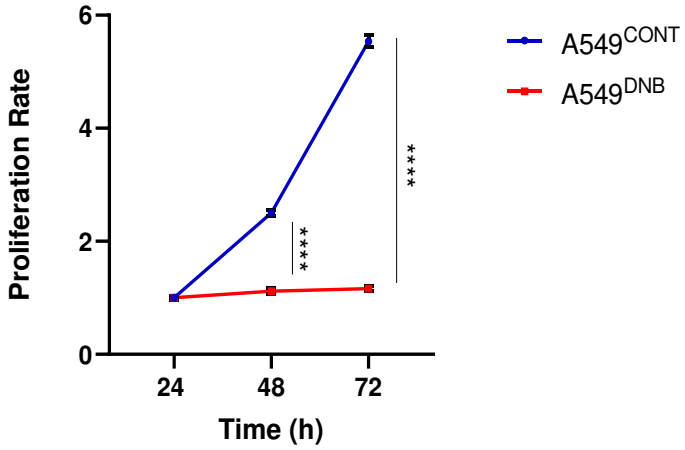

Figure 38. **Evaluation of proliferative capacity of the two cell lines.** The proliferation rate of $A549^{CONT}$ (in blue) and $A549^{DNB}$ (in red) cells was evaluated using the SRB assay at 24, 48, and 72 h from the cell seeding. Values are reported as the proliferation rate relative to measurements at 24 h and expressed as the mean ± SEM of six independent experiments. Statistical comparisons at each time point were conducted using Student's t-test. ****: $p < 0.0001$.

The reduced proliferative capacity of $A549^{DNB}$ cells make them less susceptible to DNB action. In this context, to confirm the actual acquisition of chemoresistance, DNB sensitivity will be evaluated at the specific duplication time of $A549^{DNB}$ cells, rather than at the previously assessed 24-hour.

Recently, it has been hypothesized that the presence of a subpopulation of quiescent cells, intrinsically less proliferative, may undergo a process of selection, adaptation to the new growth conditions, and subsequent expansion. This process likely contributed to the emergence of a fully chemoresistant cell line [139], [141]. Our observations are consistent with these findings, although further analysis is needed.

3.3.2 *A549^{DNB} cell line shows mesenchymal-like properties*

During the one-month incubation of A549^{DNB} cells with DNB, a progressive morphological change was visually observed, suggesting the onset of an epithelial-to-mesenchymal transition (EMT). In contrast, A549^{CONT} cells retained their epithelial characteristics throughout the same period.

To further investigate this aspect, the expression levels of key epithelial and mesenchymal markers, such as E-cadherin and N-cadherin/vimentin, respectively, was analysed. The results revealed a highly significant increase in both N-cadherin and vimentin levels in the A549^{DNB} cell line, while E-cadherin expression was significantly reduced compared to the control (**Figure 39**). Immunofluorescence analysis corroborated these findings, showing abundant vimentin expression in A549^{DNB} cells, along with marked differences in size and morphology compared to A549^{CONT} cells (**Figure 40**).

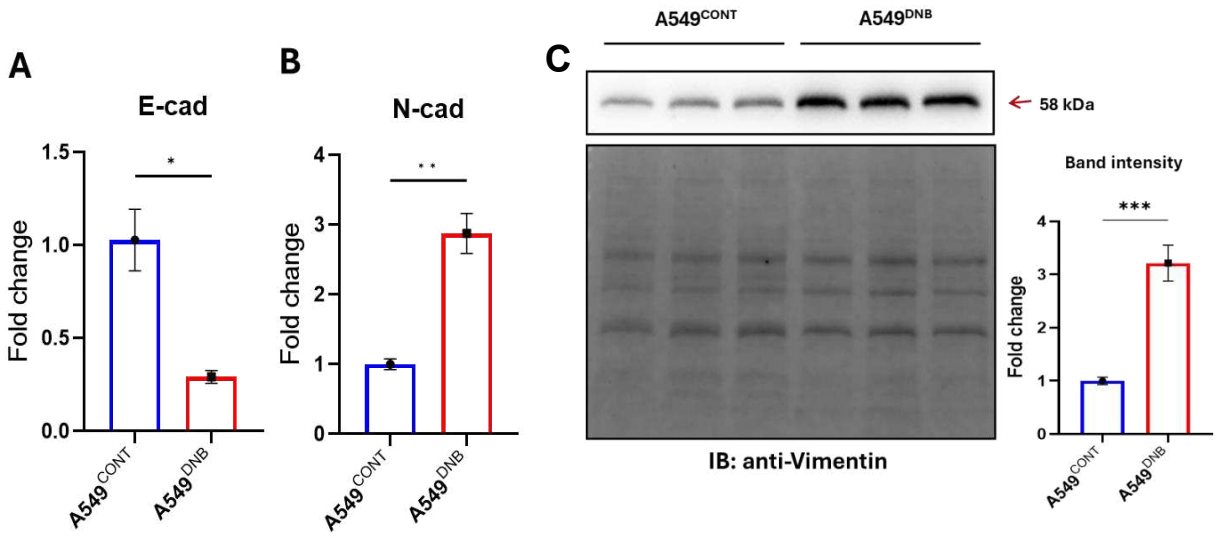

***Figure 39.* Evaluation of epithelial-to-mesenchymal transition marker expression.** Panels **A** and **B** show the fold change in expression of E-cadherin and N-cadherin, respectively, in A549^{DNB} cells (red) compared to control A549^{CONT} cells (blue), determined by Real-Time PCR using the ΔΔCt method. Panel **C** shows vimentin expression level in the two cell lines investigated determined by Western Blot analysis. Band intensities were normalized to the total protein content in each respective lane and reported as fold changes relative to the expression measured in A459^{CONT}. Values derive from the mean ± SEM of three independent experiments. Statistical analysis was performed through Student's T-test. *: $p < 0.05$; **: $p < 0.01$; ***: $p < 0.001$

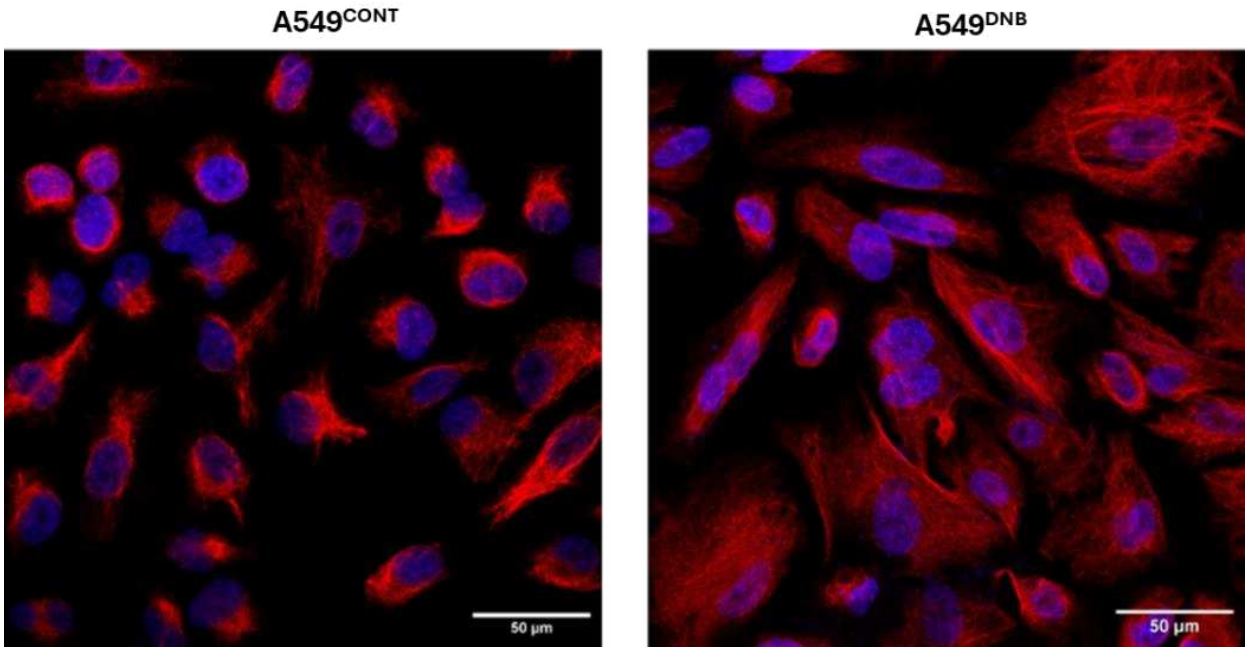

***Figure 40*. Confocal fluorescence microscopy images of vimentin immunostaining.** Representative images of A549^{CONT} (left) and A549^{DNB} (right) cells, immunostained as detailed in **Section 2.3**. Vimentin is shown in red; nuclei are stained with DAPI (blue). Images were acquired with Nikon Confocal Ax, using Plan Fluor 40 X Oil objective (Lens NA = 1.3; laser: 405, 488, 561 and 640 nm).

Another specific characteristic of mesenchymal cells is the invasiveness. To assess this, the migratory ability of the two cell lines was evaluated using a wound healing assay. A549^{DNB} cells displayed significantly enhanced mobility compared to the control cells after 24 hours, reaching the full confluence after 48 hours, unlike the control cells (**Figure 41**).

Lastly, given that both cell migration and metabolic reprogramming driving chemoresistance, and EMT require significant energy expenditure[182], we speculated that the two cell lines might differ in their energy status. Indeed, A549^{DNB} cells exhibited a significantly higher energy charge value compared to the A549^{CONT} cells (**Figure 42**).

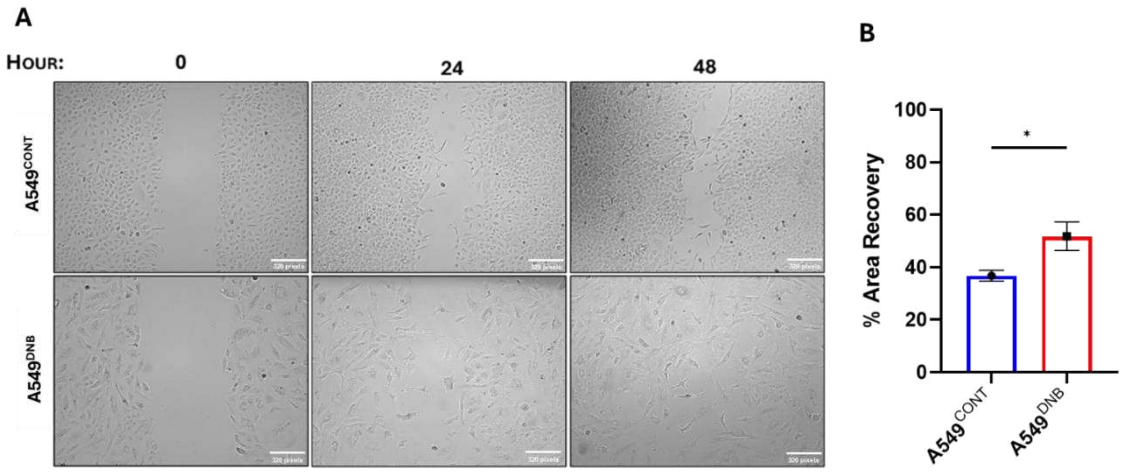

***Figure 41.* Comparison of migratory ability between the two cell lines.** The migratory capacity of A549^{CONT} (upper images) and A549^{DNB} (lower images) cells was evaluated using a wound healing assay as described in **subsection 2.2.3**. Panel **A** presents representative images captured immediately after wound formation (0) and after 24 and 48 h using the JuLI Br Live Cell Movie Analyzer (NanoEnTek USA Inc., Waltham, MA, USA). Panel **B** shows the measurement of area recovery after 24 h, performed with Fiji software (using the Wound Healing Size tool) for both A549^{CONT} (blue) and A549^{DNB} (red) cell lines. Values are expressed as the mean ± SD of three independent experiments. Statistical analysis was performed using Student's t-test. *: $p < 0.05$.

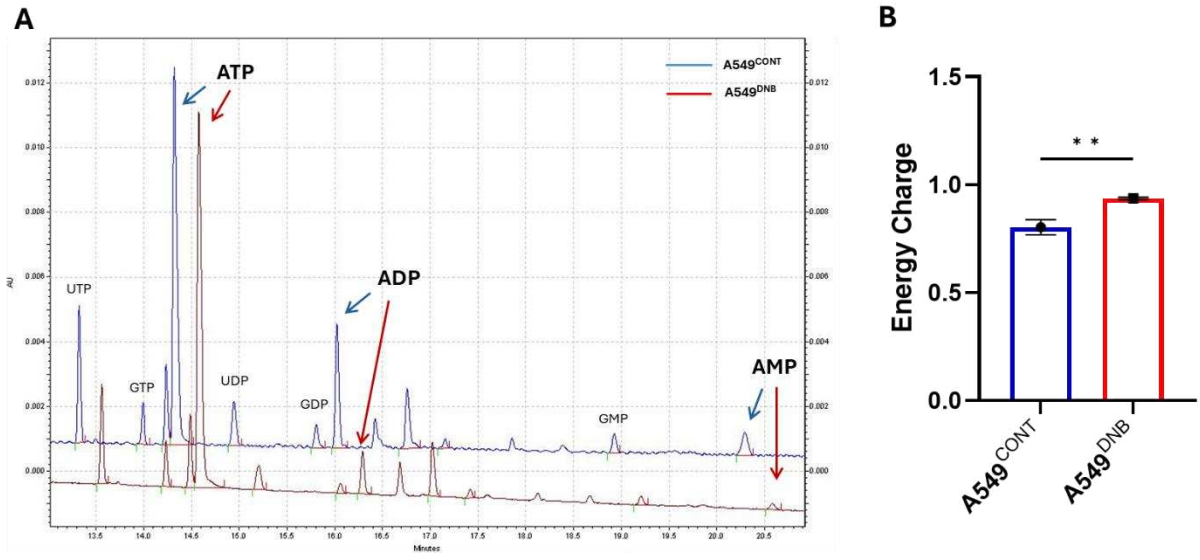

Figure 42. Adenylate energy charge evaluation in A549^{DNB} and A549^{CONT} lines. Adenylic nucleotide levels in A549^{CONT} and A549^{DNB} cell lines were measured by capillary electrophoresis, and energy charge was calculated as detailed in **subsection 2.7.2**. Panel **A** displays a representative electropherogram, showing the elution times and peaks of different nucleotides present in extracts from A549^{DNB} (red) and A549^{CONT} (blue) cells. The adenylic nucleotide peaks considered for energy charge analysis (shown in panel **B**) are indicated by arrows. Values are reported as the mean ± SEM of three independent experiments. Statistical analysis was performed using Student's t-test. **: $p < 0.01$.

Taken together, these results indicate that A549^{DNB} cell line exhibits profound phenotypic and metabolic-functional differences compared to the control cells. A549^{DNB} cells are less proliferative and display mesenchymal characteristics, including enhanced migratory capacity, along with the acquisition of mesenchymal morphology and markers. Additionally, the increased capability to survive in the presence of high doses of DNB suggests that A549^{DNB} cells might employ a series of detoxification mechanisms.

3.3.3 Preliminary screening of the expression of key genes associated with oxidative stress and acquired chemoresistance

To understand the mechanisms by which A549^{DNB} cells are able to survive at high levels of DNB, we analysed the expression of various genes involved in detoxification processes. One of the best-recognized mechanisms associated with anthracycline detoxification is the active extrusion of the drug from cancer cells [183]. Therefore, we investigated the expression of two multidrug resistance proteins (MRPs), namely MRP1 and MRP5. As shown in **Figure 43**, the expression of MRP1 was significantly elevated in A549^{DNB} cells compared to A549^{CONT} cells, consistent with numerous literature findings [110], [184], [185], [186], [187], [188]. MRP1 is one of the primary transporters of chemotherapeutic agents and facilitates the efflux of DNB in co-transport with reduced glutathione (GSH). It has been demonstrated that the inhibition of this transporter with verapamil increases cellular sensitivity to daunorubicin by preventing its exit from the cell [182]. In contrast, no significant differences in the expression of the MRP5 transporter were observed between the two cell lines. Supporting this result, although MRP5 has been shown to be important for the efflux of nucleotide-analogue classes of anticancer drugs [189], its specific function in mediating DNB transport and its involvement in acquired chemoresistance remain uninvestigated.

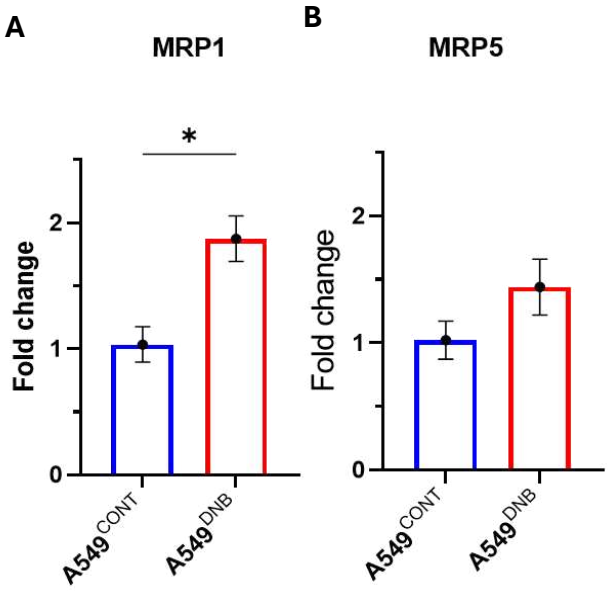

Figure 43. **Mulidrug Resistance Protein MRP1 and MRP5 expression in A549-derived cell lines.** Graphs show the fold change in expression of MRP1 (**A**) and MRP5 (**B**) in $A549^{DNB}$ cells (red) compared to control $A549^{CONT}$ cells (blue), determined by Real-Time PCR using the ΔΔCt method. Values derive from the mean ± SEM of at least three independent experiments. Statistical analysis was performed through Mann Whitney nonparametric test. *: $p < 0.05$.

Drug resistance is often associated with alterations in cellular glutathione concentration and/or in the activity and expression of Glutathione S-transferases (GSTs), which often resulted overexpressed [190], [191]. We analysed the expression levels of two enzymes belonging to the GST family, specifically GSTA4 and GSTP1. For both enzymes, a significant upregulation was observed in $A549^{DNB}$ cells compared to $A549^{CONT}$ cells (**Figure 44**).

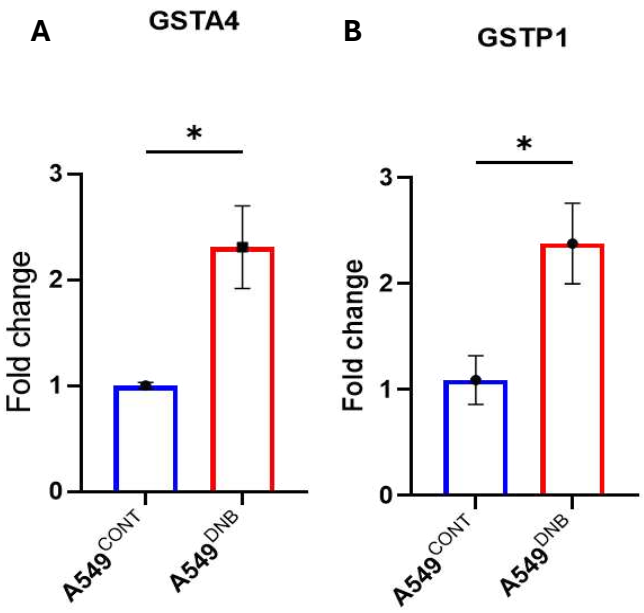

***Figure 44*. Glutathione S-Transferase GSTA4 and GSTP1 expression in A549-derived cell lines.** Graphs show the fold change in expression of GSTA4 (**A**) and GSTP1 (**B**) in $A549^{DNB}$ cells (red) compared to control $A549^{CONT}$ cells (blue), determined by Real-Time PCR using the ΔΔCt method. Values derive from the mean ± SEM of four independent experiments. Statistical analysis was performed through Student's T-test. *: $p < 0.05$.

Unlike other chemotherapeutic agents, anthracyclines do not undergo conjugation with glutathione (GSH) by GSTs, and the presence of GS-DNB adducts has never been detected neither *in vivo* nor *in vitro* studies[192]. Therefore, it is likely that the overexpression of these enzymes in resistant cells plays a significant role in the glutathionylation of other compounds generated by DNB activity, such as those resulting from oxidative processes. DNB is indeed responsible for inducing a strong oxidative stress response, and the hyperactivation of GST may serve as a defence mechanism against reactive species. In this context, as a preliminary investigation, the expression of superoxide dismutase enzymes (SOD) involved in detoxifying reactive oxygen species (ROS) was evaluated. The results, presented in **Figure 45,** demonstrate a clear hyperactivation of the genes encoding the two investigated isoforms of SOD, namely SOD1 and SOD2. Notably, the most significant hyperactivation was observed in the mitochondrial isoform, SOD2. It is relevant to highlight that, as described in detail in **Subsection 1.3.1,** DNB can interfere with the electron transport chain at the mitochondrial membrane and undergo one-electron reduction, promoting the formation of superoxide anions in this cellular compartment[91].

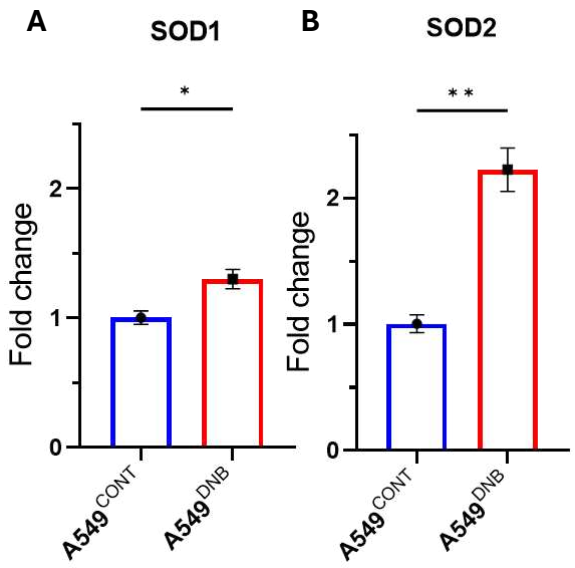

***Figure 45*. Superoxide dismutase SOD1 and SOD2 expression in A549-derived cell lines.** Graphs show the fold change in expression of SOD1 (**A**) and SOD2 (**B**) in $A549^{DNB}$ cells (red) compared to control $A549^{CONT}$ cells (blue), determined by Real-Time PCR using the ΔΔCt method. Values derive from the mean ± SEM of three independent experiments. Statistical analysis was performed through Student's T-test. *: $p < 0.05$; **: $p < 0.01$.

Finally, to monitor the redox status of the two cell lines, we quantified glutathione content, both in its reduced and total form, using high-performance capillary electrophoresis analysis. Surprisingly, a substantial depletion of glutathione was observed in the resistant $A549^{DNB}$ cells compared to the control $A549^{CONT}$ cells (**Figure 46**). Furthermore, no significant differences were found in the reduced glutathione and total glutathione for both cell lines, suggesting that all glutathione is present in its reduced form. Therefore, the marked decrease in intracellular glutathione in the $A549^{DNB}$ cell line can not be ascribed to oxidative processes, despite the constant presence of a pro-oxidant molecule. The low glutathione content could be an intrinsic characteristic of the newly established cell line or may result from the reduced proliferative capacity of $A549^{DNB}$ cells. Indeed, as demonstrated by Shaw *et al.*, there is a correlation between total intracellular glutathione levels and cellular proliferation. Specifically, they found that proliferating cells exhibit higher total glutathione levels compared to growth-arrested cells, and that mitogenic stimulation of quiescent cells leads to a two-fold increase in cellular glutathione content, consistent with our findings [193].

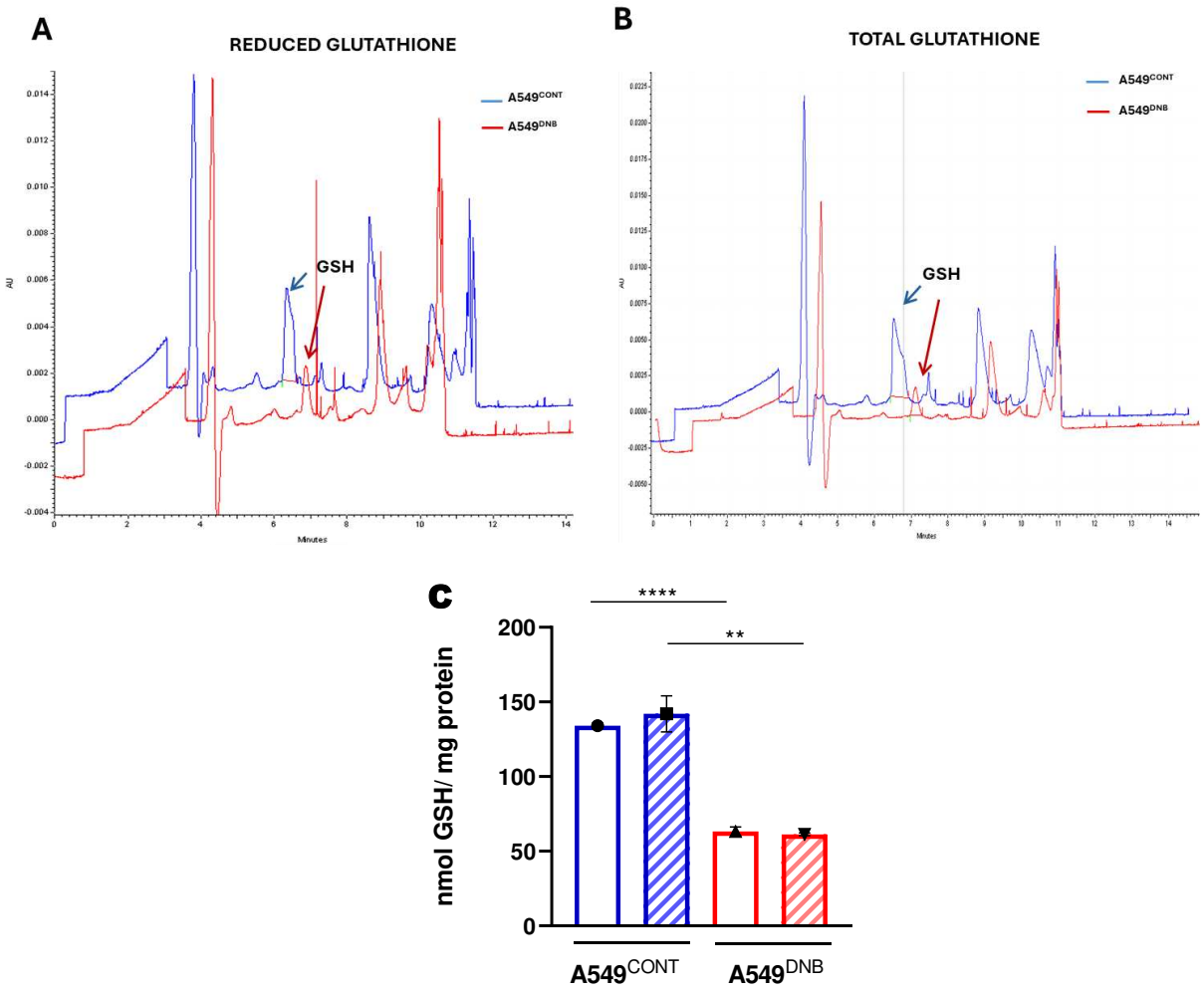

***Figure 46.* Evaluation of intracellular glutathione content in A549^{DNB} with respect to A549^{CONT} cells.** GSH levels in A549^{CONT} and A549^{DNB} cell lines were measured by capillary electrophoresis as detailed in **subsection 2.7.1**. Representative electropherograms from A549^{DNB} (red) and A549^{CONT} (blue) extracts, either directly acidified (**A**) or reduced and subsequentially acidified (**B**), are shown. Arrows indicate the GSH elution peak, considered further for analysis. Graph in panel **C** reports the quantification of glutathione content, expressed as nmol of GSH/mg protein, in A549^{CONT} (blue) and A549^{DNB} (red) cells. Solid bars indicate reduced fraction, while striped bars indicate the total amount of glutathione (both reduced and oxidated form). Values derive from the mean ± SEM of three independent experiments. Statistical analysis was performed through Student's T-test. **: $p < 0.01$; ****: $p < 0.0001$.

This preliminary analysis focused on the expression of key enzymes and transporters involved in multidrug response; however, it is possible that other factors may also contribute to the acquisition of chemoresistance. Future studies will aim to confirm the increased expression and activity of the identified upregulated markers through Western blotting and activity assays,

including the use of specific modulators, to elucidate their role in DNB resistance. Additionally, to gain a comprehensive understanding of the primary resistance mechanisms employed by $A549^{DNB}$ cells, it will be necessary to investigate the expression of other transporters and detoxifying enzymes.

3.3.4 $A549^{DNB}$ cell line has altered oxidoreductase enzyme expression and activity

The expressions of enzymes reported to possess DNB reductase activity, namely AKR1A1, AKR1B10, AKR1C3, and CBR1 were analysed at both transcriptional and translational levels, as shown in **Figures 47**, **48**, **49**, and **50**, respectively. A significant reduction in the transcriptional levels of all enzymes, except for CBR1 (**Figure 50-A**), was observed in the $A549^{DNB}$ cell line compared to $A549^{CONT}$ cells. However, this downregulation was not reflected in the analysis of the corresponding protein expression levels, which appeared unchanged between the two cell lines, except for AKR1B10, which instead exhibited significantly lower protein levels in the DNB-resistant cells compared to the controls (**Figure 48-B**). Intriguingly, this represents the first evidence of marked downregulation of AKR1B10 associated with a chemoresistant phenotype, and its significance warrants further investigation.

Furthermore, some oxidoreductase activities present in crude extracts from the two cell lines were analysed using different substrates, in order to at least partially cover the substrates specificity of AKR1A1, CBR1, AKR1C3, AKR1B10. In fact, due to a wide substrate overlapping, it is not possible to unequivocally measure the activity of each enzyme in cell crude extracts. Results reported in **Table 8** indicate that no differences were observed for activities that should be probably related to AKR1A1, CBR1, AKR1C3, AKR1B10 between the two cell lines.

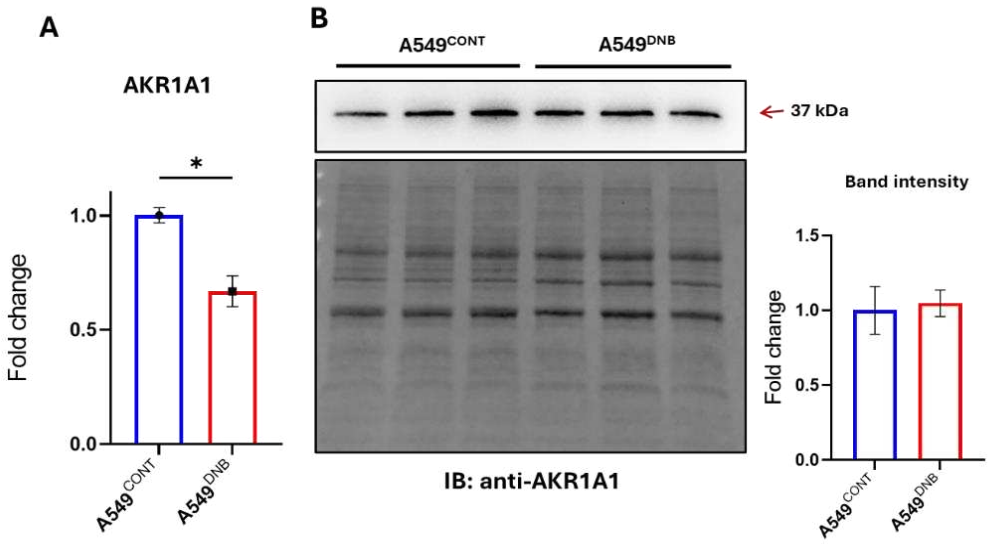

***Figure 47.* Evaluation of AKR1A1 mRNA and protein expression in A549^{DNB} *vs* A549^{CONT} cells.** Graph in **A** shows the fold change in expression of AKR1A1 in A549^{DNB} cells (red) compared to control A549^{CONT} cells (blue), determined by Real-Time PCR using the ΔΔCt method. Panel **B** shows AKR1A1 protein expression level in the two cell lines investigated determined by Western Blot analysis. Band intensities were normalized to the total protein content in each respective lane and reported as fold changes relative to the expression measured in the control line A549^{CONT}. Values derive from the mean ± SEM of three independent experiments. Statistical analysis was performed through Student's T-test. *: $p < 0.05$.

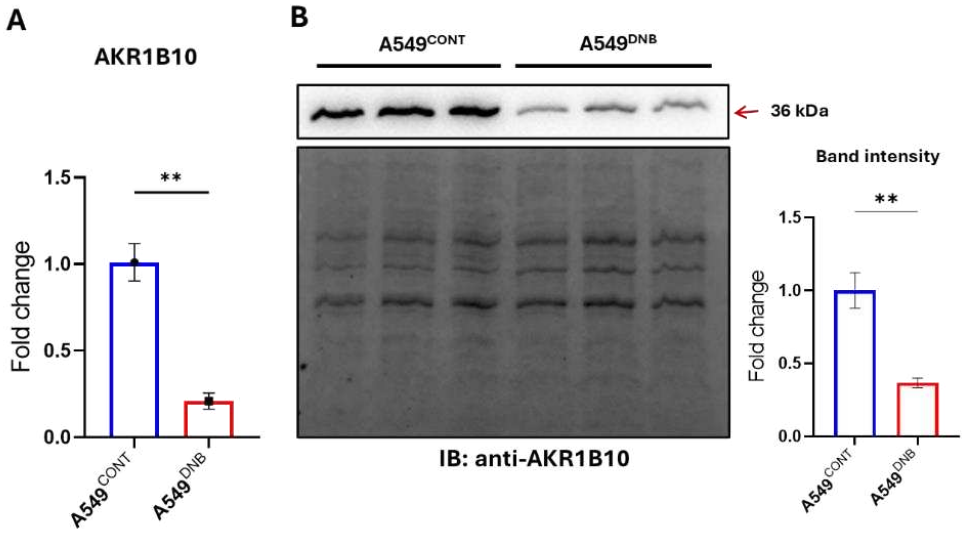

***Figure 48.* Evaluation of AKR1B10 mRNA and protein expression in A549^{DNB} *vs* A549^{CONT} cells.** Graph in **A** shows the fold change in expression of AKR1B10 in A549^{DNB} cells (red) compared to control A549^{CONT} cells (blue), determined by Real-Time PCR using the ΔΔCt method. Panel **B** shows AKR1B10 protein expression level in the two cell lines investigated determined by Western Blot analysis. Band intensities were normalized to the total protein content in each respective lane and reported as fold changes relative to the expression measured in the control line A549^{CONT}. Values derive from the mean ± SEM of three independent experiments. Statistical analysis was performed through Student's T-test. **: $p < 0.01$.

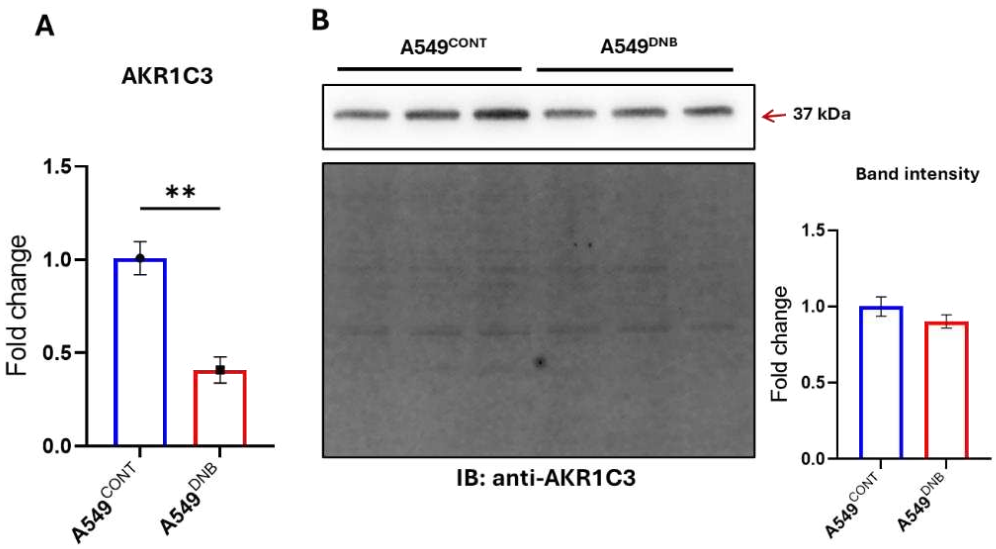

Figure 49. **Evaluation of AKR1C3 mRNA and protein expression in A549^{DNB} *vs* A549^{CONT} cells.** Graph in **A** shows the fold change in expression of AKR1C3 in A549^{DNB} cells (red) compared to control A549^{CONT} cells (blue), determined by Real-Time PCR using the ΔΔCt method. Panel **B** shows AKR1C3 protein expression level in the two cell lines investigated determined by Western Blot analysis. Band intensities were normalized to the total protein content in each respective lane and reported as fold changes relative to the expression measured in the control line A549^{CONT}. Values derive from the mean ± SEM of three independent experiments. Statistical analysis was performed through Student's T-test. **: $p < 0.01$.

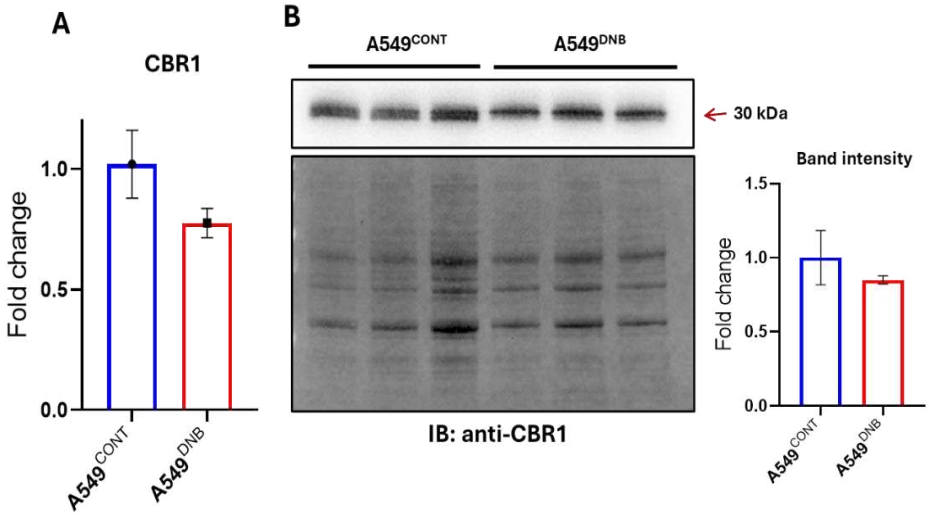

Figure 50. **Evaluation of CBR1 mRNA and protein expression in A549^{DNB} *vs* A549^{CONT} cells.** Graph in **A** shows the fold change in expression of CBR1 in A549^{DNB} cells (red) compared to control A549^{CONT} cells (blue), determined by Real-Time PCR using the ΔΔCt method. Panel **B** shows CBR1 protein expression level in the two cell lines investigated determined by Western Blot analysis. Band intensities were normalized to the total protein content in each respective lane and reported as fold changes relative to the expression measured in the control line A549^{CONT}. Values derive from the mean ± SEM of three independent experiments. Statistical analysis was performed through Student's T-test.

Finally, given the recent association between AKR1B1 and the polyol pathway with the EMT process[155], the expression levels of mRNA and protein for the two polyol pathway enzymes AKR1B1 and SDH were analysed. Concerning SDH, this enzyme resulted markedly increased at both the transcriptional and protein levels (**Figure 51**) in DNB-resistant cells compared to control cells. However, the enzymatic activity measured in crude extracts using fructose as a substrate did not show significant differences (**Table 8**). On the contrary, a significant increase in AKR1B1 protein levels in A549^{DNB} cells compared to A549^{CONT} cells were detected, while no changes at transcriptional level were observed between the two lines (**Figure 52**). Concurrently, the enzymatic activity of AKR1B1 was measured in cellular extracts, using L-idose as specific substrate, showing a 3-fold increase in A549^{DNB} cells compared to controls (**Table 8**). As detailed in **Subsection 1.3.4**, the enzyme AKR1B1 has been shown to be an important promoter of EMT in both cancer cells [148], [150], [152] and non-cancer cells [147], [154]. This strongly suggests a possible role for AKR1B1 in mesenchymal-like cells, although its specific function remains unknown.

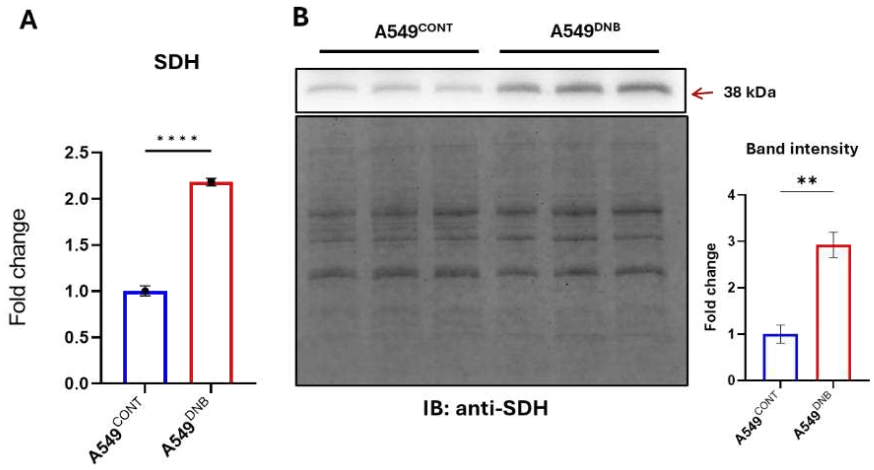

***Figure 51*. Evaluation of SDH mRNA and protein expression in A549^{DNB} *vs* A549^{CONT} cells.** Graph in **A** shows the fold change in expression of SDH in A549^{DNB} cells (red) compared to control A549^{CONT} cells (blue), determined by Real-Time PCR using the ΔΔCt method. Panel **B** shows SDH protein expression level in the two cell lines investigated determined by Western Blot analysis. Band intensities were normalized to the total protein content in each respective lane and reported as fold changes relative to the expression measured in the control line A549^{CONT}. Values derive from the mean ± SEM of three independent experiments. Statistical analysis was performed through Student's T-test. **: $p < 0.01$; ****: $p < 0.0001$.

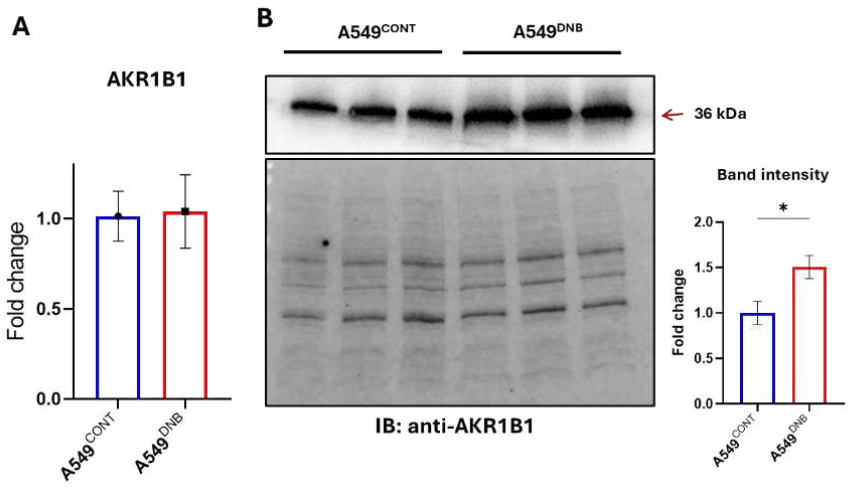

***Figure 52.* Evaluation of AKR1B1 mRNA and protein expression in A549^{DNB} *vs* A549^{CONT} cells.** Graph in **A** shows the fold change in expression of AKR1B1 in A549^{DNB} cells (red) compared to control A549^{CONT} cells (blue), determined by Real-Time PCR using the ΔΔCt method. Panel **B** shows AKR1B1 protein expression level in the two cell lines investigated determined by Western Blot analysis. Band intensities were normalized to the total protein content in each respective lane and reported as fold changes relative to the expression measured in the control line A549^{CONT}. Values derive from the mean ± SEM of three independent experiments. Statistical analysis was performed through Student's T-test. *: $p < 0.05$.

Substrate and cofactor	Activity (mU/mg)		Significance
	A549^{CONT}	A549^{DNB}	
L-idose, NADPH	47.2 ± 2.6	145.3 ± 15.4	***
D-fructose, NADH	14.5 ± 2.8	11.7 ± 1.7	NS
HNE, NADPH	51.5 ± 4.2	58.6 ± 7.4	NS
GS-HNE, $NADP^+$	16.6 ± 4.0	14.1 ± 4.7	NS
9,10-Phenanthrenequinone, NADPH	743.6 ± 135.9	781.3 ± 37.5	NS

***Table 8.* Evaluation of oxidoreductase activities in A549^{DNB} and A549^{CONT} crude extracts.** Different substrates covering, at least partially, the substrates specificity of AKR1A1, AKR1B10, AKR1C3, CBR1, were used. L-idose is used to specifically test AKR1B1 activity, while fructose in the presence of NADH allowed to monitor SDH activity. Values derive from the mean ± SD of three independent assays. Statistical analysis was performed through Student's T-test. ***: $p < 0.001$; NS: not significantly different.

CHAPTER 4: CONCLUSIONS

This study examines the cellular response to two distinct stimuli—a high glucose concentration, typical of diabetic conditions, and exposure to daunorubicin, a first-line chemotherapeutic agent—with a focus on understanding the significance of oxidoreductase activities in cellular processes related to both inflammation and chemoresistance phenomena.

Human lens epithelial cells exposed to elevated glucose levels displayed, as expected, a pronounced increase in sorbitol accumulation and a concomitant inflammatory response, evidenced by increased COX2 expression mediated via NF-κB activation. However, differently from several literature findings, in our conditions AKR1B1 inhibition affects only sorbitol accumulation while the inflammation induced by high glucose exposure resulted completely unaffected. This finding suggests, in HLEC_F, the contributions to inflammation from other, early-stage alterations which are not directly connected with AKR1B1. High glucose concentrations may therefore contribute to a generalized stress state, activating multiple pathways beyond the polyol pathway—such as increased glycolytic flux, the hexosamine pathway, glucose auto-oxidation, and AGE formation—indicating that AKR1B1 is merely one of several factors involved. In addition, considering the supposed role as pro-inflammatory compound of glutathionyl-dihydroxynonene produced by AKR1B1, the inefficacy of AKR1B1 inhibition in impairing the onset of inflammation in HLEC_F cells could be related to the presence in this cell line of other enzyme activities able to produce the pro-inflammatory molecule but not affected through AKR1B1 inhibition (as, for example, CBR1). Since AKR1B1 inhibition led to the complete impairment of sorbitol formation, this enzyme remains a validated pharmacological target for counteracting diabetic complications linked to sorbitol accumulation. Finally, given the detoxifying role of AKR1B1 acting on reactive aldehydes from lipid peroxidation, it is conceivable, though paradoxical, that AKR1B1 inhibition with Sorbinil could counterproductively exacerbate inflammatory processes. This underscores the potential value of differential inhibitors that selectively inhibit AKR1B1's role in glucose metabolism while preserving its detoxifying activity against reactive aldehydes like HNE, thus

maintaining its protective function[194]. A full AKR1B1 knockout, potentially through CRISPR-Cas9 technology, could clarify the enzyme's role in oxidative and glycative stress conditions.

Regarding DNB metabolism, enzymes with oxidoreductase activity, specifically AKR1A1, AKR1B10, AKR1C3, and CBR1, were confirmed to reduce daunorubicin to its corresponding alcohol, supporting their potential role as pharmacological targets to enhance chemotherapeutic efficacy. In this context, three thiazolidinone-derived inhibitors were identified, with promising effects when administered to cancer cells. Among these, compound C3, an inhibitor of AKR1C3 and CBR1, and compound C2, an inhibitor of AKR1C3 and AKR1B10, emerged as the most effective, reducing cell viability by up to approximately 43% and 16%, respectively, at DNB concentrations above 400 nM. This seems to support a preeminent role of AKR1C3 in the removal of DNB in A549 cells. The administration of compound C1, even in the absence of DNB, resulted in a significant decrease in viability, making it difficult to distinguish between its intrinsic toxicity and its efficacy in enhancing DNB activity. The fact that among the tested compounds only C1 resulted able to exert toxicity and to inhibit AKR1A1, may suggest a relevant role for this enzyme in detoxification events in A549 cells. Thus, a potential use of C1 in sensitizing cancer cells to oxidative damage, irrespectively to the presence of the chemotherapeutic agent could be envisaged.

Finally, the study of the cellular mechanisms associated to chemoresistance induced by pharmacological treatments also led to evaluate the cellular effect of low doses of the drugs over time. The observation of a subset of A549 cells insensitive to DNB prompted an investigation into the underlying mechanisms. A DNB-resistant cell line, designated as $A549^{DNB}$, was generated and characterized through prolonged incubation with low-dose DNB (50 nM). By the end of the incubation period, the cells exhibited significant morphological and functional changes, adopting characteristics typical of mesenchymal cells. Specifically, overexpression of N-cadherin and vimentin and concurrent downregulation of E-cadherin were observed. Resistant cells also exhibited increased motility and a decreased proliferation rate, along with differences in energetic charge and glutathione content compared to control cells, suggesting the presence of a distinct cellular population with respect to the parental cell line. A plausible explanation is that the parental A549 cell population included a minority of quiescent cells, often referred to as cancer stem cells (CSC), with reduced proliferative capacity, self-renewal ability, and intrinsic resistance to conventional chemotherapy due to

expression of efflux and drug-metabolizing genes (e.g., GST and MRP1). In their quiescent state, these cells likely underwent selection, expansion, and adaptation to new growth conditions during the incubation period, leading to the formation of a novel, chemoresistant cell line. Further analyses, including assessing the expression of known CSC markers (such as CD44, CD24, and CD133, [195])are required to confirm this hypothesis. The analysis of expression of the four oxidoreductase enzymes previously implicated in DNB metabolism, did not reveal any significant alteration, except for AKR1B10, which appeared downregulated. This suggests that these enzymes' activity may not be the primary detoxification mechanism under these cellular conditions. The downregulation of AKR1B10 could be associated with its role in retinaldehyde metabolism, which promotes cell proliferation. Thus, reduced AKR1B10 levels may contribute to the lower proliferative rate observed in $A549^{DNB}$ cells. Interestingly, the polyol pathway enzymes, AKR1B1 and SDH, were highly overexpressed in $A549^{DNB}$ cells, revealing a possible novel link between glucose metabolism and tumour aggressiveness. Consistent with our findings, AKR1B1 has emerged as a key promoter of EMT [146], [152], though its exact role in this process warrants further exploration. Intriguingly, AKR1B1 inhibition may thus offer a promising therapeutic approach for controlling cancer dissemination and metastasis.

APPENDICES

These appendices contain the main results achieved during the period of study and research abroad at the University of Surrey (Guildford, UK). During this time, I had the opportunity to study some matrix proteoglycans and metalloproteinases belonging to the ADAMTS family, introduced in **Section 1.3.4**. Specifically, two main aims were pursued: the enzymatic characterisation of the main substrates and interactors of recombinant ADAMTS9 metalloproteinase, and the expression and purification of recombinant human syndecan-4 ectodomain.

APPENDIX I: Characterisation of ADAMTS9 proteoglycanase activity

Introduction

Proteoglycans are macromolecules consisting of a core protein to which glycosaminoglycan (GAG) chains are covalently linked via a tetrasaccharide bridge [196]. They are present in the extracellular matrix (ECM) of nearly all tissues, where they play a crucial role in providing structural support, mechanical resistance, and tissue hydration due to their high hydrophilicity. Proteoglycans can also be located at the plasma membrane, exposed on the extracellular surface where they interact with ligands and signalling molecules, regulating their availability and interaction with cell receptors[197].

Proteoglycans are categorized based on the most abundant type of GAG chains attached to their core protein. These include proteoglycans with heparan sulfate (HS) such as syndecans, glypicans and perlecan [198], chondroitin sulfate (CS), like aggrecan, versican, decorin, and biglycan[199], dermatan sulfate (DS), and those with keratan sulfate (KS), such as keratocan and lumican [200]. Notably, hyaluronan is unique among GAGs as it does not attach to a core protein and consists of a simple, non-sulfated, sugar chain[197].

ADAMTS9 belongs to the subgroup of ADAMTS secreted enzymes endowed with proteoglycanase activity, with typical modular organisation detailed and depicted in **Figure 1** [201]. This enzyme is one of the largest in its family, with a predicted molecular weight of 216 kDa. This large size is due to the presence of 15 thrombospondin type I repeats within the ancillary domain, and the Gon-1 domain at the C-terminal end, the function of which remains unknown. The active form of ADAMTS9 is generated following the removal of the signal peptide and pro-domain, resulting in a molecular weight of approximately 184 kDa [202]**.** ADAMTS9 active site is very similar, both in sequence and 3D structure, to ADAMTS1, ADAMTS4, and ADAMTS5 suggesting similar cleavage site specificities. This hypothesis has been further demonstrated by Somerville *et al.*, although complete characterisation and identification of its major natural interactors are still lacking[202]**.**

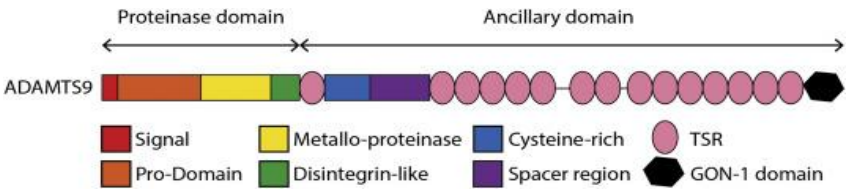

***Figure 1*. Schematic domain organization of ADAMTS9**. ADAMTS9 presents a N-terminal proteinase domain consisting of a signal peptide for entering the secretory pathway, a pro-domain which must be removed for enzyme activation, a metalloproteinase catalytic domain followed by non-catalytic ancillary domains including a disintegrin-like domain, a central thrombospondin-type I motif (TSR), a cysteine-rich domain, a spacer region, 14 additional TSRs and a Gon-1 domain at the C-terminus (figure from Desanlis *et. al* [252]). Similarly to the other ADAMTS proteins, the consensus sequence HEXXHXXGXXH located in the Mp domain (HELGHVFNMPH in ADAMTS9) constitutes the zinc-binding motif, where the three histidine residues coordinate a zinc atom, and together with a glutamate residue, exerts a catalytic role. This motif is followed C-terminally by a methionine residue that constitutes a structural turn (Met-turn) conserved within the metzincin family of metallopeptidases [201].

Evolutionary, ADAMTS9 is considered the oldest among the ADAMTS family members, showing sequence conservation with invertebrate proteases, which suggests a highly conserved physiological role[201]. It appears to play a critical role particularly during development, when cell migration through and upon the ECM is crucial to shaping and positioning the three germ layers endoderm, mesoderm, and ectoderm. In *Caenorhabditis elegans,* ADAMTS9 ortholog GON-1 is crucial for the migration of distal tip cells during gonadal morphogenesis, potentially by degrading the basement membrane and regulating extracellular signals required for cell migration[203]. Similarly, in *Drosophila melanogaster*, the ADAMTS9 ortholog AdamtsA is

essential during embryogenesis for the migration of multiple cell types, facilitating this process by clearing a path in front of migrating cells and promoting cell detachment from ECM [204].

In mammals, particularly in mice, ADAMTS9 is expressed in maternal and fetal tissues, early in embryogenesis and is crucial for regulating cardiovascular proteoglycans, which is vital for the proper organisation of the heart and large blood vessels [205]**.** The cardiac and vascular ECM plays a critical mechanical role, regulating cell migration and providing specific cues for migration and proliferation. Thus, defects in the ECM or its modifying enzymes can contribute to inherited and adult-onset cardiovascular disorders [206]. Loss-of-function studies of ADAMTS9 have highlighted its essential role in heart development. Mice homozygous for a null allele (*Adamts9*$^{-/-}$) died by embryonic day 7.5, before cardiovascular development occurs, while heterozygous mice (*Adamts9*$^{+/-}$) survived to adulthood but exhibited a range of cardiac anomalies due to the accumulation of versican in the myocardium and valves[206]. ADAMTS9 is thus proposed as a potential candidate gene for congenital valvular, aortic, and myocardial anomalies [206]. Despite its crucial role in heart development, many aspects of its functionality remain to be elucidated.

In order to characterise ADAMTS9 proteoglycanase activity, the Santamaria laboratory attempted expression of full-length FLAG-tagged ADAMTS9 in HEK293T cells. Unfortunately, this construct was rapidly degraded in the conditioned medium either in the presence or absence of heparin, which releases ADAMTSs from their binding to the ECM. A construct truncated after the Spacer domain (ADAMTS9 MDTCS) was then generated and transfected in HEK293T cells. This construct was successfully expressed and purified, accordingly to the expression and purification procedures of other recombinant ADAMTSs [207], alongside a similar construct, containing a Glu^{435}→Gln substitution in the active site, to serve as a negative control in digestion experiments (defined as ADAMTS9-EQ). The availability of purified ADAMTS9 MDTCS and EQ allowed to perform a first enzymatic characterisation, using different proteoglycans as substrates and an evaluation of inhibitory properties of natural inhibitors of ADAMTSs, belonging to the Tissue Inhibitors of Metalloproteinases (TIMPs) family.

Materials and Methods

Reagents

Purified recombinant ADAMTS9 MDTCS and ADAMTS5, which served as a positive control for proteoglycanase activity, were obtained at Santamaria's laboratory according to the standard procedure for ADAMTS expression and purification [208].

Full-length versican V1 (V1-FL) as well as its truncated version (V1-5GAG), were purified in the host laboratory as described by Santamaria *et al.* [207]. Aggrecan and biglycan from bovine articular cartilage were from Sigma-Aldrich. Recombinant TIMPs were from R&D Systems (Cat. n.: 970-TM, 971-TM, 973-TM, 974-TSF).

All the enzymatic reactions were conducted in TNC-B buffer (20mM Tris-HCl pH 7.5, 150mM NaCl and 10mM $CaCl_2$, 0.05 % Briji-35) and stopped with EDTA buffer (200 mM sodium acetate, 250 mM Tris/HCl pH 8.0 and 100 mM EDTA).

Aggrecan digestion assay

Aggrecan (667 nM) was incubated with increasing concentrations (0.1-500 nM) of ADAMTS9 MDTCS or 5 nM ADAMTS5 in TNC-B buffer, at 37°C for 2 or 24 h. The reactions were stopped with EDTA at the indicated time points, and solutions subjected to deglycosylation to remove GAG chains by incubation with 0.1 milliunits/µl of chondroitinase ABC and 0.1 milliunits/µl of keratanase overnight at 37°C. Then, samples were prepared for electrophoretic separation, adding reducing sample buffer (containing 5% β-mercaptoethanol) and heated for 10 min at 90°C. Samples were loaded in a 4-12% NuPAGE gel, run at 200 mV for 1 h, and blotted on membranes using Trans-Blot® Turbot Transfer System (BioRad). Membranes were probed with mouse monoclonal BC-3 antibody (1:250 in 0.5% BSA / PBS) detecting the ARGSV neoepitope formed by the cleavage at the Glu^{392}-Ala^{393} bond and mouse monoclonal 2B6 antibody (1:100 in 0.5% BSA/PBS) recognizing the CS stubs left following treatment of proteoglycans with chondroitinase ABC.

Versican digestion assay

V1-FL or V1-5GAG (each 100 nM) were incubated with increasing concentrations (0.1-100 nM) of ADAMTS9 MDTCS or 5 nM ADAMTS5 in TNC-B buffer, at 37°C for 2 or 24 h. The reactions were stopped with EDTA at the indicated time points and incubated with 0.1 milliunits/µl of chondroitinase ABC overnight at 37°C for deglycosylation. Then, samples were prepared and subjected to Western blotting as previously described for aggrecan assay. Membranes were probed with rabbit polyclonal anti-VC antibody (1:1000 in 0.5% BSA/PBS), recognizing the versican sequence ^{432}VPKDPEAAEARRG^{445} which contains the Glu^{441}-Ala^{442} cleavage site [209], and rabbit polyclonal anti-DPEAAE neoepitope antibody (1:1000 in 0.5% BSA/PBS), which only detects versikine, the N-terminal versican fragment generated after ADAMTS cleavage at Glu^{441}-Ala^{442} (UniProt ID: P13611-2).

Biglycan digestion assay

Biglycan (2 µM) was incubated with 500 nM ADAMTS9 MTDCS or 50 nM ADAMTS5 in TNC-B buffer, at 37°C for 24 h. The reaction was stopped with EDTA, and solutions underwent deglycosylation to remove GAG chains, incubating with 0.1 milliunits/µl of chondroitinase ABC overnight at 37°C. Samples underwent Western blotting following the procedure indicated for aggrecan assay, and membranes were probed with goat polyclonal anti-biglycan antibody (1:500 in 0.5% BSA/ PBS, R&D Systems, Cat. n. AF2667).

In vitro inhibition of versican cleavage with recombinant TIMPs

Before digestion, 100 nM ADAMTS9 MDTCS was preincubated with 500 nM recombinant TIMP-1, -2, -3 or -4 in TNC buffer for 1h at 37°. The reactions were started by the addition of 100 nM V1-GAG substrate, incubated 2h at 37° and stopped by the addiction of an equal volume of EDTA buffer. Solutions were deglycosylated with 0.1 milliunits/µl of chondroitinase ABC overnight at 37°, and finally prepared for SDS-PAGE. Samples were loaded in a 4-12% NuPAGE gel, run at 200 mV for 1 h, and blotted using Trans-Blot® Turbot Transfer System (BioRad). Membranes were probed with rabbit polyclonal anti-DPEAAE neoepitope antibody (1:1000 in 0.5% BSA/PBS) for versikine detection.

Quantification of versicanase activity by sandwich ELISA

ADAMTS9 MDTCS (50 nM) was incubated with 50 nM V1-FL or V1-5GAG at 37 °C in TNC-B buffer. At different time points (0–120 min), an aliquot of each sample was removed, and reaction was stopped with the addiction of EDTA buffer. The amount of versikine neoepitope generated in each reaction was measured by sandwich ELISA and finally quantified using a standard curve (0–1.56 nM) of V1-5GAG completely digested with ADAMTS5, according to the procedure reported in Santamaria *et al*. [207] (**Figure 2**). Briefly, 96-well Maxisorp plates (Nunc) were coated with 5 µg/mL anti-DPEAAE neoepitope antibody in 3% BSA/PBS (16 h, 4 °C), and blocked with 3% BSA/PBS (2 h, at room temperature, RT). Samples from digestion reactions were diluted in 3% BSA/PBS and incubated for 2 h at RT. Bound DPEAAE-containing versican fragments were detected using mouse anti-G1 monoclonal antibody (3 µg/mL in 0.5% BSA/PBS, 1.5 h at RT) followed by horseradish peroxidase (HRP)-conjugated anti-mouse antibodies (2.4 µg/mL in 0.5% BSA/PBS, 1 h at RT). Each step was followed by three washes with PBS containing 0.1% Tween-20. Finally, signal was developed by addition of o-phenylenediamine dihydrochloride (OPD) for 10 minutes and reactions were stopped with 2 M H_2SO_4. The absorbance was read at 492 nm.

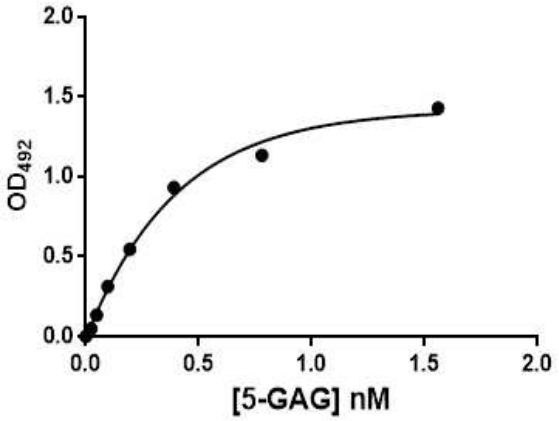

Figure 2. **Calibration curve for quantification of versican cleavage.** Standard concentrations (0-1.56 nM) of completely digested V1-5GAG underwent ELISA assay previously described, obtained an absorbance value at 492 nm for each tested concentration. Reported values of absorbance have been subtracted of the blank signal (undigested V1- 5GAG). Curve was fitted through nonlinear regression and used for extrapolating unknown concentrations of versikine in the samples.

Quenched- Fluorescent (QF) peptide cleavage assay

QF peptides are small synthetic peptides, composed of ~12 amino acids, whose functionality is based on Förster Resonance Energy Transfer (FRET) technology. These peptides are designed with a fluorophore at one end and a quencher at the other. In the intact peptide, the proximity of the quencher to the fluorophore prevents the emission of fluorescent signal. However, if the peptide contains a proteolytic cleavage site and is cleaved by a protease, the fluorophore is separated from the quencher, resulting in the emission of fluorescence.

QF peptides were synthesized by Fowkes *et al*. and details are reported in **Table 1** [210]. Cleavage assay was conducted in 384-well plates (Greiner Bio-One, Cat. No.: 784900) using a SpectraMax i3 Multi-Mode Platform (Molecular Devices), as described by Santamaria *et al*. [211]. The reactions were carried out at a final volume of 20 µl, incubating 40 µM of each QF peptide with 10 nM ADAMTS9 MDTCS in TNC-B buffer at 37 °C for 24 hours. Fluorescence intensity was measured with an excitation wavelength of 300 nm and an emission wavelength of 430 nm. Blank values (from reactions without enzyme) were subtracted from the corresponding experimental fluorescence values, and the results are reported as changes in relative fluorescence units (ΔRFU). As a positive control, digestion of ADAMTS5 against its specific QF peptide #6 was simultaneously performed.

Data

analysis and statistical tests

Catalytic efficiency (k_{cat}/K_m) were calculated using a nonlinear regression analysis, by means of the equation:

$$y = 1 - e^{-(0.1\,x \cdot \frac{kcat}{Km})}.$$

Band intensity was quantified through ImageJ software tool, and compared using One Way ANOVA statistical test, performed with GraphPad Prism 9 software.

# QF peptide	Peptide Sequence
1	Abz-TESESRGAIY-Dpa-KK-NH2
2	KY(NO$_2$)TESESRGK(Abz)IYYKKG
3	KY(NO$_2$)SEGESRGK(Abz)JYFKKG
4	KY(NO$_2$)TEGESRGK(Abz)JZYKKG
5	KY(NO$_2$)SENESRGK(Abz)IYYKKG
6	WYRGRL-AEEA-KY(NO$_2$)TESESRGK(Abz)IYYKKG
7	WYRGRL-AEEA-KY(NO$_2$)NDTESOAK(Abz)AHFUKG
8	KY(NO$_2$)TENESRGK(Abz)IYYKKG
9	KY(NO$_2$)QDSESBAK(Abz)JHYUKG
10	KY(NO$_2$)TETESOAK(Abz)IYFKKG
11	KY(NO$_2$)SESESRGK(Abz)IYYKKG
12	KY(NO$_2$)NDTESOAK(Abz)AHFUKG
13	KY(NO$_2$)NESESKAK(Abz)VHYKKG

Table 1. **Peptide sequences of QF substrates**. This table summarizes the FRET peptides assessed for ADAMTS9 MTDCS cleavage. For each peptide, numbered from 1 to 13, the amino acid sequence is reported. Of note, the ortho-amino benzoyl group (Abz, bound to the side chain of lysine) acts as the fluorophore, while the quenchers are either the N-3-[2,4-dinitrophenyl]-L-2,3 diaminopropionyl group (Dpa) or the 3-nitro-L-tyrosine (Y(NO2)). Non-traditional amino acids are indicated as follows: O = ornithine, B = 2,4-Diaminobutyric acid, J = β-cyclopropyl-alanine, Z = 4-Thiazolyl-alanine, U = 2,3-Diaminopropionic acid, AEEA = 8-amino-3,6-dioxaoctanoic acid.

Results and Discussion

ADAMTS9 MDTCS does not cleave ADAMTS FRET substrates

A screening of available QF peptides was performed to identify an optimal ADAMTS9 substrate. A total of 13 different FRET substrates were tested for ADAMTS9 MDTCS cleavage after 24 h of incubation. Fluorescence for each tested substrate, corrected by subtracting the respective blank value, is shown in **Figure 3**. Among all the QF peptides screened, only substrate #6 generated a signal appreciably different from the background, with a ΔRFU > 220,000. However, when compared to the signal generated by ADFAMTS5 cleavage of QF peptide #6, it is evident that ADAMTS9 MDTCS does not exhibit significant cleavage activity toward any of the tested peptides. Ultimately, I did not identify any QF peptide from the tested substrates suitable for the quantitative characterization of ADAMTS9 MDTCS. As this small library was originally

designed for ADAMTS5 [15], these results suggest that the cleavage site specificity of ADAMTS9 is distinct from that of ADAMTS5.

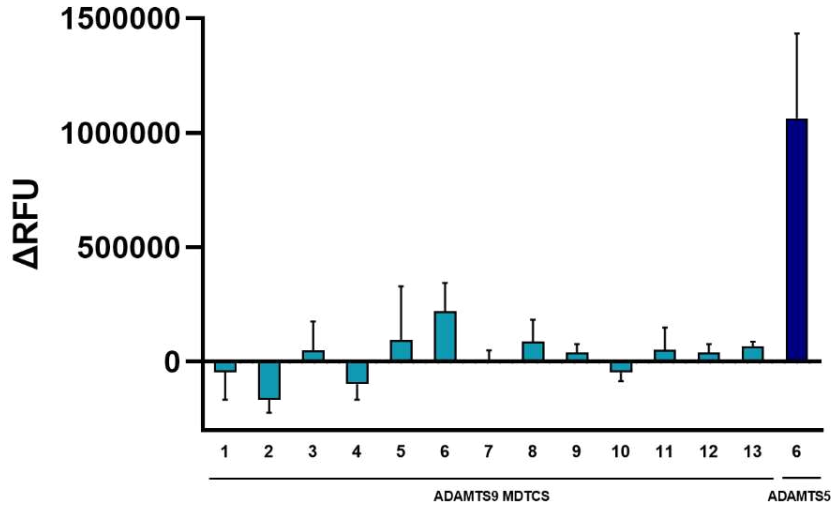

***Figure 3*. Cleavage Activity of ADAMTS9 MTDCS on QF Peptides.** The graph displays florescence values subtracted of the blank (ΔRFU) for the tested QF peptides. As a positive control for high cleavage activity, the signal from ADAMTS5 incubated with its optimal QF substrate #6 is shown (dark blue bar). Each assay was performed at least three times, with results reported as the average ± SD.

ADAMTS9 MDTCS aggrecanase activity is lower than that of ADAMTS5.

As ADAMTS9 phylogenetically belong to the proteoglycanase subfamily of ADAMTSs, I initially assessed the proteolytic activity of ADAMTS9 MDTCS against aggrecan, one of the most abundant CS proteoglycans and a major component of cartilage and cardiovascular tissue [212] [213], in comparison to the well-established aggrecanase ADAMTS5 (also known as aggrecanase-2). The presence of fragments of varying molecular weights, resulting from the proteolytic cleavage by ADAMTS5 and ADAMTS9 MDTCS at different cleavage sites, can be detected through immunoblotting using specific antibodies. First, I analysed the products of 2-hour digestion reactions via immunoblotting with the 2B6 antibody, which recognizes the CS stubs generated by chondroitinase ABC following deglycosylation. Aggrecan was present as a major band with molecular weight >250 kDa, while a band of approximately 40 kDa was detected in all samples analysed, including undigested aggrecan, suggesting the occurrence of proteolysis in the commercial aggrecan batch (Figure 4-A). However, the intensity of this

band increased in the presence of ADAMTS5 and all tested concentrations of ADAMTS9 MDTCS (100-0.1 nM). Notably, digestion of aggrecan with ADAMTS5 resulted in the appearance of numerous low molecular weight bands (**Figure 4-A**).

These results suggest that ADAMTS9 MDTCS possesses aggrecanase activity, albeit to a lesser extent compared to ADAMTS5. I then evaluated the presence of the neoepitope ARGSV, generated by cleavage at the site located at Glu^{392}-Ala^{393} (UniProt ID: P13608-1) (**Figure 4-B**). The blotting revealed faint immunoreactive bands of approximately 250 kDa, corresponding to the C-terminal fragment containing the neoepitope, in both ADAMTS5 and ADAMTS9 MDTCS digests. This fragment should be generated by an additional cleavage at Glu^{1499}-Gly^{1500} [214].

However, in the ADAMTS5 digest, there were additional immunoreactive bands at lower molecular weights, suggesting multiple proteolytic cleavages by ADAMTS5 that generated smaller fragments, all containing the neoepitope ARGSV. ADAMTS9 MDTCS was also capable of generating lower molecular weight cleavage products, but only at the highest concentration tested (500 nM). Overall, these results confirm that ADAMTS9 MDTCS exhibits proteolytic capacity toward aggrecan, although this is greatly reduced compared to ADAMTS5.

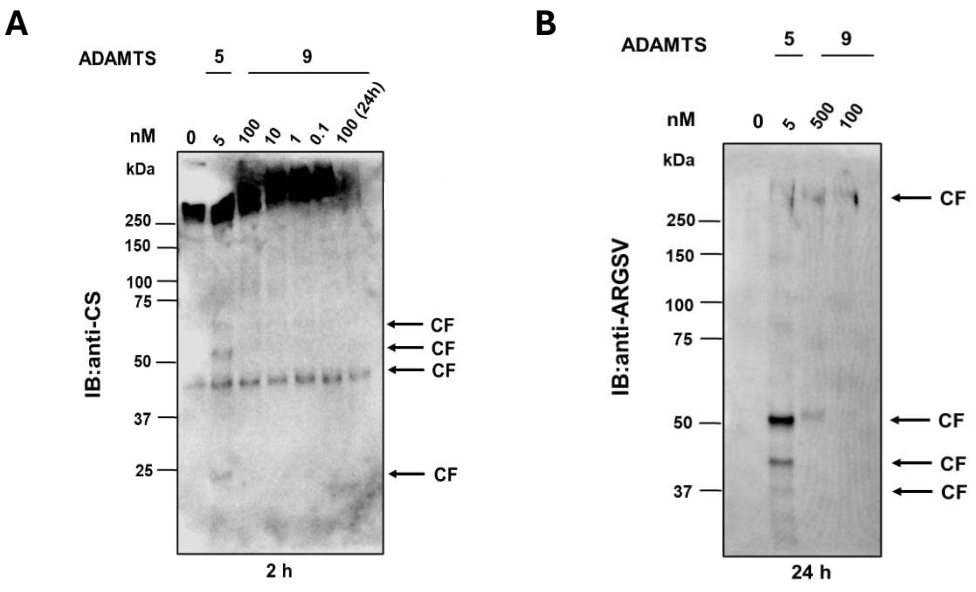

***Figure 4*. Aggrecanase activity of ADAMTS9 MDTCS**. Increasing concentrations of ADAMTS9 MDTCS (0.1-500 nM) or 5 nM ADAMTS5 (as positive control of cleavage) were incubated with aggrecan (667 nM). Digestions were stopped after 2 or 24 h, as indicated, and cleavage fragments deglycosylated and subjected to SDS-PAGE. Bands were detected using the antibody 2B6, against the CS stubs left following treatment of aggrecan with chondroitinase ABC (**A**), or a neoepitope antibody recognizing the aggrecan ARGSV neoepitope (**B**). CF, cleavage fragment. "0" condition refers to buffer control.

This result is consistent with previous findings by Rogerson *et al*., who demonstrated that the aggrecanase activity of ADAMTS9 could only emerge, *in vivo,* in the absence of the two major aggrecanases, ADAMTS5 and ADAMTS4, whose strong activity against this substrate otherwise prevailed over that of ADAMTS9[215]. The lower aggrecanase activity of ADAMTS9 MDTCS, exerted in a controlled and less destructive manner compared to the other two enzymes, suggests that the role of this enzyme may be related to fine matrix remodelling during development and tissue homeostasis in adults.

ADAMTS9 MDTCS shows robust proteolytic activity against versican

Since ADAMTS9 was reported to cleave versican in a cell-based ADAMTS assay [202], ADAMTS9 MDTCS versicanase activity was assessed against purified Versican V1 isoform, using both the full-length versican (V1-FL) and its truncated variant V1-5GAG. Digestion products were compared to those of ADAMTS5, the most potent versicanase [207].

Increasing concentrations of ADAMTS9 MDTCS (0.1–100 nM) were incubated with 100 nM of each substrate for 2 hours, and the cleavage products were analysed by immunoblotting using anti-VC and anti-DPEAAE antibodies detecting versican/versikine and versikine alone, respectively. As shown by the immunoreactive bands for VC (**Figure 5**-**A** and -**B**), the intensity of the uncleaved substrate (indicated as FL) decreased with higher concentrations of ADAMTS9 MDTCS. Conversely, the lower molecular weight band corresponding to the cleavage product versikine was absent or faint at the lowest ADAMTS9 MDTCS concentrations and increased in intensity as the enzyme concentration rose. Furthermore, after a 24 hour incubation, the versican FL form was no longer detectable, with only versikine remaining, similar to what was observed for ADAMTS5, indicating complete substrate digestion. This result was corroborated using the anti-DPEAAE neoepitope antibody, which detects specifically versikine (**Figure 5-C** and -**D**).

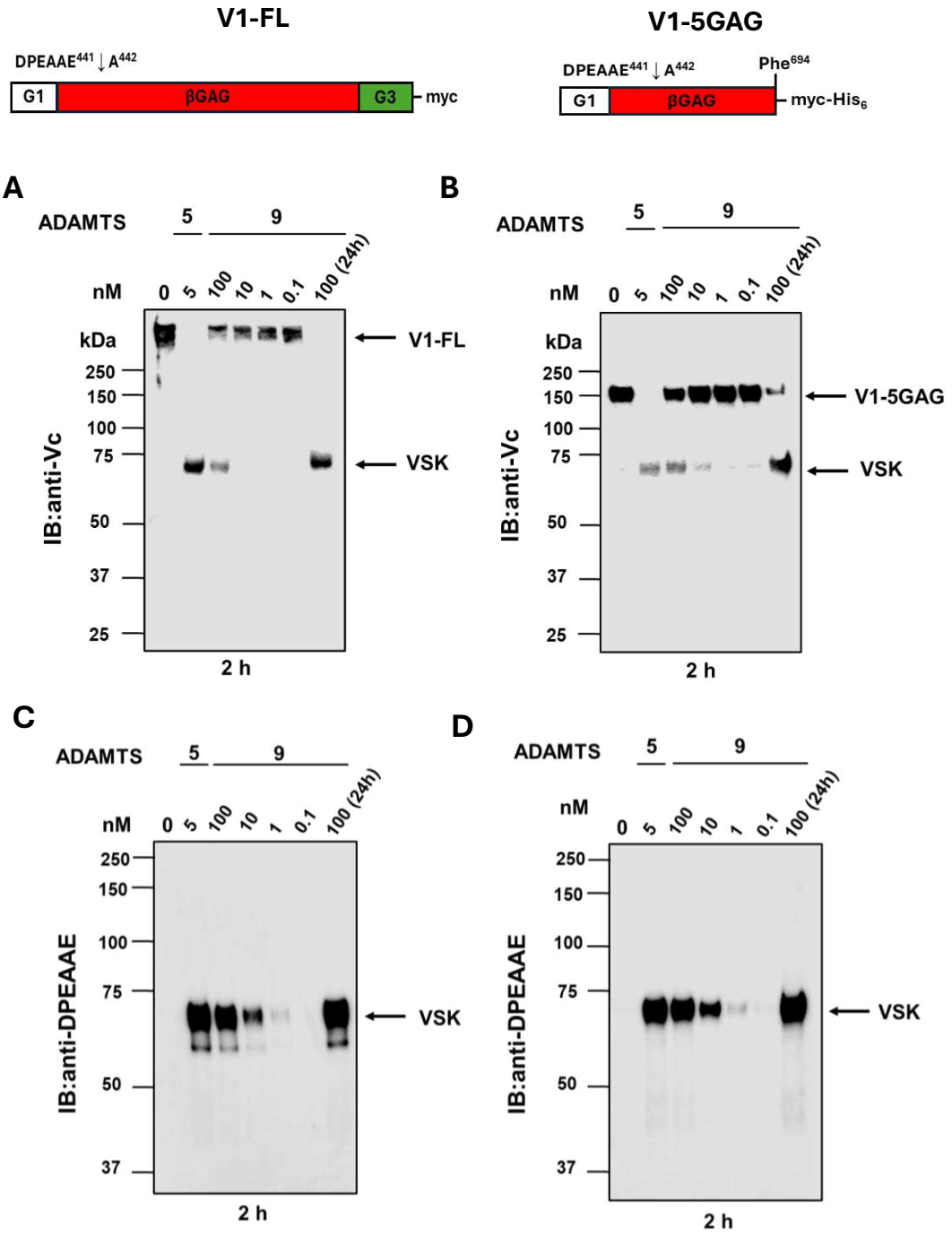

Figure 5. **Versicanase activity of ADAMTS9 MDTCS.** Increasing concentrations of ADAMTS9 MDTCS (0.1-100 nM) or 5 nM ADAMTS5 (as positive control) were incubated with 100 nM versican variants V1-FL (**A** and **C**) or V1-5GAG (**B** and **D**). Digestions were stopped after 2 or 24 h with EDTA and cleavage fragments deglycosylated and subjected to SDS-PAGE. Bands were detected using the anti VC antibody, recognizing the versican sequence ^{432}VPKDPEAAEARRG^{445} containing the Glu^{441}-Ala^{442} cleavage site (**A** and **B**) or the anti-DPEAAE neoepitope antibody for versikine (VSK) detection (**C** and **D**).

The versicanase activity of ADAMTS9 MDTCS (50 nM) was also quantitatively assessed using an in-house sandwich ELISA after incubation with either 50 nM V1-FL or V1-5GAG (**Figure 6**). At the indicated time points, aliquots were taken, the reactions were stopped with EDTA, and the concentration of cleavage products was quantified by ELISA, as previously described[207], [216]. Fractional cleavage was plotted over time, and non-linear regression analysis was performed to obtain kinetic parameters, revealing that ADAMTS9 MDTCS cleaved full-length versican with a specificity constant (k_{cat}/K_m) of 6×10^3 $M^{-1}s^{-1}$. This value was approximately 600-fold lower than ADAMTS5, 35-fold lower than ADAMTS4, but 2-fold higher than ADAMTS1 (**Table 2**). Of note, the two tested substrates were cleaved at the same rate, in agreement with previous findings for ADAMTS1, 4, and 5 [207], [217]. In conclusion, ADAMTS9 MDTCS efficiently cleaved both V1-FL and V1-5GAG variants, although with lower efficiency compared to ADAMTS5, which remains the most potent versicanase at the Glu^{441}-Ala^{442} site.

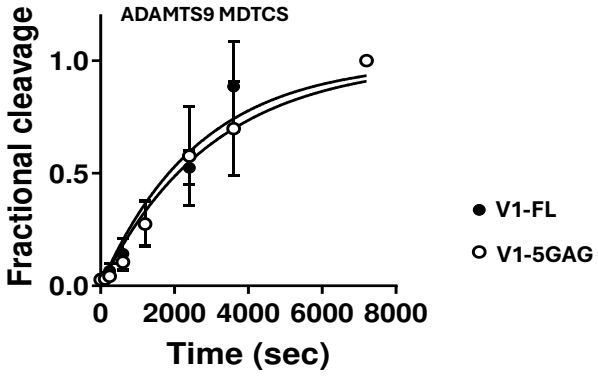

Substrate	k_{cat}/K_m ($\times10^3$ M^{-1} s^{-1})
V1	6.10 ± 2.7
V1-5GAG	6.00 ± 3.0

***Figure 6*. Quantitative determination of versicanase activity of ADAMTS9 MDTCS**. ADAMTS9 MDTCS was incubated with either 50 nM V1-FL (black dots) or V1-5GAG (white dots), and versikine quantified by sandwich ELISA at different time points. Fractional cleavage was plotted against time and nonlinear regression analysis was performed to obtain kinetic parameters summarized in table. Data are reported as mean ± SD.

ADAMTS family member	kcat/Km (x10^5 $M^{-1}sec^{-1}$) (V1-5GAG)	Reference
ADAMTS 5 FL	35.6 ± 3.8	[207]
ADAMTS 4 FL	2.10 ± 0.28	[207]
ADAMTS 9 MDTCS	**0.06 ± 0.03**	
ADAMTS 1 FL	0.042 ± 0.023	[217]
ADAMTS 8 FL	ND	[208]

***Table 2*. Kinetic parameters for proteolysis of V1-5GAG by different ADAMTS proteoglycanases.** The values were obtained using a sandwich ELISA assay using the wild type, full-length enzymes, except for ADAMTS9, whose wild-type form has not yet been purified. ADAMTS4 and ADAMTS5 were found to be the enzymes with the highest versicanase activity, followed by ADAMTS9 MDTCS and ADAMTS1, while no cleavage activity against versican was detected for recombinant ADAMTS8. FL, full-length, ND, not detected.

ADAMTS9 MDTCS cleaves biglycan

To complete the characterisation of the proteoglycanase activity of ADAMTS9 MDTCS towards major CS proteoglycans, I tested its proteolytic activity against biglycan. Biglycan is a small leucine-rich proteoglycan (SLRP) of 42 kDa (in its deglycosylated form), a ubiquitous non-fibrillar component of the extracellular matrix (ECM), which functions both as a structural scaffold and as an inflammatory signalling molecule, when proteolytically released from ECM [197]. I conducted 24 h digestion reactions with 500 nM ADAMTS9 MDTCS and 2 μM biglycan. The digestion products were then deglycosylated and analysed through Coomassie Brilliant Blue (CBB) staining and Western blotting. The results are shown in **Figure 7**. Notably, both ADAMTS5 and ADAMTS9 MDTCS (albeit weakly) demonstrated the ability to cleave biglycan, producing low molecular weight fragments. While the biglycanase activity of ADAMTS5 has been well documented [208] [217], the ability of ADAMTS9 to cleave biglycan had not been previously observed. This finding provides new insights into the activity of ADAMTS9 and its physiological substrates.

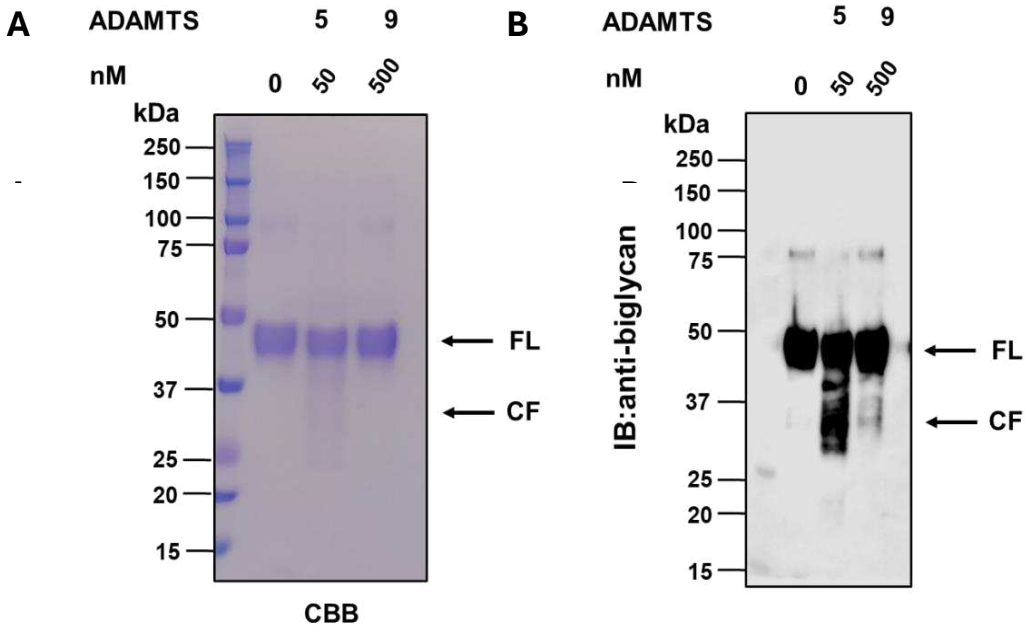

***Figure 7.* ADAMTS9 MDTCS proteolytic activity against biglycan.** Activity of ADAMTS9 MDTCS (500 nM) and ADAMTS5 (50 nM) against biglycan (2 μM) was investigated after 24 h digestion. After deglycosylation, samples were analysed by CBB (**A)** and western blotting **(B)**, using polyclonal anti-biglycan antibodies. CF, cleavage fragments: FL, full-length.

TIMP-2 and TIMP-3 are inhibitors of ADAMTS9 versicanase activity

The four Tissue Inhibitors of Metalloproteinases (TIMPs) are endogenous ADAMTS inhibitors whose conserved Cys^1 coordinates the catalytic Zn^{2+}, which is essential for ADAMTS catalytic activity, through bidentate interactions with its α-amino and carbonyl groups. This binding occurs in a 1:1 stoichiometric ratio [218]. To test their inhibitory properties, I incubated ADAMTS9 MDTCS (100 nM) with different TIMPs (each at 500 nM) for 1 h before addition of V1-5GAG (100 nM) and incubation at 37° C for 2 h. Reactions with ADAMTS5 in the absence of inhibitors were performed as a positive control. After deglycosylation, cleavage products were analysed by SDS-PAGE and immunoblotting using the anti-DPEAAE antibody. Our results showed that TIMP3 completely inhibited versikine generation, as evidenced by the absence of a band, while TIMP2 only partially inhibited it under these conditions, as indicated by a fainter band (**Figure 8**).

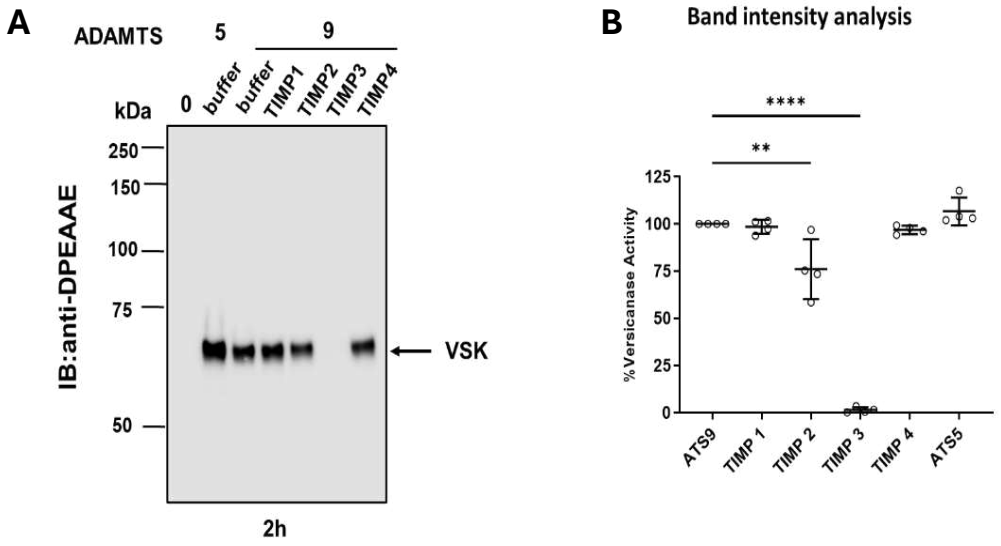

Figure 8. **Inhibition of ADAMTS9 MDTCS by TIMPS 1-4.** **A** 500 nM TIMP-1, -2, -3, and -4 were preincubated with ADAMTS9 MDTCS (100 nM) or ADAMTS5 (5 nM) for 1 h at 37° C before the addition of 100 nM versican V1-5GAG. After 2 h, samples were deglycosylated, subjected to SDS-PAGE and immunoblotted for versikine (VSK) detection using anti-DPEAAE antibody. **B** Band intensities were quantified using ImageJ and statistically analysed by GraphPad Prism Software. Results were reported as the mean of residual activities compared to ADAMTS9 versicanase activity in the absence of inhibitors (indicated as 'buffer') ± SD (n = 4 independent experiments). ** $p < 0.01$; **** $p \leq 0.0001$ (One Way ANOVA).

I thus confirmed TIMP3 as the most effective inhibitor of ADAMTS9 MDTCS versicanase activity, followed by TIMP2, consistent with what is already known for ADAMTS5 and ADAMTS4 [219], [220], while TIMP1 and TIMP4 did not show significant inhibition. Notably, ADAMTS ancillary domains are generally not required for TIMP inhibition [221], thus these results may likely be extended to ADAMTS9 FL. The identification of a potent inhibitor of ADAMTS9 with such inhibitory properties will enable the precise determination of active ADAMTS9 MDTCS concentrations. To this end, continuing the screening initiated with the QF peptides in search of potential small substrates of ADAMTS9 that allow for quantitative measurement will be essential to carry out active site titration.

Conclusions and Perspectives

The difficulty in obtaining purified full-length recombinant ADAMTS9 protein, likely due to proteolytic susceptibility, has delayed its enzymatic characterisation. Further attempts will be necessary to optimize the expression and purification of the full-length protein, as well as various deletion variants, to explore potential differences in proteolytic activity towards identified substrates and to identify specific domains critical for interactions with different substrates and/or inhibitors. For the first time, Santamaria and collaborators successfully expressed and purified a truncated form of ADAMTS9, encompassing the core proteoglycanase domain (i.e., truncated after the Spacer domain), referred to as ADAMTS9 MDTCS. I demonstrated that ADAMTS9 MDTCS cleaves the proteoglycans aggrecan, versican, and biglycan, and its versicanase activity was primarily inhibited by TIMP3.

These findings indicate that the proteoglycanase activity of ADAMTS9 is similar, albeit weaker, to that of ADAMTS4 and ADAMTS5, both in terms of substrate specificity and natural interactors. This suggests that its specific role in heart development may be a result of spatiotemporal regulation as it is known that ADAMTS4 and ADAMTS5 knockout mice are viable and do not have major phenotypic anomalies [222].

APPENDIX II: Expression and purification of recombinant Syndecan-4 ectodomain

Introduction

Syndecans are type I transmembrane heparan sulfate (HS) proteoglycans that play a critical role in numerous physiological (such as wound healing and development) and pathological processes (including tumour progression and metastasis), by regulating cellular proliferation, differentiation, adhesion, and migration [223]. In mammals, the syndecan family comprises four members - syndecan-1 through syndecan-4 - illustrated in **Figure 1.** Syndecan-1 is predominantly expressed in epithelial tissues, syndecan-2 in endothelial cells and fibroblasts, and syndecan-3 primarily in neuronal and musculoskeletal tissues [224]. In contrast, syndecan-4 is ubiquitously expressed.

Similar to other syndecans, syndecan-4 contains an ectodomain to which linear chains of glycosaminoglycans are covalently attached, facilitating extracellular interactions. Specifically, the syndecan-4 ectodomain is modified with three HS chains N-terminally located. The transmembrane region of syndecan-4 is a single-pass domain that is highly conserved among all syndecan family members, while the intracellular domain contains a variable region that determines the cytoplasmic interactors specificity, thus activating specific signalling pathway. This variable region is flanked by two conserved domains, C1 and C2, which are shared across all syndecans [225].

As a proteoglycan with extracellular HS chains, syndecan-4 interacts with a wide array of heparin-binding growth factors, including fibroblast growth factors (FGFs), vascular endothelial growth factors (VEGFs), and platelet-derived growth factors (PDGFs) [226], [227] [228]. The binding of these growth factors can initiate cellular signalling by presenting the growth factor ligand to its signalling receptor or modulating growth factor bioavailability by serving as a cell-bound reservoir [229]. In this manner, syndecan-4, along with other heparan sulfate proteoglycans, helps establish spatial gradients of growth factors as well as of other extracellular matrix (ECM) components, such as proteases and protease inhibitors [230]. Additionally, syndecan-4 also functions, in a Rho-dependent manner, with the $\alpha_5\beta_1$ integrin to

promote the adhesion-dependent formation of actin stress fibers and focal adhesions, which are stable contact points between the cell and the extracellular matrix (ECM) [231], [232].

Interestingly, syndecan ectodomains can be released into the extracellular environment through highly regulated proteolysis called shedding [223], [233], [234]. This cleavage occurs constitutively but is accelerated under specific conditions, such as inflammation [226], [227] and wound healing [235], [236]. The shedding of syndecan ectodomains not only downregulates signalling but can also convert membrane-bound receptors into soluble effectors or antagonists. Soluble syndecan ectodomains can compete with intact syndecans for extracellular ligands in the pericellular space [237], while the remaining portion of the membrane-bound receptor loses its ability to bind ligands and may undergo further processing by the presenilin/γ-secretase complex [238].

Various sheddases, including matrix metalloproteinases (MMPs), ADAM (a disintegrin and metalloproteinase) proteins, and ADAMTS (ADAM with thrombospondin motifs) proteins, have been shown to cleave syndecans on their extracellular side, releasing soluble syndecan ectodomains [239], [240].

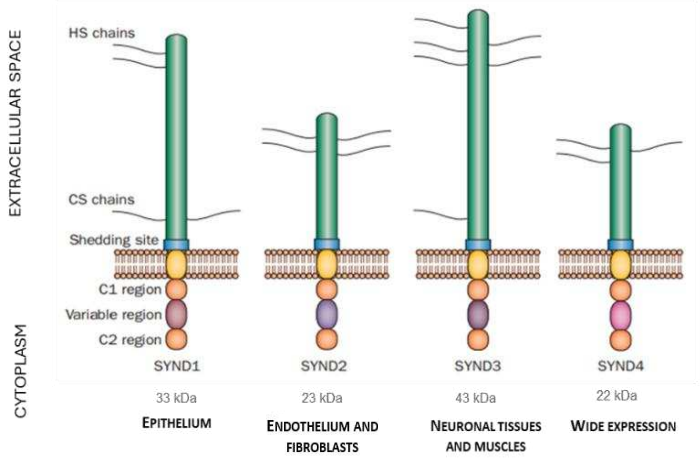

***Figure 1*. Human members of syndecan family.** While the organization and size of the intracellular domains are highly similar among the four syndecans, the ectodomains of syndecan-1 and syndecan-3 are larger than those of syndecan-2 and syndecan-4, allowing them to carry both N-terminal heparan sulfate (HS) and juxtamembrane chondroitin sulfate (CS) chains. The cytoplasmic domains contain two highly conserved regions, C1 and C2, separated by a syndecan-specific variable (V) region. The major sheddase cleavage site, indicated by the blue square, is located adjacent to the cell membrane. Figure adapted from Pap and Bertrand, 2013 [234].

Recent findings have shown that the ectodomain of syndecan-4 regulates the activation of ADAMTS-5 through direct interaction [241]. Similarly, Gao et al. suggested that syndecan-1 enhances the aggrecanase activity of ADAMTS-4 by forming a complex at the cell surface [242].

In a screening for ADAMTS substrates and interaction partners, the Santamaria lab tested a fragment of the syndecan-4 ectodomain (residues 19-145, commercially available from Bio-Techne Ltd, product code 2918-SD-050) for its ability to affect the proteolytic activity of ADAMTS-4 and ADAMTS-5. The syndecan-4 fragment was dialyzed into assay buffer (20 mM Tris, 150 mM NaCl, 10 mM $CaCl_2$) to remove preservatives that could interfere with the assay. Surprisingly, shed syndecan-4 exhibited inhibitory activity against both proteases, with IC_{50} values of 20 nM and 140 nM for ADAMTS-4 and ADAMTS-5, respectively.

To confirm the inhibitory effect of the syndecan-4 ectodomain on these proteoglycanases and rule out potential contaminants in the commercial batch, a purified, recombinant syndecan-4 ectodomain (SDC4-ect) was required. In this study, we expressed recombinant human syndecan-4 ectodomain, using various combinations of protease inhibitors, given the susceptibility of syndecan-4 to proteolytic cleavage. Syndecan-4 ectodomain was successfully expressed; however, due to its inherent instability, it was not possible to obtain a purified protein for further studies. Additional optimization will be necessary to maintain the integrity of the syndecan-4 ectodomain throughout the purification process.

Materials

For bacterial growth, 20 g Luria Bertani (LB) broth (with or without agar) were dissolved in 1 L of water, then sterilized by autoclaving.

The synthetic, hydroxamate-based metalloproteinase inhibitor CT1746 (a kind gift from Dr. Yoshifumi Itoh, University of Oxford) was dissolved in DMSO at a stock concentration of 10 mM and stored at -80°C.

For Ni-Sepharose chromatography, the following buffers were prepared: column-preparing buffer: 0.1 M $NiSO_4$; Equilibration buffer: 20 mM HEPES pH 7.4 + 150 mM NaCl; Washing buffer:

20 mM HEPES pH 7.4 + 150 mM NaCl + 10 mM imidazole; Elution buffer: 20 mM HEPES pH 7.4 + 150 mM NaCl + 300 mM imidazole; Regeneration buffer #1: 20 mM HEPES pH 7.4 + 150 mM NaCl + 100 mM EDTA; Regeneration buffer #2: 20 mM HEPES pH 7.4 + 150 mM NaCl + 50 mM EDTA + 8 M urea.

For HiTrap Q Sepharose Fast Flow (Q FF) anion exchange chromatography, the following buffers were utilised: Buffer A: 20 mM HEPES pH 7.4 + 0.2 M NaCl; Buffer B: 20 mM HEPES pH 7.4 + 0.7 M NaCl; Regeneration buffer: 20 mM HEPES pH 7.4 + 2 M NaCl.

Methods

Syndecan-4 ectodomain construct amplification and purification

A cDNA construct encoding the human syndecan-4 ectodomain (amino acids 1-145), with a C-terminal tandem 6-His tag (shown in **Figure 2-A**), was custom-synthesized by Invitrogen. 100 ng of the construct were used to transform 25 µL of TOP10 competent *E. coli* cells (Invitrogen). Briefly, the DNA was added to the bacterial cell suspension, kept on ice for 30 min, then heat-shocked for 30 sec at 40°C in a water bath, and finally returned to ice for 2 min. Next, 250 µL of SOC Outgrowth Medium (New England Biolab) was added to the cell suspension, which was then incubated with gentle agitation at 37°C for 50 min. Subsequently, 100 µL of the cell suspension was plated on a 100 mm Petri dish containing LB agar with 100 µg/mL ampicillin and incubated overnight (ON) at 37°C. The following day, a single colony was picked and inoculated into 5 mL of LB broth with 100 µg/mL ampicillin, followed by ~8 h of shaking incubation at 37°C. Then, 1 mL of this cell culture was added to 300 mL of LB broth with 100 µg/mL ampicillin and incubated overnight at 37°C with vigorous shaking. The amplified plasmid was then purified using the ZymoPURE II Plasmid Maxiprep Kit (ZymoResearch), following the manufacturer's instructions. Finally, the plasmid DNA concentration and purity were measured using the QFX Fluorometer (DeNovix), and the sample was stored at -20°C.

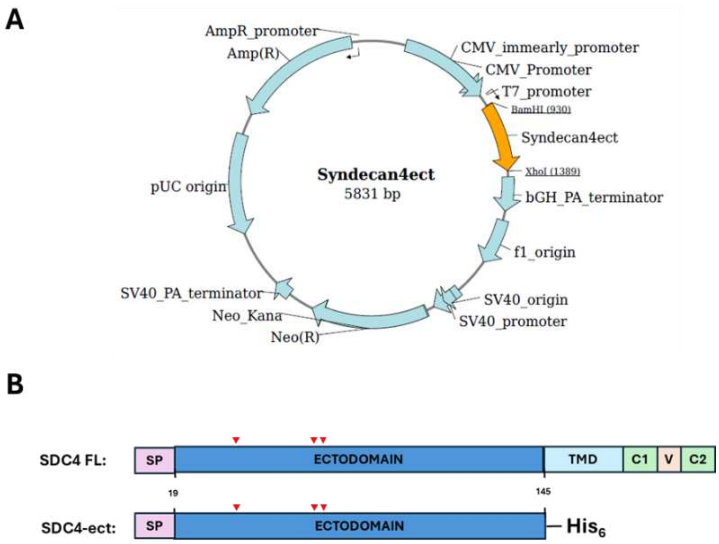

Figure 2. **The SDC4-ect construct. A** The illustrated construct, 5831 bp in length, was used for the expression of recombinant SDC4-ect protein in HEK293T cells. The syndecan-4 ectodomain sequence was cloned into the plasmid using the BamHI (position 930) and XhoI (position 1289) restriction sites. Transgene expression is regulated by the human cytomegalovirus (CMV) immediate-early enhancer and promoter, along with the bovine growth hormone polyadenylation (bGH-PA) signal, which serves as the transcription terminator. The plasmid also contains an ampicillin resistance gene for the selection of transformed cells during construct amplification. **B** Comparison of full length Syndecan-4 (SDC4 FL) and SDC4-ect construct. As shown, the construct was designed to express the extracellular portion of syndecan-4, lacking the signal peptide (SP), transmembrane domain (TMD), and the cytoplasmic portion, which includes the two conserved domains C1 and C2 as well as the variable region (V). A C-terminal 6xHis tag (His6) was added to the recombinant protein to facilitate detection and purification. Sites of O-glycosylation (located at serine residues 39, 61and 63, [253]) are indicated by red arrowheads and are retained in the recombinant SDC4 ectodomain construct.

Cell culture and Transient transfection

Human embryonic kidney cells (HEK293T, ATCC: CRL-3216) were cultured in Eagle's Modified Minimum Essential Medium (MEM) supplemented with 10% (v/v) fetal bovine serum (FBS), 50 mU/mL penicillin-streptomycin, 2 mM glutamine, and 1% (v/v) non-essential amino acids (NEAA), maintained at 37°C in a humidified atmosphere containing 5% CO_2. Cells were grown in the supplemented medium, which was refreshed every other day until they reached 80% confluence, then sub-cultured using Trypsin/EDTA solution.

For transient transfection, cells were seeded either in 6-well plates (for small-scale transfections) or in 525 cm^2 triple flasks (vWR product code 734-2001) in growth medium. Upon reaching confluence, cells were transfected as follows: the transfection solution was first prepared, adding 4 µg/well or 107 µg/triple flask of SDC4-ect construct and a volume of

polyethylenimine (PEI) equivalent to 3.6 times the amount of the construct (PEI stock solution: 1 mg/mL) to a 0.15 M NaCl solution, and incubating at room temperature (RT) for 10 min. Next, the transfection solution was added to OptiMEM medium supplemented with 50 mU/mL penicillin-streptomycin and 2 mM $CaCl_2$ (expression medium). Cells were washed once with sterile PBS before the addition of expression medium. When specified, 100 µM CT1746 (final concentration) and/or a protease inhibitor cocktail (PIC, Clinisciences catalogue number K1008-1ml) were added to the cells, which were subsequently incubated at 37°C for 24, 48, or 72 h, as indicated. Whenever indicated, 4 h after transfection, a 0.2 mg/mL heparin solution was added to conditions specified as "+heparin."

Medium harvest and expression analysis

At the specified time points, both the conditioned medium (CM) and cell lysates from small-scale transfected cells were collected to test SDC4-ect expression. Briefly, 1 mL of CM was collected, followed by protein precipitation with 50 µL of 100% trichloroacetic acid (TCA), and incubated overnight (ON) at 4°C. The following day, the sample was centrifuged at 14,000 × *g* for 30 min at 4°C, the supernatant was discarded, and the protein pellet was resuspended in 25 µL of reducing sample buffer (containing 5% β-mercaptoethanol), then heated for 10 min at 90°C for subsequent western blot analysis. In parallel, cells were washed once with PBS, then lysed by adding 200 µL of cell lysis buffer (Merck) and incubation at 37°C for 15 min. Subsequently, 100 µL of reducing sample buffer was added, and the lysate was collected in an Eppendorf tube and heated for 10 min at 90°C.

For western blot analysis, both the CM and cell lysates were loaded onto a NuPAGE 4–12% Bis-Tris gel, electrophoresed at 200 V for 40 min, and transferred onto nitrocellulose membranes using the Trans-Blot® Turbo Transfer System (BioRad). The membranes were then probed with a rabbit anti-HisTag antibody (1:40,000 in 0.5% BSA/PBS), recognizing the C-terminal 6-His tag, and a rabbit anti-actin antibody (1:10,000 in 0.5% BSA/PBS).

SDC4-ect purification

400 mL of CM from large-scale transfection were collected after 48 h of incubation and concentrated approximately 10-fold using the Labscale Tangential Flow Filtration (TFF) system (Merck). The concentrated CM was then purified by Fast Protein Liquid Chromatography (FPLC) on an ÄKTAstart™ preparative chromatography system (Cytiva). Two sequential purification passages were performed, and elution profiles were monitored by absorbance at 280 nm. After each purification step, the presence of recombinant SDC4-ect was confirmed via western blotting (WB) using an anti-HisTag antibody, and purity was assessed by Coomassie Brilliant Blue (CBB) staining.

First, Ni-Sepharose chromatography was performed using a HiTrap Chelating HP column (0.7 x 2.5 cm, Cytiva) pre-charged with Ni^{2+} ions by passing 5 column volumes (CV) of column preparation buffer. The entire procedure was conducted at a flow rate of 0.5 mL/min, with fractions of 2.5 mL collected. Before loading the concentrated CM, the column was equilibrated with 5 CV of equilibration buffer. Following sample loading, the column was washed with 3 additional CV of equilibration buffer, followed by 3 CV of elution buffer #1. Proteins were eluted by passing 10 CV of a linear gradient of 10–300 mM imidazole (starting from elution buffer #1 and elution buffer #2). Finally, the column was regenerated by passing 5 CV of regeneration buffer #1, followed by 5 CV of regeneration buffer #2. An aliquot from each fraction was taken for SDC4-ect expression and purity analysis. Positive fractions were pooled and stored at -80°C for use in the subsequent purification step.

Next, an anion exchange chromatography was performed using a HiTrap Q FF column (0.7 x 2.5 cm, Cytiva). The column was initially equilibrated with 10 CV of buffer A at a flow rate of 1 mL/min. The pooled fractions from the previous purification step were diluted 2.5-fold in buffer A, and loaded onto the column at a flow rate of 0.5 mL/min. After sample loading, the column was washed with 6 CV of buffer A, and protein elution was achieved using 10 CV of a linear gradient (0–100%) of buffer B at a flow rate of 1 mL/min. Fractions of 1 mL were collected, with an aliquot from each fraction analysed for purity. Finally, the column was regenerated by passing at least 5 CV of regeneration buffer at a flow rate of 1 mL/min. An aliquot from each fraction was retained for SDC4-ect expression and purity evaluation.

SDC4-ect is expressed in its intact form in the presence of the hydroxamate inhibitor CT1746

In pilot experiment, HEK293T cells were transfected with the plasmid containing the SDC4-ect construct, and expression in both the CM and cell lysates (Lys) was evaluated after 72 h of incubation. Additionally, to facilitate potential release of the secreted protein from the ECM, heparin was added 4 hours after the transfection solution. As shown in **Figure 3,** no immunoreactive band corresponding to the expected molecular weight of SDC4-ect (~17 kDa) was observed in either the CM or the lysates, even in the presence of heparin. The presence of actin in the lysates confirmed equal protein loading in each well. The functionality of the anti-6His antibody was validated by loading an in-house expressed His-tagged control protein, which showed a clear immunoreactive band (positive CTRL).

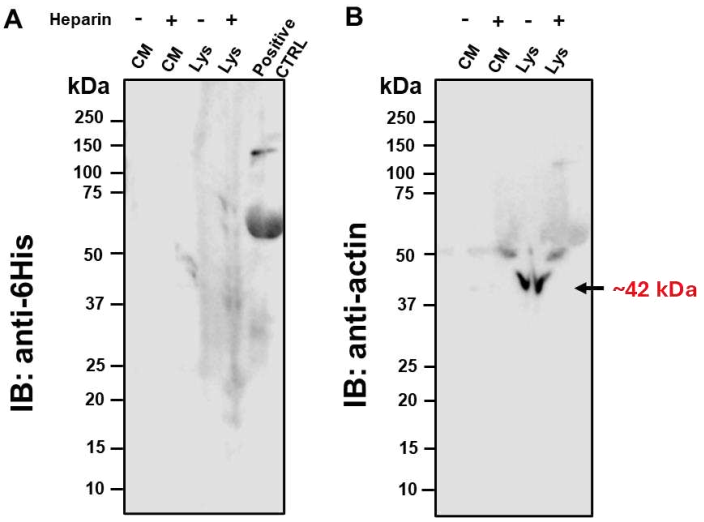

Figure 3. **First attempt of SDC4-ect recombinant protein expression.** SDC4-ect was transfected in HEK293T cells. In "+" conditions, heparin was added 4 h post-transfection to release forms eventually bound to the ECM. **A** Conditioned media (CM) and cell lysates (Lys) were collected after 72 h and analysed by immunoblotting under reducing conditions using anti-His Tag antibody. No immunoreactive band corresponding to the expected molecular weight (17 kDa) was observed. Positive control (CTRL) refers to a His-tagged protein loaded together with samples for proving antibody's reactivity and specificity against 6-His tag. **B** Immunoblot anti- actin was used as a loading control.

Two likely causes may explain this result: protein degradation during the incubation period or loss of the His tag during expression. The ectodomain of syndecan4 is relatively small (127 residues) and may be susceptible to proteolytic degradation by pericellular and extracellular proteases. It is well known that several metalloproteinases, including members of the MMP and ADAMTS families [239], can act as sheddases, cleaving multiple sites within the SDC4 ectodomain. Thus, it is likely that once expressed, the recombinant protein is rapidly proteolyzed by numerous cellular proteases. The loss of the 6x His tag could be tested using an anti-syndecan4 antibody. However, the lack of a commercially available, specific anti-syndecan4 antibody prevented us further from testing this hypothesis.

We proceeded to optimize the expression protocol by testing the efficacy of several inhibitors that may prevent SDC4-ect degradation. Specifically, the synthetic inhibitor CT1746 and a protease inhibitor cocktail (PIC) targeting serine and cysteine proteases were used, both individually and in combination. As heparin did not affect SDC4-ect expression (**Figure 3**), the effect of heparin was not investigated in this context. As shown in **Figure 4**, in the absence of inhibitors, no immunoreactive bands were detected at any time points examined, thus confirming the results from the pilot experiment described in Figure 3. However, in the presence of CT1746, either alone or in combination with PIC, a main band corresponding to the expected molecular weight of the SDC4-ect was observed. The polydispersity of the bands was indicative of glycosylation (potentially O-glycosylation). However, this should be confirmed by subjecting the samples to deglycosylation using heparinase, chondroitinase ABC, and PNGase. Notably, in the presence of PIC alone, no specific band for SDC4-ect was detected, suggesting that the primary protective effect is contributed by CT1746. Additionally, after 48 hours the SDC4-ect band was markedly more intense, indicating maximal availability of SDC4-ect in the CM at this time point. Therefore, this time point was selected and used for all subsequent experiments.

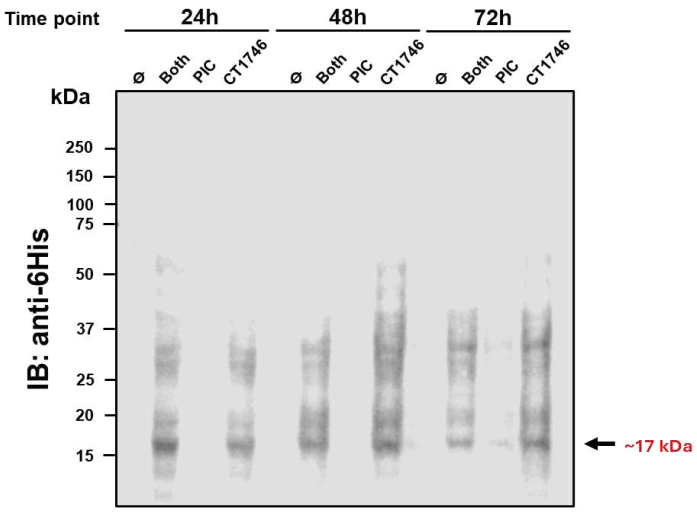

***Figure 4*. The hydroxamate-based inhibitor CT1746 allowed SDC4-ect expression and detection in CM.** Transient transfection of SDC4-ect was performed and analysed at three different time points in the presence of 100 µM CT1746, the proteinase inhibitor cocktail (PIC), or both (both). In the absence of both inhibitors (denoted as Ø), no immunoreactive bands were observed. Similarly, when only PIC was used, no bands were detected. However, in the presence of CT1746, either alone or in combination with PIC, a band corresponding to the expected molecular weight of 17 kDa was observed, demonstrating the effectiveness of CT1746 in preventing SDC4-ect degradation. This result was confirmed in with a second independent experiment.

CT1746 is a hydroxamate-based compound, known for its ability to inhibit several MMPs [243]. The hydroxamate moiety in this molecule acts as a chelator of zinc ions, essential for metalloenzyme activity, resulting in MMP inhibition[244]. Of note, the PIC used in this experiment did not have EDTA as a metalloproteinase inhibitor. In summary, we successfully identified optimal conditions for obtaining appreciable expression of recombinant SDC4-ect and confirmed that syndecan4 is proteolyzed by metalloproteases. This allowed us to proceed with large-scale expression, using the best conditions identified (48-hour transfection with CT1746 inhibitor) to move forward with protein purification.

SDC4-ect is lost during protein purification

Initially, CM from large-scale transfection was filtered using a vacuum filtration apparatus and concentrated. The concentrated CM was then subjected to nickel affinity chromatography, leveraging the affinity between the side chains of the histidine residues in the C-terminal His-tag of SDC4-ect and the nickel ions associated with the stationary phase of the column. The

recombinant protein in the medium thus remained bound to the column and was subsequently eluted by applying an imidazole gradient. Imidazole, with a higher affinity for nickel ions, competes with the histidine residues in the tag, enabling the release of SDC4-ect from the column. The result of this purification step is shown in **Figure 5**, where fractions 5, 6, and 7 (eluted at 90 mM imidazole) anti-6x His tag-immunoreactive bands at the expected molecular weight. Notably, the initial CM sample shows a markedly reduced presence of SDC4-ect, indicated by a faint band at 17kDa. This likely results from the partial, progressive degradation of SDC4-ect following the removal of the inhibitor during filtration and sample concentration steps. Additionally, CBB staining reveals that fractions positive for SDC4-ect (fractions 5, 6, and 7) are still heavily contaminated with other proteins present in the CM, which were not removed during this purification step. Therefore, an additional purification step was required.

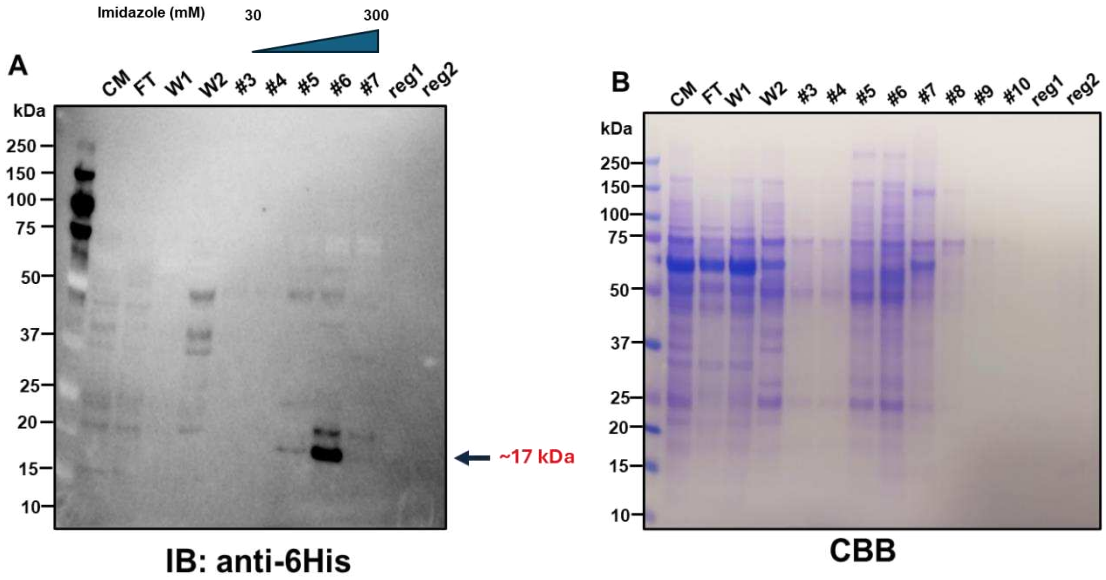

***Figure 5*. SDC4-ect first step purification by affinity chromatography.** 48 hours post-transfection, CM was harvested, filtered and concentrated. The concentrated CM was then subjected to purification using a Ni-Sepharose column. An aliquot of each purification step was taken and analysed through anti-His tag immunoblot (**A**) and CBB staining (**B**) under reducing conditions. Arrow indicates the immunoreactive bands, corresponding to the expected SDC4-ect molecular weight of approximately 17 kDa.CM: conditioned medium; FT: flow-through; W1: wash 1; W2: wash 2; Reg1: regeneration 1; Reg2: regeneration 2.

The pool of SDC4-ect-positive fractions from the previous step was subjected to further purification via anion exchange chromatography. The Sepharose resin contained -N+$(CH_3)_3$ groups, which may electrostatically interact with the negatively charged heparan sulfate chains

covalently bound to SDC4-ect, allowing the protein to associate with the stationary phase. To elute SDC4-ect, a NaCl gradient (150-700 mM) was applied to incrementally increase ionic strength.

Unfortunately, as shown by the WB results in **Figure 6-A**, no immunoreactive bands corresponding to SDC4-ect were detected, even in the starting pool. This suggests that the recombinant protein was irreversibly lost during purification and/or storage, confirming its high instability. Small proteins, particularly recombinant ones lacking structured domains, tend to be thermodynamically unstable and often more labile, undergoing degradation or denaturation. However, CBB staining in **Figure 6-B** indicated a band at the expected molecular weight in fractions 7 and 8. To rule out the possibility that this band represented SDC4-ect, which might have been undetected by the antibody for unknown reasons, the band was excised and analysed by mass spectrometry, performed by the group of Dr. Sneha Pinto (University of Surrey). Mass spectrometry results confirmed that the ~17 kDa band corresponded to the Eukaryotic Translation Initiation Factor 5A-1 (EIF5A), which indeed has a molecular weight of 17 kDa, conclusively indicating the definitive loss of the recombinant protein.

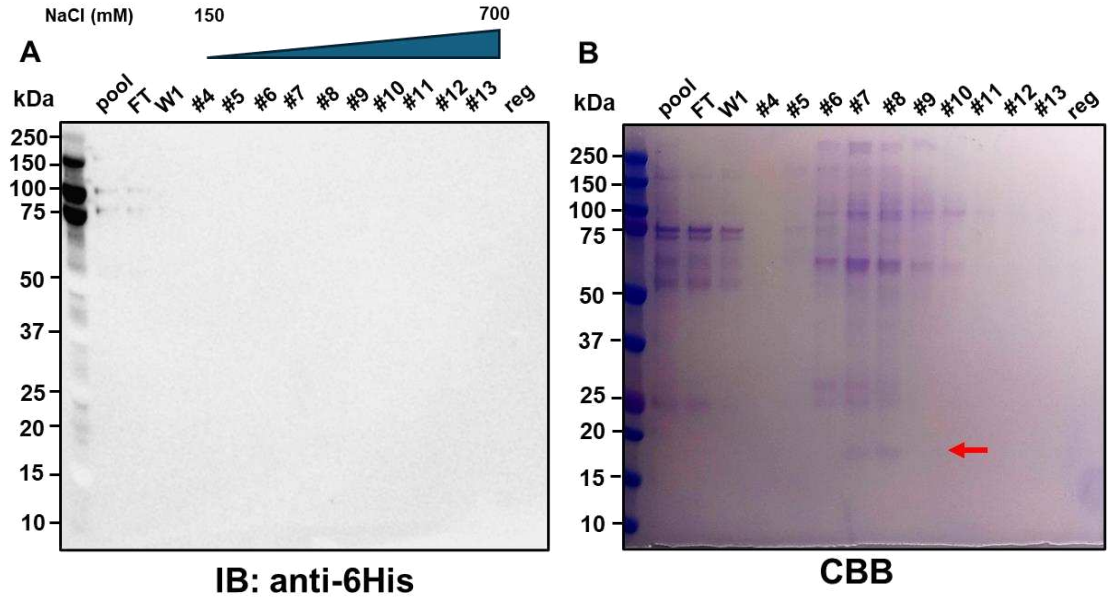

***Figure 6.* SDC4-ect second step purification by ion exchange chromatography.** The pool of SDC4-ect-positive fractions from affinity chromatography was subjected to a second round of purification using an Q Sepharose column. An aliquot from each purification step was collected and analysed via anti-His tag immunoblot (**A**) and CBB staining (**B**) under reducing conditions. Red arrows indicate the bands corresponding to the expected molecular weight of SDC4-ect that were excised and subjected to mass spectrometry analysis. FT: flow-through; W1: wash 1; reg: regeneration.

Conclusion and Perspectives

Using the MMP inhibitor CT1746, we successfully expressed the SDC4-ect protein in HEK293T human cell line. Specifically, in the presence of CT1746, we observed the release of the recombinant SDC4-ect into the conditioned medium, from which its isolation was carried on. Unfortunately, due to the small size of the protein and its susceptibility to metalloprotease cleavage, it was rapidly lost following the initial chromatographic steps, preventing completion of the purification process. CT1746 is essential to maintain the expression of SDC4-ect. However, during filtration and concentration processes, the inhibitor is removed, potentially allowing MMP activity to resume. A limitation of CT1746 is its low solubility in aqueous solutions, which prevents its use at high concentrations, as it quickly precipitates. Testing other hydroxamate-based inhibitors would be of interest, as would identifying the specific protease responsible for SDC4 proteolysis. Another possible approach to enhance SDC4-ect expression is the use of bacterial expression systems, such as the *BL21* strain of *E. coli*, which was successfully employed by Gondelaud *et al*. for the expression of various human syndecan ectodomains [245]. However, if expressed in bacteria, SDC4-ect will not be glycosylated, thus preventing us from properly testing the biological activity of SDC4-ect. Once recombinant SDC4-ect yield and purity are improved, further investigation into its potential effect on ADAMTS-4 and ADAMTS-5 activity will be possible, as well as studies on enzyme-inhibitor interactions.

REFERENCES

[1] H. Sies, C. Berndt, and D. P. Jones, "Oxidative Stress," *Annual Review ofBiochemistry*, vol. 86, pp. 715–748, 2017, doi: 10.1016/B978-0-12-411604-7.00006-4.

[2] J. D. Hayes, A. T. Dinkova-Kostova, and K. D. Tew, "Oxidative Stress in Cancer," *Cancer Cell*, vol. 38, pp. 167–197, 2020, doi: 10.1016/j.ccell.2020.06.001.

[3] K. Jomova *et al.*, "Reactive oxygen species, toxicity, oxidative stress, and antioxidants: chronic diseases and aging," *Arch Toxicol*, vol. 97, pp. 2499–2574, 2023, doi: 10.1007/s00204-023-03562-9.

[4] R. Z. Zhao, S. Jiang, L. Zhang, and Z. Bin Yu, "Mitochondrial electron transport chain, ROS generation and uncoupling (Review)," *Int J Mol Med*, vol. 44, pp. 3–15, 2019, doi: 10.3892/ijmm.2019.4188.

[5] D. J. R. Fulton *et al.*, "Reactive oxygen and nitrogen species in the development of pulmonary hypertension," *Antioxidants*, vol. 6, 2017, doi: 10.3390/antiox6030054.

[6] R. Thanan *et al.*, "Oxidative stress and its significant roles in neurodegenerative diseases and cancer," *Int J Mol Sci*, vol. 16, pp. 193–217, 2014, doi: 10.3390/ijms16010193.

[7] G. Barrera, "Oxidative Stress and Lipid Peroxidation Products in Cancer Progression and Therapy," *ISRN Oncol*, vol. 2012, pp. 1–21, 2012, doi: 10.5402/2012/137289.

[8] H. K. Krishnamurthy *et al.*, "Oxidative stress: fundamentals and advances in quantification techniques," *Front Chem*, vol. 12, 2024, doi: 10.3389/fchem.2024.1470458.

[9] N. Couto, J. Wood, and J. Barber, "The role of glutathione reductase and related enzymes on cellular redox homoeostasis network," *Free Radic Biol Med*, vol. 95, pp. 27–42, 2016, doi: 10.1016/j.freeradbiomed.2016.02.028.

[10] Y. Sheng *et al.*, "Superoxide dismutases and superoxide reductases," *Chem Rev*, vol. 114, pp. 3854–3918, 2014, doi: 10.1021/cr4005296.

[11] H. N. Kirkman and G. F. Gaetani, "Mammalian catalase: a venerable enzyme with new mysteries," *Trends Biochem Sci*, vol. 32, pp. 44–50, 2007, doi: 10.1016/j.tibs.2006.11.003.

[12] E. A. Elko *et al.*, “Peroxiredoxins and Beyond; Redox Systems Regulating Lung Physiology and Disease,” *Antioxid Redox Signal*, vol. 31, pp. 1070–1091, 2019, doi: 10.1089/ars.2019.7752.

[13] R. Brigelius-Flohé and M. Maiorino, “Glutathione peroxidases,” *Biochim Biophys Acta Gen Subj*, vol. 1830, pp. 3289–3303, 2013, doi: 10.1016/j.bbagen.2012.11.020.

[14] J. S. Rodríguez-Zavala, L. F. Calleja, R. Moreno-Sánchez, and B. Yoval-Sánchez, “Role of Aldehyde Dehydrogenases in Physiopathological Processes,” *Chem Res Toxicol*, vol. 32, no. 3, pp. 405–420, Mar. 2019, doi: 10.1021/acs.chemrestox.8b00256.

[15] Trevor M. Penning, “The Aldo-Keto Reductases (AKRs): Overview,” *Chem Biol Interact*, vol. 234, pp. 236–246, 2015, doi: 10.1016/j.cbi.2014.09.024.The.

[16] U. Oppermann, “Carbonyl reductases: The complex relationships of mammalian carbonyl- and quinone-reducing enzymes and their role in physiology,” 2007. doi: 10.1146/annurev.pharmtox.47.120505.105316.

[17] J. D. Hayes, J. U. Flanagan, and I. R. Jowsey, “Glutathione transferases,” *Annu Rev Pharmacol Toxicol*, vol. 45, pp. 51–88, 2005, doi: 10.1146/annurev.pharmtox.45.120403.095857.

[18] Y. S. Keum, “Regulation of Nrf2-mediated phase ii detoxification and anti-oxidant genes,” *Biomol Ther (Seoul)*, vol. 20, pp. 144–151, 2012, doi: 10.4062/biomolther.2012.20.2.144.

[19] J. A. Johnson *et al.*, “The Nrf2-ARE pathway: An indicator and modulator of oxidative stress in neurodegeneration,” *Ann N Y Acad Sci*, vol. 1147, pp. 61–69, 2008, doi: 10.1196/annals.1427.036.

[20] S. Saha, B. Buttari, E. Panieri, E. Profumo, and L. Saso, “An Overview of Nrf2 Signaling Pathway and Its Role in Inflammation,” *Molecules*, vol. 25, 2020, doi: 10.3390/molecules25225474.

[21] A. P. Shanbhag and P. Bhowmik, “Cancer to Cataracts: The Mechanistic Impact of Aldo-Keto Reductases in Chronic Diseases,” *Yale J Biol Med*, vol. 97, pp. 179–204, 2024, doi: 10.59249/VTBV6559.

[22] O. A. Barski, S. M. Tipparaju, and A. Bhatnagar, “The aldo-keto reductase superfamily and its role in drug metabolism and detoxification,” *Drug Metab Rev*, vol. 40, pp. 553–624, 2008, doi: 10.1080/03602530802431439.

[23] T. L. Rižner and T. M. Penning, “Role of aldo-keto reductase family 1 (AKR1) enzymes in human steroid metabolism,” *Steroids*, vol. 79, pp. 49–63, 2014, doi: 10.1016/j.steroids.2013.10.012.

[24] J. Fujii, T. Homma, S. Miyata, and M. Takahashi, “Pleiotropic actions of aldehyde reductase (AKR1A1),” *Metabolites*, vol. 11, 2021, doi: 10.3390/metabo11060343.

[25] W. H. Tang, K. A. Martin, and J. Hwa, “Aldose reductase, oxidative stress, and diabetic mellitus,” *Front Pharmacol*, vol. 3, 2012, doi: 10.3389/fphar.2012.00087.

[26] K. V Ramana *et al.*, “Characterization of the glutathione binding site of aldose reductase,” *Chem Biol Interact*, vol. 130, pp. 537–548, 2001, [Online]. Available: www.elsevier.com/locate/chembiont

[27] K. V. Ramana and S. K. Srivastava, “Aldose reductase: A novel therapeutic target for inflammatory pathologies,” *International Journal of Biochemistry and Cell Biology*, vol. 42, pp. 17–20, 2010, doi: 10.1016/j.biocel.2009.09.009.

[28] S. Endo, T. Matsunaga, and T. Nishinaka, “The role of AKR1B10 in physiology and pathophysiology,” *Metabolites*, vol. 11, no. 6, 2021, doi: 10.3390/metabo11060332.

[29] F. X. Ruiz, S. Porté, X. Parés, and J. Farrés, “Biological role of aldo-keto reductases in retinoic acid biosynthesis and signaling,” *Front Pharmacol*, vol. 3, 2012, doi: 10.3389/fphar.2012.00058.

[30] N. Noy, “Between death and survival: Retinoic acid in regulation of apoptosis,” *Annu Rev Nutr*, vol. 30, pp. 201–217, 2010, doi: 10.1146/annurev.nutr.28.061807.155509.

[31] X. Ye *et al.*, “Aldo-keto reductase 1B10 as a Carcinogenic but Not a Prognostic Factor in Colorectal Cancer,” *J Cancer*, vol. 15, pp. 1657–1667, 2024, doi: 10.7150/jca.91064.

[32] T. Matsunaga *et al.*, “Aldo-keto reductase 1B10 promotes development of cisplatin resistance in gastrointestinal cancer cells through down-regulating peroxisome

proliferator-activated receptor-γ-dependent mechanism," *Chem Biol Interact*, vol. 256, pp. 142–153, 2016, doi: 10.1016/j.cbi.2016.07.008.

[33] T. H. Jang *et al.*, "The Role of AKR1B10 in Lung Cancer Malignancy Induced by Sublethal Doses of Chemotherapeutic Drugs," *Cancers (Basel)*, vol. 16, 2024, doi: 10.3390/cancers16132428.

[34] T. M. Penning, P. Wangtrakuldee, and R. J. Auchus, "Structural and functional biology of aldo-keto reductase steroid-transforming enzymes," *Endocr Rev*, vol. 40, pp. 447–475, 2019, doi: 10.1210/er.2018-00089.

[35] N. Beranič, B. Štefane, B. Brus, S. Gobec, and T. L. Rižner, "New enzymatic assay for the AKR1C enzymes," *Chem Biol Interact*, vol. 202, no. 1–3, pp. 204–209, 2013, doi: 10.1016/j.cbi.2012.12.003.

[36] T. Šmuc, N. Hevir, M. Ribič-Pucelj, B. Husen, H. Thole, and T. L. Rižner, "Disturbed estrogen and progesterone action in ovarian endometriosis," *Mol Cell Endocrinol*, vol. 301, pp. 59–64, 2009, doi: 10.1016/j.mce.2008.07.020.

[37] M. C. Byrns, L. Duan, S. H. Lee, I. A. Blair, and T. M. Penning, "Aldo-keto reductase 1C3 expression in MCF-7 cells reveals roles in steroid hormone and prostaglandin metabolism that may explain its over-expression in breast cancer," *Journal of Steroid Biochemistry and Molecular Biology*, vol. 118, pp. 177–187, 2010, doi: 10.1016/j.jsbmb.2009.12.009.

[38] T. Šmuc, N. Hevir, M. Ribič-Pucelj, B. Husen, H. Thole, and T. L. Rižner, "Disturbed estrogen and progesterone action in ovarian endometriosis," *Mol Cell Endocrinol*, vol. 301, no. 1–2, pp. 59–64, Mar. 2009, doi: 10.1016/j.mce.2008.07.020.

[39] C. M. Zeng *et al.*, "Aldo-keto reductase AKR1C1-AKR1C4: Functions, regulation, and intervention for anti-cancer therapy," *Front Pharmacol*, vol. 8, 2017, doi: 10.3389/fphar.2017.00119.

[40] T. L. Rižner, T. Šmuc, R. Rupreht, J. Šinkovec, and T. M. Penning, "AKR1C1 and AKR1C3 may determine progesterone and estrogen ratios in endometrial cancer," *Mol Cell Endocrinol*, vol. 248, pp. 126–135, 2006, doi: 10.1016/j.mce.2005.10.009.

[41] N. Nikolaou *et al.*, “AKR1D1 is a novel regulator of metabolic phenotype in human hepatocytes and is dysregulated in non-alcoholic fatty liver disease,” *Metabolism*, vol. 99, pp. 67–80, Oct. 2019, doi: 10.1016/j.metabol.2019.153947.

[42] S. Nagini, P. R. Kallamadi, K. K. K. Tanagala, and G. B. Reddy, “Aldo-keto reductases: Role in cancer development and theranostics,” *Oncol Res*, vol. 32, no. 8, pp. 1287–1308, 2024, doi: 10.32604/or.2024.049918.

[43] T. M. Penning, S. Jonnalagadda, P. C. Trippier, and T. L. Rižner, “Aldo-keto reductases and cancer drug resistance,” *Pharmacol Rev*, vol. 73, pp. 1150–1171, 2021, doi: 10.1124/pharmrev.120.000122.

[44] J. Fujii, T. Homma, S. Miyata, and M. Takahashi, “Pleiotropic actions of aldehyde reductase (Akr1a),” *Metabolites*, vol. 11, no. 6, 2021, doi: 10.3390/metabo11060343.

[45] M. Singh, A. Kapoor, and A. Bhatnagar, “Physiological and pathological roles of aldose reductase,” *Metabolites*, vol. 11, 2021, doi: 10.3390/metabo11100655.

[46] X. Chu *et al.*, “Overview of human 20 alpha-hydroxysteroid dehydrogenase (AKR1C1): Functions, regulation, and structural insights of inhibitors,” *Chem Biol Interact*, vol. 351, 2022, doi: 10.1016/j.cbi.2021.109746.

[47] T. L. Rižner, H. K. Lin, D. M. Peehl, S. Steckelbroeck, D. R. Bauman, and T. M. Penning, “Human type 3 3α-hydroxysteroid dehydrogenase (aldo-keto reductase 1C2) and androgen metabolism in prostate cells,” *Endocrinology*, vol. 144, no. 7, pp. 2922–2932, Jul. 2003, doi: 10.1210/en.2002-0032.

[48] T. M. Penning, “AKR1C3 (type 5 17β-hydroxysteroid dehydrogenase/prostaglandin F synthase): Roles in malignancy and endocrine disorders,” *Mol Cell Endocrinol*, vol. 489, pp. 82–91, 2019, doi: 10.1016/j.mce.2018.07.002.

[49] T. M. Penning and J. E. Drury, “Human aldo-keto reductases: Function, gene regulation, and single nucleotide polymorphisms,” Aug. 15, 2007. doi: 10.1016/j.abb.2007.04.024.

[50] M. Chen and T. M. Penning, “5β-Reduced steroids and human Δ4-3-ketosteroid 5β-reductase (AKR1D1),” *Steroids*, vol. 83, pp. 17–26, May 2014, doi: 10.1016/j.steroids.2014.01.013.

[51] P. Malátková, E. Maser, and V. Wsól, “Human Carbonyl Reductases,” *Curr Drug Metab*, vol. 11, pp. 639–658, 2010, [Online]. Available: http://www.sdr-enzymes.org.

[52] F. Hoffmann and E. Maser, “Carbonyl reductases and pluripotent hydroxysteroid dehydrogenases of the short-chain dehydrogenase/reductase superfamily,” *Drug Metab Rev*, vol. 39, pp. 87–144, 2007, doi: 10.1080/03602530600969440.

[53] S. Endo *et al.*, “Human carbonyl reductase 4 is a mitochondrial NADPH-dependent quinone reductase,” *Biochem Biophys Res Commun*, vol. 377, no. 4, pp. 1326–1330, Dec. 2008, doi: 10.1016/j.bbrc.2008.11.003.

[54] U. Oppermann, “Carbonyl reductases: The complex relationships of mammalian carbonyl- and quinone-reducing enzymes and their role in physiology,” *Annu Rev Pharmacol Toxicol*, vol. 47, pp. 293–322, 2007, doi: 10.1146/annurev.pharmtox.47.120505.105316.

[55] G. L. Forrest and B. Gonzalez, “Carbonyl reductase,” *Chem Biol Interact*, vol. 129, pp. 21–40, 2000, [Online]. Available: www.elsevier.com/locate/chembiont

[56] H. Wirth and B. Wermuth, “Immunohistochemical Localization of Carbonyl Reductase in Human Tissues,” *The Journal of Histochemistry and Cytochemistry*, vol. 40, pp. 1817–1863, 1992.

[57] R. Moschini *et al.*, “Kinetic features of carbonyl reductase 1 acting on glutathionylated aldehydes,” *Chem Biol Interact*, vol. 276, pp. 127–132, 2017, doi: 10.1016/j.cbi.2017.03.003.

[58] R. L. Bateman, D. Rauh, B. Tavshanjian, and K. M. Shokat, “Human carbonyl reductase 1 is an S-nitrosoglutathione reductase,” *Journal of Biological Chemistry*, vol. 283, pp. 35756–35762, 2008, doi: 10.1074/jbc.M807125200.

[59] M. A. Rashid, M. Haque, and M. Akbar, “Detoxification of carbonyl compounds by carbonyl reductase in neurodegeneration,” *Adv Neurobiol*, vol. 12, pp. 355–365, 2016, doi: 10.1007/978-3-319-28383-8_19.

[60] L. Mao *et al.*, “Carbonyl Reductase 1 Attenuates Ischemic Brain Injury by Reducing Oxidative Stress and Neuroinflammation”, doi: 10.1007/s12975-021-00912-6/Published.

[61] A. Scheepers, H. G. Joost, and A. Schürmann, “The glucose transporter families SGLT and GLUT: Molecular basis of normal and aberrant function,” *Journal of Parenteral and Enteral Nutrition*, vol. 28, pp. 364–371, 2004, doi: 10.1177/0148607104028005364.

[62] Y. Liu *et al.*, “Signaling pathways of oxidative stress response: the potential therapeutic targets in gastric cancer,” *Front Immunol*, vol. 14, 2023, doi: 10.3389/fimmu.2023.1139589.

[63] P. González, P. Lozano, G. Ros, and F. Solano, “Hyperglycemia and Oxidative Stress: An Integral, Updated and Critical Overview of Their Metabolic Interconnections,” Jun. 01, 2023, *Multidisciplinary Digital Publishing Institute (MDPI)*. doi: 10.3390/ijms24119352.

[64] O. M. Ighodaro, “Molecular pathways associated with oxidative stress in diabetes mellitus,” *Biomedicine and Pharmacotherapy*, vol. 108, pp. 656–662, 2018, doi: 10.1016/j.biopha.2018.09.058.

[65] D. Cosentino-Gomes, N. Rocco-Machado, and J. R. Meyer-Fernandes, “Cell signaling through protein kinase C oxidation and activation,” *Int J Mol Sci*, vol. 13, pp. 10697–10721, 2012, doi: 10.3390/ijms130910697.

[66] S. Brings, T. Fleming, M. Freichel, M. U. Muckenthaler, S. Herzig, and P. P. Nawroth, “Dicarbonyls and advanced glycation end-products in the development of diabetic complications and targets for intervention,” *Int J Mol Sci*, vol. 18, 2017, doi: 10.3390/ijms18050984.

[67] K. V. Ramana and S. K. Srivastava, “Aldose reductase: A novel therapeutic target for inflammatory pathologies,” *International Journal of Biochemistry and Cell Biology*, vol. 42, pp. 17–20, 2010, doi: 10.1016/j.biocel.2009.09.009.

[68] L. jun Yan, “Redox imbalance stress in diabetes mellitus: Role of the polyol pathway,” *Animal Model Exp Med*, vol. 1, pp. 7–13, 2018, doi: 10.1002/ame2.12001.

[69] A. Singh Grewal, S. Bhardwaj, D. Pandita, V. Lather, and B. Singh Sekhon, “Updates on Aldose Reductase Inhibitors for Management of Diabetic Complications and Non-diabetic Diseases,” *Mini-Reviews in Medicinal Chemistry*, vol. 16, no. 2, pp. 120–162, 2015, doi: 10.2174/1389557515666150909143737.

[70] C. A. Thorne, A. C. Grey, J. C. Lim, and P. J. Donaldson, “The Synergistic Effects of Polyol Pathway-Induced Oxidative and Osmotic Stress in the Aetiology of Diabetic Cataracts,” *Int J Mol Sci*, vol. 25, 2024, doi: 10.3390/ijms25169042.

[71] S. S. M. Chung, E. C. M. Ho, K. S. L. Lam, and S. K. Chung, “Contribution of polyol pathway to diabetes-induced oxidative stress,” *Journal of the American Society of Nephrology*, vol. 14, pp. 233–236, 2003, doi: 10.1097/01.asn.0000077408.15865.06.

[72] B. Collier, L. A. Dossett, A. K. May, and J. J. Diaz, “Glucose control and the inflammatory response,” *Nutrition in Clinical Practice*, vol. 23, pp. 3–15, 2008, doi: 10.1177/011542650802300103.

[73] T. Zhang, C. Ma, Z. Zhang, H. Zhang, and H. Hu, “NF-κB signaling in inflammation and cancer,” *MedComm (Beijing)*, vol. 2, pp. 618–653, 2021, doi: 10.1002/mco2.104.

[74] T. Lawrence, “The nuclear factor NF-kappaB pathway in inflammation.,” *Cold Spring Harb Perspect Biol*, vol. 1, 2009, doi: 10.1101/cshperspect.a001651.

[75] M. Serasanambati and S. R. Chilakapati, “Function of Nuclear Factor Kappa B (NF-kB) in Human Diseases-A Review,” *South Indian Journal of Biological Sciences*, vol. 2, pp. 368–387, 2016, doi: 10.22205/sijbs/2016/v2/i4/103443.

[76] M.-J. Lallena *et al.*, “Activation of IB Kinase by Protein Kinase C Isoforms,” *Mol Cell Biol*, vol. 19, no. 3, pp. 2180–2188, 1999.

[77] K. Kierdorf and G. Fritz, “RAGE regulation and signaling in inflammation and beyond,” *J Leukoc Biol*, vol. 94, pp. 55–68, Mar. 2013, doi: 10.1189/jlb.1012519.

[78] M. Z. Banday, A. S. Sameer, and S. Nissar, “Pathophysiology of diabetes: An overview,” *Avicenna J Med*, vol. 10, pp. 174–188, Oct. 2020, doi: 10.4103/ajm.ajm_53_20.

[79] O. Ozougwu, “The pathogenesis and pathophysiology of type 1 and type 2 diabetes mellitus,” *Journal of Physiology and Pathophysiology*, vol. 4, pp. 46–57, 2013, doi: 10.5897/jpap2013.0001.

[80] J. B. Cole and J. C. Florez, “Genetics of diabetes mellitus and diabetes complications,” *Nat Rev Nephrol*, vol. 16, no. 7, pp. 377–390, 2020, doi: 10.1038/s41581-020-0278-5.

[81] S. D. De Ferranti *et al.*, “Type 1 diabetes mellitus and cardiovascular disease a scientific statement from the american heart association andamerican diabetes association,” *Circulation*, vol. 130, no. 13, pp. 1110–1130, 2014, doi: 10.1161/CIR.0000000000000034.

[82] F. M. Turnbull *et al.*, “Intensive glucose control and macrovascular outcomes in type 2 diabetes,” *Diabetologia*, vol. 52, pp. 2288–2298, 2009, doi: 10.1007/s00125-009-1470-0.

[83] K. R. Tuttle *et al.*, “Diabetic kidney disease: A report from an ADA consensus conference,” *Diabetes Care*, vol. 37, pp. 2864–2883, 2014, doi: 10.2337/dc14-1296.

[84] R. Pop-Busui *et al.*, “Diabetic neuropathy: A position statement by the American diabetes association,” *Diabetes Care*, vol. 40, pp. 136–154, 2017, doi: 10.2337/dc16-2042.

[85] G. Castelli, K. M. Desai, and R. E. Cantone, “Peripheral Neuropathy: Evaluation and Differential Diagnosis,” *American Family Physician www.aafp.org/afp*, vol. 102, 2020, [Online]. Available: www.choosingwisely.org.

[86] J. F. Hejtmancik and A. Shiels, “Overview of the Lens,” *Prog Mol Biol Transl Sci*, vol. 134, pp. 119–127, 2015, doi: 10.1016/bs.pmbts.2015.04.006.

[87] I. G. Obrosova, S. S. M. Chung, and P. F. Kador, “Diabetic cataracts: Mechanisms and management,” *Diabetes Metab Res Rev*, vol. 26, pp. 172–180, 2010, doi: 10.1002/dmrr.1075.

[88] E. Kubo, T. Urakami, N. Fatma, Y. Akagi, and D. P. Singh, “Polyol pathway-dependent osmotic and oxidative stresses in aldose reductase-mediated apoptosis in human lens epithelial cells: Role of AOP2,” *Biochem Biophys Res Commun*, vol. 314, pp. 1050–1056, 2004, doi: 10.1016/j.bbrc.2004.01.002.

[89] P. Venkatesh, ; Anup, and K. Affiliations, “Anthracyclines,” *Treasure Island, FL: StatPearls*, 2023, [Online]. Available: https://www.ncbi.nlm.nih.gov/sites/books/NBK538187/?report=printable

[90] M. B. Martins-Teixeira and I. Carvalho, “Antitumour Anthracyclines: Progress and Perspectives,” *ChemMedChem*, vol. 15, no. 11, pp. 933–948, 2020, doi: 10.1002/cmdc.202000131.

[91] R. Mattioli, A. Ilari, B. Colotti, L. Mosca, F. Fazi, and G. Colotti, “Doxorubicin and other anthracyclines in cancers: Activity, chemoresistance and its overcoming,” *Mol Aspects Med*, vol. 93, no. May, p. 101205, 2023, doi: 10.1016/j.mam.2023.101205.

[92] T. Saleem, ; Anup, and K. Affiliations, “Daunorubicin Continuing Education Activity,” *Treasure Island (FL): StatPearls*, 2023, [Online]. Available: https://www.ncbi.nlm.nih.gov/books/NBK559073/?report=printable

[93] A. Kelly Johnson-Arbor and R. Dubey Affiliations, “Doxorubicin Continuing Education Activity,” *Treasure Island (FL): StatPearls*, 2023, [Online]. Available: https://www.ncbi.nlm.nih.gov/books/NBK459232/?report=printable

[94] M. Khasraw, R. Bell, and C. Dang, “Epirubicin: Is it like doxorubicin in breast cancer? A clinical review,” *The Breast*, vol. 21, pp. 142–149, 2012, doi: 10.1016/j.breast.2011.12.012.

[95] M. M. Buckley and H. M. Lamb, “Oral Idarubicin,” *Drugs Aging*, vol. 11, pp. 61–86, 1997.

[96] S. V Onrust and H. M. Lamb, “Valrubicin,” *Drugs Aging*, vol. 12, pp. 69–75, 1999.

[97] R. A. Bilardi, K. I. Kimura, D. R. Phillips, and S. M. Cutts, “Processing of anthracycline-DNA adducts via DNA replication and interstrand crosslink repair pathways,” *Biochem Pharmacol*, vol. 83, pp. 1241–1250, 2012, doi: 10.1016/j.bcp.2012.01.029.

[98] R. A. Forrest *et al.*, “Activation of DNA damage response pathways as a consequence of anthracycline-DNA adduct formation,” *Biochem Pharmacol*, vol. 83, pp. 1602–1612, 2012, doi: 10.1016/j.bcp.2012.02.026.

[99] V. Visone, I. Szabó, G. Perugino, F. Hudecz, Z. Bánóczi, and A. Valenti, “Topoisomerases inhibition and DNA binding mode of daunomycin–oligoarginine conjugate,” *J Enzyme Inhib Med Chem*, vol. 35, pp. 1363–1371, 2020, doi: 10.1080/14756366.2020.1780226.

[100] K. Evans-Roberts and A. Maxwell, “DNA Topoisomerases,” *EcoSal Plus*, vol. 3, 2009, doi: 10.1128/ecosalplus.4.4.9.

[101] K. B. Wallace, V. A. Sardão, and P. J. Oliveira, “Mitochondrial Determinants of Doxorubicin-Induced Cardiomyopathy,” *Circ Res*, vol. 126, pp. 926–941, 2020, doi: 10.1161/CIRCRESAHA.119.314681.

[102] M. Nikolaou, A. Pavlopoulou, A. G. Georgakilas, and E. Kyrodimos, “The challenge of drug resistance in cancer treatment: a current overview,” *Clin Exp Metastasis*, vol. 35, pp. 309–318, 2018, doi: 10.1007/s10585-018-9903-0.

[103] J. L. Nitiss’ and W. T. Beck, “Antitopoisomerase Drug Action and Resistance,” *Eur J Cancer*, vol. 32, pp. 958–966, 1996.

[104] Y. Okada, A. Tosaka, Y. Nimura, A. Kikuchi, S. Yoshida, and M. Suzuki, “Atypical multidrug resistance may be associated with catalytically active mutants of human DNA topoisomerase II a,” *Gene*, vol. 272, pp. 141–148, 2001, [Online]. Available: www.elsevier.com/locate/gene

[105] J. I. Fletcher, R. T. Williams, M. J. Henderson, M. D. Norris, and M. Haber, “ABC transporters as mediators of drug resistance and contributors to cancer cell biology,” *Drug Resistance Updates*, vol. 26, pp. 1–9, 2016, doi: 10.1016/j.drup.2016.03.001.

[106] S. Kachalaki, M. Ebrahimi, L. Mohamed Khosroshahi, S. Mohammadinejad, and B. Baradaran, “Cancer chemoresistance; Biochemical and molecular aspects: a brief overview,” *European Journal of Pharmaceutical Sciences*, vol. 89, pp. 20–30, 2016, doi: 10.1016/j.ejps.2016.03.025.

[107] S. P. C. Cole, “Multidrug resistance protein 1 (mrp1, abcc1), a ‘multitasking’ atp-binding cassette (abc,) transporter,” *Journal of Biological Chemistry*, vol. 289, pp. 30880–30888, 2014, doi: 10.1074/jbc.R114.609248.

[108] X. F. Hul *et al.*, “Rapid up-regulation of mdrl expression by anthracyclines in a classical multidrug-resistant cell line,” *Br J Cancer*, vol. 71, no. 5, pp. 931–936, 1995, doi: 10.1038/bjc.1995.180.

[109] G. Zhou and M. T. Kuo, “Wild-type p53-mediated induction of rat mdr1b expression by the anticancer drug daunorubicin,” *Journal of Biological Chemistry*, vol. 273, pp. 15387–15394, 1998, doi: 10.1074/jbc.273.25.15387.

[110] L. Bao, S. Hazari, S. Mehra, D. Kaushal, K. Moroz, and S. Dash, “Increased expression of P-glycoprotein and doxorubicin chemoresistance of metastatic breast cancer is regulated by miR-298,” *American Journal of Pathology*, vol. 180, no. 6, pp. 2490–2503, Jun. 2012, doi: 10.1016/j.ajpath.2012.02.024.

[111] A. Calcabrini, S. Meschini, A. Stringaro, M. Cianfriglia, G. Arancia, and A. Molinari, “Detection of P-glycoprotein in the nuclear envelope of multidrug resistant cells,” 2000.

[112] W. Szaflarski *et al.*, “Nuclear localization of P-glycoprotein is responsible for protection of the nucleus from doxorubicin in the resistant LoVo cell line,” *Biomedicine and Pharmacotherapy*, vol. 67, pp. 497–502, 2013, doi: 10.1016/j.biopha.2013.03.011.

[113] A. L. Doyle *et al.*, “A multidrug resistance transporter from human MCF-7 breast cancer cells,” *Proc Natl Acad Sci U S A*, vol. 95, pp. 15665–15670, 1998, doi: 10.1073/pnas.95.26.15665.

[114] R. W. Robey, O. Polgar, J. Deeken, K. W. To, and S. E. Bates, “ABCG2: Determining its relevance in clinical drug resistance,” *Cancer and Metastasis Reviews*, vol. 26, pp. 39–57, 2007, doi: 10.1007/s10555-007-9042-6.

[115] W. Yin *et al.*, “The inhibition of ABCB1/MDR1 or ABCG2/BCRP enables doxorubicin to eliminate liver cancer stem cells,” *Sci Rep*, vol. 11, no. 1, pp. 1–13, 2021, doi: 10.1038/s41598-021-89931-9.

[116] S. P. C. Cole *et al.*, “Overexpression of a Transporter Gene in a Multidrug-Resistant Human Lung Cancer Cell Line,” *Science (1979)*, vol. 258, pp. 1650–1654, 1992.

[117] D. Lorendeau *et al.*, “MRP1-dependent Collateral Sensitivity of Multidrug-resistant Cancer Cells: Identifying Selective Modulators Inducing Cellular Glutathione Depletion,” *Curr Med Chem*, vol. 24, no. 12, 2016, doi: 10.2174/0929867324666161118130238.

[118] S. P. C. Cole, “Multidrug resistance protein 1 (MRP1, ABCC1), a ‘Multitasking’ ATP-binding Cassette (ABC) Transporter,” *Journal of Biological Chemistry*, vol. 289, no. 45, pp. 30880–30888, 2014, doi: 10.1074/jbc.R114.609248.

[119] G. L. Beretta and F. Zunino, “Molecular mechanisms of anthracycline activity,” *Top Curr Chem*, vol. 283, pp. 1–19, 2007, doi: 10.1007/128_2007_3.

[120] O. S. Bains, T. A. Grigliatti, R. E. Reid, and K. W. Riggs, “Naturally occurring variants of human aldo-keto reductases with reduced in vitro metabolism of daunorubicin and doxorubicin,” *Journal of Pharmacology and Experimental Therapeutics*, vol. 335, no. 3, pp. 533–545, Dec. 2010, doi: 10.1124/jpet.110.173179.

[121] O. S. Bains, M. J. Karkling, T. A. Grigliatti, R. E. Reid, and K. W. Riggs, “Two Nonsynonymous Single Nucleotide Polymorphisms of Human Carbonyl Reductase 1 Demonstrate Reduced in Vitro Metabolism of Daunorubicin and Doxorubicin,” *Drug Metabolism and Disposition*, vol. 37, no. 5, pp. 1107–1114, May 2009, doi: 10.1124/dmd.108.024711.

[122] T. Zhong, F. Xu, J. Xu, L. Liu, and Y. Chen, “Aldo-keto reductase 1C3 (AKR1C3) is associated with the doxorubicin resistance in human breast cancer via PTEN Loss,” *Biomedicine and Pharmacotherapy*, vol. 69, pp. 317–325, 2015, doi: 10.1016/j.biopha.2014.12.022.

[123] K. Piska, P. Koczurkiewicz, A. Bucki, K. Wójcik-Pszczoła, M. Kołaczkowski, and E. Pękala, “Metabolic carbonyl reduction of anthracyclines — role in cardiotoxicity and cancer resistance. Reducing enzymes as putative targets for novel cardioprotective and chemosensitizing agents,” *Invest New Drugs*, vol. 35, no. 3, pp. 375–385, 2017, doi: 10.1007/s10637-017-0443-2.

[124] D. Edwardson, R. Narendrula, S. Chewchuk, K. Mispel-Beyer, J. Mapletoft, and A. Parissenti, “Role of Drug Metabolism in the Cytotoxicity and Clinical Efficacy of Anthracyclines,” *Curr Drug Metab*, vol. 16, no. 6, pp. 412–426, 2015, doi: 10.2174/1389200216888150915112039.

[125] O. S. Bains *et al.*, “A correlation between cytotoxicity and reductase-mediated metabolism in cell lines treated with doxorubicin and daunorubicin,” *Journal of Pharmacology and Experimental Therapeutics*, vol. 347, no. 2, pp. 375–387, 2013, doi: 10.1124/jpet.113.206805.

[126] A. Mordente, E. Meucci, G. E. Martorana, B. Giardina, and G. Minotti, “Human heart cytosolic reductases and anthracycline cardiotoxicity,” *IUBMB Life*, vol. 52, no. 1–2, pp. 83–88, 2001, doi: 10.1080/15216540252774829.

[127] M. J. Kuffei, M. M. Ames, M. J. Kuffel, and " M M Ames, “Comparative resistance of idarubicin, doxorubicin and their C-13 alcohol metaboUtes in human MDR1 transfected NIH-3T3 Cells,” *Cancer Chemother Pharmacol*, vol. 36, pp. 223–226, 1995.

[128] A. D. Heibein, B. Guo, J. A. Sprowl, D. A. MacLean, and A. M. Parissenti, “Role of aldo-keto reductases and other doxorubicin pharmacokinetic genes in doxorubicin resistance, DNA binding, and subcellular localization,” *BMC Cancer*, vol. 12, 2012, doi: 10.1186/1471-2407-12-381.

[129] K. Piska, P. Koczurkiewicz, A. Bucki, K. Wójcik-Pszczoła, M. Kołaczkowski, and E. Pękala, “Metabolic carbonyl reduction of anthracyclines — role in cardiotoxicity and cancer resistance. Reducing enzymes as putative targets for novel cardioprotective and chemosensitizing agents,” *Invest New Drugs*, vol. 35, no. 3, pp. 375–385, 2017, doi: 10.1007/s10637-017-0443-2.

[130] M. Dean, T. Fojo, and S. Bates, “Tumour stem cells and drug resistance,” *Nat Rev Cancer*, vol. 5, no. 4, pp. 275–284, 2005, doi: 10.1038/nrc1590.

[131] Z. Xu, Y. Zhang, H. Dai, and B. Han, “Epithelial–Mesenchymal Transition-Mediated Tumor Therapeutic Resistance,” *Molecules*, vol. 27, 2022, doi: 10.3390/molecules27154750.

[132] K. Shinlapawittayatorn, S. C. Chattipakorn, and N. Chattipakorn, “The effects of doxorubicin on cardiac calcium homeostasis and contractile function,” Aug. 01, 2022, *Japanese College of Cardiology (Nippon-Sinzobyo-Gakkai)*. doi: 10.1016/j.jjcc.2022.01.001.

[133] S. N. Weingart, L. Zhang, M. Sweeney, and M. Hassett, “Series Drug safety in oncology 1 Chemotherapy medication errors,” 2018. [Online]. Available: www.thelancet.com/oncology

[134] L. K. Booth, R. E. Redgrave, O. Folaranmi, J. H. Gill, and G. D. Richardson, “Anthracycline-induced cardiotoxicity and senescence,” *Frontiers in Aging*, vol. 3, 2022, doi: 10.3389/fragi.2022.1058435.

[135] A. N. Linders, I. B. Dias, T. López Fernández, C. G. Tocchetti, N. Bomer, and P. Van der Meer, “A review of the pathophysiological mechanisms of doxorubicin-induced cardiotoxicity and aging,” *npj Aging*, vol. 10, no. 1, 2024, doi: 10.1038/s41514-024-00135-7.

[136] S. Y. van der Zanden, X. Qiao, and J. Neefjes, “New insights into the activities and toxicities of the old anticancer drug doxorubicin,” *FEBS Journal*, vol. 288, pp. 6095–6111, 2021, doi: 10.1111/febs.15583.

[137] M. Saxena, M. A. Stephens, H. Pathak, and A. Rangarajan, “Transcription factors that mediate epithelial-mesenchymal transition lead to multidrug resistance by upregulating ABC transporters,” *Cell Death Dis*, vol. 2, 2011, doi: 10.1038/cddis.2011.61.

[138] J. Xu, S. Lamouille, and R. Derynck, “TGF-B-induced epithelial to mesenchymal transition,” *Cell Res*, vol. 19, pp. 156–172, Feb. 2009, doi: 10.1038/cr.2009.5.

[139] M. Sabbah *et al.*, “Molecular signature and therapeutic perspective of the epithelial-to-mesenchymal transitions in epithelial cancers,” *Drug Resistance Updates*, vol. 11, no. 4–5, pp. 123–151, 2008, doi: 10.1016/j.drup.2008.07.001.

[140] J. D. Ahlstrom, “Molecular Organization of Cells,” in *Principles of Regenerative Medicine*, Elsevier, 2018, pp. 1–13. doi: 10.1016/B978-0-12-809880-6.00001-1.

[141] Yun Zhang and R. A. Weinberg, “Epithelial-to-mesenchymal transition in cancer: complexity and opportunities,” *Front. Med*, vol. 12, pp. 361–373, 2018, doi: 10.1007/s11684-018-0656-6.Epithelial-to-mesenchymal.

[142] L. Yadav, N. Puri, V. Rastogi, P. Satpute, R. Ahmad, and G. Kaur, “Matrix metalloproteinases and cancer - Roles in threat and therapy,” *Asian Pacific Journal of Cancer Prevention*, vol. 15, pp. 1085–1091, 2014, doi: 10.7314/APJCP.2014.15.3.1085.

[143] M. J. Duffy *et al.*, “The ADAMs family of proteases: New biomarkers and therapeutic targets for cancer?,” *Clin Proteomics*, vol. 8, 2011, doi: 10.1186/1559-0275-8-9.

[144] R. Bacchetti, S. Yuan, and E. Rainero, “ADAMTS Proteases: Their Multifaceted Role in the Regulation of Cancer Metastasis,” *Diseases & Research*, vol. 4, pp. 40–52, 2024, doi: 10.54457/DR.202401004.

[145] S. Banerjee, “Aldo Keto Reductases AKR1B1 and AKR1B10 in Cancer: Molecular Mechanisms and Signaling Networks,” in *Advances in Experimental Medicine and Biology*, vol. 1347, Springer, 2021, pp. 65–82. doi: 10.1007/5584_2021_634.

[146] G. J. Zablocki, P. A. Ruzycki, M. A. Overturf, S. Palla, G. B. Reddy, and J. M. Petrash, “Aldose reductase-mediated induction of epithelium-to-mesenchymal transition (EMT) in lens,” *Chem Biol Interact*, vol. 191, pp. 351–356, 2011, doi: 10.1016/j.cbi.2011.02.005.

[147] T. T. Wu, Y. Y. Chen, H. Y. Chang, Y. H. Kung, C. J. Tseng, and P. W. Cheng, “AKR1B1-induced epithelial–mesenchymal transition mediated by rage-oxidative stress in diabetic cataract lens,” *Antioxidants*, vol. 9, 2020, doi: 10.3390/antiox9040273.

[148] J. Ji *et al.*, “AKR1B1 promotes pancreatic cancer metastasis by regulating lysosome-guided exosome secretion,” *Nano Res*, vol. 15, pp. 5279–5294, 2022, doi: 10.1007/s12274-022-4167-z.

[149] C. Di Benedetto *et al.*, “The p53 tumor suppressor regulates AKR1B1 expression, a metastasis-promoting gene in breast cancer,” *Front Mol Biosci*, vol. 10, 2023, doi: 10.3389/fmolb.2023.1145279.

[150] L. Liu, L. Zhu, Z. Cheng, Y. Sun, Y. Zhou, and J. Cao, “Aberrant expression of AKR1B1 indicates poor prognosis and promotes gastric cancer progression by regulating the AKT-mTOR pathway,” *Aging*, vol. 15, 2023, [Online]. Available: www.aging-us.com

[151] B. Laffin and J. M. Petrash, “Expression of the aldo-ketoreductases AKR1B1 and AKR1B10 in human cancers,” *Front Pharmacol*, vol. 3, 2012, doi: 10.3389/fphar.2012.00104.

[152] X. Wu *et al.*, “AKR1B1 promotes basal-like breast cancer progression by a positive feedback loop that activates the EMT program,” *Journal of Experimental Medicine*, vol. 214, no. 4, pp. 1065–1079, 2017, doi: 10.1084/jem.20160903.

[153] R. Tammali, K. V. Ramana, S. S. Singhal, S. Awasthi, and S. K. Srivastava, “Aldose reductase regulates growth factor-induced cyclooxygenase-2 expression and prostaglandin E2 production in human colon cancer cells,” *Cancer Res*, vol. 66, no. 19, pp. 9705–9713, Oct. 2006, doi: 10.1158/0008-5472.CAN-06-2105.

[154] K. C. Chang and J. M. Petrash, “Aldose reductase mediates transforming growth factor β2 (TGF-β2)–inducedmigration and epithelial-to-mesenchymal transition of lens-derived epithelial cells,” *Invest Ophthalmol Vis Sci*, vol. 56, no. 8, pp. 4198–4210, 2015, doi: 10.1167/iovs.15-16557.

[155] A. Schwab *et al.*, “Polyol pathway links glucose metabolism to the aggressiveness of cancer cells,” *Cancer Res*, vol. 78, no. 7, pp. 1604–1618, 2018, doi: 10.1158/0008-5472.CAN-17-2834.

[156] T. Mosmann, “Rapid Colorimetric Assay for Cellular Growth and Survival: Application to Proliferation and Cytotoxicity Assays,” 1983.

[157] V. Vichai and K. Kirtikara, “Sulforhodamine B colorimetric assay for cytotoxicity screening,” *Nat Protoc*, vol. 1, no. 3, pp. 1112–1116, Aug. 2006, doi: 10.1038/nprot.2006.179.

[158] F. Balestri *et al.*, “L-Idose: An attractive substrate alternative to D-glucose for measuring aldose reductase activity,” *Biochem Biophys Res Commun*, vol. 456, no. 4, pp. 891–895, 2015, doi: 10.1016/j.bbrc.2014.12.054.

[159] R. Rotondo *et al.*, “Human carbonyl reductase 1 as efficient catalyst for the reduction of glutathionylated aldehydes derived from lipid peroxidation,” *Free Radic Biol Med*, vol. 99, pp. 323–332, 2016, doi: 10.1016/j.freeradbiomed.2016.08.015.

[160] C. Federico, F. D. Nicole, P. Rossana, S. Allegrini, C. Marcella, and T. M. Grazia, “IMP-GMP specific cytosolic 5'-nucleotidase regulates nucleotide pool and prodrug metabolism,” *Biochim Biophys Acta Gen Subj*, vol. 1850, no. 7, pp. 1354–1361, Jul. 2015, doi: 10.1016/j.bbagen.2015.03.017.

[161] M. M. Bradford, “A Rapid and Sensitive Method for the Quantitation of Microgram Quantities of Protein Utilizing the Principle of Protein-Dye Binding,” *Anal Biochem*, vol. 72, pp. 248–254, 1976, doi: 10.1016/j.cj.2017.04.003.

[162] L. A. Brennan, R. S. Mcgreal, and M. Kantorow, “Oxidative stress defense and repair systems of the ocular lens,” 2012.

[163] Y. Takamura, Y. Sugimoto, E. Kubo, Y. Takahashi, and Y. Akagi, “Immunohistochemical Study of Apoptosis of Lens Epithelial Cells in Human and Diabetic Rat Cataracts,” 2001.

[164] A. Singh Grewal, S. Bhardwaj, D. Pandita, V. Lather, and B. Singh Sekhon, “Updates on Aldose Reductase Inhibitors for Management of Diabetic Complications and Non-diabetic Diseases,” *Med Chem (Los Angeles)*, vol. 16, pp. 120–162, 2016.

[165] L. jun Yan, “Redox imbalance stress in diabetes mellitus: Role of the polyol pathway,” *Animal Model Exp Med*, vol. 1, pp. 7–13, 2018, doi: 10.1002/ame2.12001.

[166] M. Egi *et al.*, “Blood glucose concentration and outcome of critical illness: The impact of diabetes,” *Crit Care Med*, vol. 36, no. 8, pp. 2249–2255, 2008, doi: 10.1097/CCM.0b013e318181039a.

[167] M. Qu *et al.*, “High glucose induces tau hyperphosphorylation in hippocampal neurons via inhibition of ALKBH5-mediated Dgkh m6A demethylation: a potential mechanism for diabetic cognitive dysfunction,” *Cell Death Dis*, vol. 14, 2023, doi: 10.1038/s41419-023-05909-7.

[168] L. Colombaioni, B. Campanella, R. Nieri, M. Onor, E. Benedetti, and E. Bramanti, “Time-dependent influence of high glucose environment on the metabolism of neuronal immortalized cells,” *Anal Biochem*, vol. 645, 2022, doi: 10.1016/j.ab.2022.114607.

[169] T. Jayakumar *et al.*, “Brazilin ameliorates high glucose-induced vascular inflammation via inhibiting ROS and CAMs production in human umbilical vein endothelial cells,” *Biomed Res Int*, vol. 2014, 2014, doi: 10.1155/2014/403703.

[170] P. González, P. Lozano, G. Ros, and F. Solano, “Hyperglycemia and Oxidative Stress: An Integral, Updated and Critical Overview of Their Metabolic Interconnections,” *Int J Mol Sci*, vol. 24, no. 11, 2023, doi: 10.3390/ijms24119352.

[171] K. V Ramana, B. Friedrich, S. Srivastava, A. Bhatnagar, and S. K. Srivastava, “Activation of Nulcear Factor-B by Hyperglycemia in Vascular Smooth Muscle Cells Is Regulated by Aldose Reductase,” 2004, [Online]. Available: http://diabetesjournals.org/diabetes/article-pdf/53/11/2910/376572/zdb01104002910.pdf

[172] K. V Ramana and S. K. Srivastava, “Mediation of aldose reductase in lipopolysaccharide-induced inflammatory signals in mouse peritoneal macrophages,” *Cytokine*, vol. 36, pp. 115–122, 2006.

[173] H. Han, J.-K. Kang, K. J. Ahn, and C.-G. Hyun, “DMSO Alleviates LPS-Induced Inflammatory Responses in RAW264.7 Macrophages by Inhibiting NF-κB and MAPK Activation,” *BioChem*, vol. 3, pp. 91–101, 2023, doi: 10.3390/biochem3020007.

[174] I. Elisia *et al.*, “DMSO represses inflammatory cytokine production from human blood cells and reduces autoimmune arthritis,” *PLoS One*, vol. 11, 2016, doi: 10.1371/journal.pone.0152538.

[175] L. De Abreu Costa *et al.*, “Dimethyl sulfoxide (DMSO) decreases cell proliferation and TNF-α, IFN-, and IL-2 cytokines production in cultures of peripheral blood lymphocytes,” *Molecules*, vol. 22, 2017, doi: 10.3390/molecules22111789.

[176] K. V. Ramana and S. K. Srivastava, “Aldose reductase: A novel therapeutic target for inflammatory pathologies,” *International Journal of Biochemistry and Cell Biology*, vol. 42, pp. 17–20, 2010, doi: 10.1016/j.biocel.2009.09.009.

[177] K. V Ramana, U. C. S. Yadav, W. J. Calhoun, and S. K. Srivastava, “Current Prospective of Aldose Reductase Inhibition in the Therapy of Allergic Airway Inflammation in Asthma,” *Curr Mol Med*, vol. 11, pp. 599–608, 2011.

[178] U. C. S. Yadav, K. V. Ramana, L. Aguilera-Aguirre, I. Boldogh, H. A. Boulares, and S. K. Srivastava, “Inhibition of aldose reductase prevents experimental allergic airway inflammation in mice,” *PLoS One*, vol. 4, 2009, doi: 10.1371/journal.pone.0006535.

[179] K. V. Ramana, B. Friedrich, A. Bhatnagar, and S. K. Srivastava, “Aldose reductase mediates cytotoxic signals of hyperglycemia and TNF-alpha in human lens epithelial cells.,” *The FASEB journal : official publication of the Federation of American Societies for Experimental Biology*, vol. 17, no. 2, pp. 315–317, 2003, doi: 10.1096/fj.02-0568fje.

[180] J. Hofman, A. Skarka, J. Havrankova, and V. Wsol, “Pharmacokinetic interactions of breast cancer chemotherapeutics with human doxorubicin reductases,” *Biochem Pharmacol*, vol. 96, no. 3, pp. 168–178, Jul. 2015, doi: 10.1016/j.bcp.2015.05.005.

[181] O. S. Bains, R. H. Takahashi, T. A. Pfeifer, T. A. Grigliatti, R. E. Reid, and K. W. Riggs, “Two allelic variants of aldo-keto reductase 1A1 exhibit reduced in vitro metabolism of daunorubicin,” *Drug Metabolism and Disposition*, vol. 36, no. 5, pp. 904–910, May 2008, doi: 10.1124/dmd.107.018895.

[182] Z. Teo *et al.*, “Elevation of adenylate energy charge by angiopoietin-like 4 enhances epithelial-mesenchymal transition by inducing 14-3-3γ expression,” *Oncogene*, vol. 36, pp. 6408–6419, 2017, doi: 10.1038/onc.2017.244.

[183] R. B. Cejas, K. Petrykey, Y. Sapkota, and P. W. Burridge, “Anthracycline Toxicity: Light at the End of the Tunnel?,” *Annual Review of Pharmacology and Toxicology Downloaded from www.annualreviews.org. Guest*, vol. 21, p. 42, 2024, doi: 10.1146/annurev-pharmtox-022823.

[184] A. Vaidyanathan *et al.*, “ABCB1 (MDR1) induction defines a common resistance mechanism in paclitaxel- and olaparib-resistant ovarian cancer cells,” *Br J Cancer*, vol. 115, pp. 431–441, 2016, doi: 10.1038/bjc.2016.203.

[185] J. Węsierska-Gądek, “Major contribution of the multidrug transporter p-glycoprotein to reduced susceptibility of poly(ADP-ribose) polymerase-1 knock-out cells to doxorubicin action,” *J Cell Biochem*, vol. 95, pp. 1012–1028, 2005, doi: 10.1002/jcb.20467.

[186] S. Goto, T. Kawabata, and T. S. Li, “Enhanced Expression of ABCB1 and Nrf2 in CD133-Positive Cancer Stem Cells Associates with Doxorubicin Resistance,” *Stem Cells Int*, vol. 2020, 2020, doi: 10.1155/2020/8868849.

[187] J. E. Jaspers *et al.*, “BRCA2-deficient sarcomatoid mammary tumors exhibit multidrug resistance,” *Cancer Res*, vol. 75, pp. 732–741, 2015, doi: 10.1158/0008-5472.CAN-14-0839.

[188] S. P. C. Cole *et al.*, “Overexpression of a Transporter Gene in a Multidrug-Resistant Human Lung Cancer Cell Line,” *Science (1979)*, vol. 258, pp. 1650–1654, 1992.

[189] P. Borst, C. De Wolf, and K. Van De Wetering, “Multidrug resistance-associated proteins 3, 4, and 5,” *Pflugers Arch*, vol. 453, pp. 661–673, 2007, doi: 10.1007/s00424-006-0054-9.

[190] D. M. Townsend and K. D. Tew, “The role of glutathione-S-transferase in anti-cancer drug resistance,” *Oncogene*, vol. 22, pp. 7369–7375, Oct. 2003, doi: 10.1038/sj.onc.1206940.

[191] K. W. Ang, S. R. Ji, A. Bhathena, C. Lee, and D. S. Riddick, “Glutathione S-transferases in wild-type and doxorubicin-resistant MCF-7 human breast cancer cell lines,” *Xenobiotica*, vol. 29, pp. 155–170, 1999, [Online]. Available: www.tandf.co.uk}

[192] G. Gaudiano *et al.*, “Lack of Glutathione Conjugation to Adriamycin in Human Breast Cancer MCF-7/DOX Cells,” *Biochem Pharmacol*, vol. 60, pp. 1915–1923, 2000.

[193] J. P. Shaw and I.-N. Chou, “Elevation of lntracellular Glutathione Content Associated With Mitogenic Stimulation of Quiescent Fibroblasts,” *J Cell Physiol*, vol. 129, pp. 193–198, 1986.

[194] F. Balestri, R. Moschini, U. Mura, M. Cappiello, and A. Del Corso, “In Search of Differential Inhibitors of Aldose Reductase,” *Biomolecules*, vol. 12, 2022, doi: 10.3390/biom12040485.

[195] J. Li Huang, M. Oshi, I. Endo, and K. Takabe, “Clinical relevance of stem cell surface markers CD133, CD24, and CD44 in colorectal cancer,” *Am J Cancer Res*, vol. 11, pp. 5141–5154, 2021, [Online]. Available: www.ajcr.us/

[196] T. E. Hardingham and A. J. Fosang, “Proteoglycans: many forms and many functions,” *The FASEB Journal*, vol. 6, pp. 861–870, 1992.

[197] L. Schaefer and R. M. Schaefer, “Proteoglycans: From structural compounds to signaling molecules,” Jan. 2010. doi: 10.1007/s00441-009-0821-y.

[198] Y. Matsuzaka and R. Yashiro, “Classification and Molecular Functions of Heparan Sulfate Proteoglycans and Their Molecular Mechanisms with the Receptor,” *Biologics*, vol. 4, no. 2, pp. 105–129, Mar. 2024, doi: 10.3390/biologics4020008.

[199] C. J. Handley, T. Samiric, and M. Z. Ilic, “Structure, Metabolism, and Tissue Roles of Chondroitin Sulfate Proteoglycans,” 2006. doi: 10.1016/S1054-3589(05)53010-2.

[200] E. Bedini, M. M. Corsaro, A. Fernández-Mayoralas, and A. Iadonisi, “Chondroitin, Dermatan, Heparan, and Keratan Sulfate: Structure and Functions,” in *Extracellular Sugar-Based Biopolymers Matrices*, vol. 12, 2019, pp. 187–233. doi: 10.1007/978-3-030-12919-4_5.

[201] S. Santamaria and R. De Groot, “ADAMTS proteases in cardiovascular physiology and disease: ADAMTS, cardiovascular roles,” *Open Biol*, vol. 10, no. 12, 2020, doi: 10.1098/rsob.200333.

[202] R. P. T. Somerville *et al.*, “Characterization of ADAMTS-9 and ADAMTS-20 as a distinct ADAMTS subfamily related to Caenorhabditis elegans GON-1,” *Journal of Biological Chemistry*, vol. 278, no. 11, pp. 9503–9513, 2003, doi: 10.1074/jbc.M211009200.

[203] R. Blelloch, S. S. Anna-Arriola, D. Gao, Y. Li, J. Hodgkin, and J. Kimble, “The gon-1 gene is required for gonadal morphogenesis in Caenorhabditis elegans,” *Dev Biol*, vol. 216, no. 1, pp. 382–393, 1999, doi: 10.1006/dbio.1999.9491.

[204] A. Ismat, A. M. Cheshire, and D. J. Andrew, “The secreted AdamTS-A metalloprotease is required for collective cell migration,” *Development*, vol. 140, no. 9, pp. 1981–1993, May 2013, doi: 10.1242/dev.087908.

[205] K. A. Jungers, C. Le Goff, R. P. T. Somerville, and S. S. Apte, “Adamts9 is widely expressed during mouse embryo development,” *Gene Expression Patterns*, vol. 5, no. 5, pp. 609–617, 2005, doi: 10.1016/j.modgep.2005.03.004.

[206] C. B. Kern *et al.*, “Reduced versican cleavage due to Adamts9 haploinsufficiency is associated with cardiac and aortic anomalies,” *Matrix Biology*, vol. 29, no. 4, pp. 304–316, 2010, doi: 10.1016/j.matbio.2010.01.005.

[207] S. Santamaria *et al.*, “Exosites in Hypervariable Loops of ADAMTS Spacer Domains control Substrate Recognition and Proteolysis,” *Sci Rep*, vol. 9, no. 1, pp. 1–12, 2019, doi: 10.1038/s41598-019-47494-w.

[208] S. Santamaria, D. R. Martin, X. Dong, K. Yamamoto, S. S. Apte, and J. Ahnström, “Post-translational regulation and proteolytic activity of the metalloproteinase ADAMTS8,” *Journal of Biological Chemistry*, vol. 297, no. 5, pp. 1–17, 2021, doi: 10.1016/j.jbc.2021.101323.

[209] S. J. Foulcer *et al.*, “Determinants of versican-v1 proteoglycan processing by the metalloproteinase ADAMTS5,” *Journal of Biological Chemistry*, vol. 289, no. 40, pp. 27859–27873, Oct. 2014, doi: 10.1074/jbc.M114.573287.

[210] M. M. Fowkes, L. Troeberg, P. E. Brennan, T. L. Vincent, M. Meldal, and N. H. Lim, “Development of Selective ADAMTS-5 Peptide Substrates to Monitor Proteinase Activity,” *J Med Chem*, vol. 66, no. 5, pp. 3522–3539, Mar. 2023, doi: 10.1021/acs.jmedchem.2c02090.

[211] S. Santamaria *et al.*, “Antibody-based exosite inhibitors of ADAMTS-5 (aggrecanase-2),” *Biochemical Journal*, vol. 471, no. 3, pp. 391–401, 2015, doi: 10.1042/BJ20150758.

[212] C. Kiani, L. Chen, Y. J. Wu, A. J. Yee, and B. B. Yang, “Structure and function of aggrecan,” *Cell Res*, vol. 12, no. 1, pp. 19–32, 2002, [Online]. Available: http://www.cell-research.com

[213] C. D. Koch, C. M. Lee, and S. S. Apte, “Aggrecan in Cardiovascular Development and Disease,” Nov. 01, 2020, *SAGE Publications Ltd*. doi: 10.1369/0022155420952902.

[214] H. Oshita, J. D. Sandy, K. Suzuki, A. Akaike, T. Bai, and K. Shimizu, “Mature bovine articular cartilage contains abundant aggrecan that is C-terminally truncated at Ala719-Ala720, a site which is readily cleaved by m-calpain,” *Biochemistry Journal*, vol. 382, pp. 253–259, 2004.

[215] F. M. Rogerson *et al.*, “ADAMTS-9 in mouse cartilage has aggrecanase activity that is distinct from ADAMTS-4 and ADAMTS-5,” *Int J Mol Sci*, vol. 20, no. 3, Feb. 2019, doi: 10.3390/ijms20030573.

[216] Minns Alexander Frederick and Santamaria Salvatore, *Determination of Versikine Levels by Enzyme-Linked Immunosorbent Assay (ELISA).*, vol. 2747. 2023.

[217] A. F. Minns, Y. Qi, K. Yamamoto, K. Lee, J. Ahnström, and S. Santamaria, “The C-terminal domains of ADAMTS1 contain exosites involved in its proteoglycanase activity,” *Journal of Biological Chemistry*, vol. 299, no. 4, Apr. 2023, doi: 10.1016/j.jbc.2023.103048.

[218] A. B. Hamze, S. Wei, H. Bahudhanapati, S. Kota, K. R. Acharya, and K. Brew, “Constraining specificity in the N-domain of tissue inhibitor of metalloproteinases-1; gelatinase-selective inhibitors,” *Protein Science*, vol. 16, no. 9, pp. 1905–1913, Sep. 2007, doi: 10.1110/ps.072978507.

[219] C. Gendron, M. Kashiwagi, C. Hughes, B. Caterson, and H. Nagase, “TIMP-3 inhibits aggrecanase-mediated glycosaminoglycan release from cartilage explants stimulated by catabolic factors,” *FEBS Lett*, vol. 555, no. 3, pp. 431–436, Dec. 2003, doi: 10.1016/S0014-5793(03)01295-X.

[220] G. Hashimoto, T. Aoki, H. Nakamura, K. Tanzawa, and Y. Okada, “Inhibition of ADAMTS4 (aggrecanase-1) by tissue inhibitors of metalloproteinases (TIMP-1, 2, 3 and 4),” *FEBS Lett*, vol. 494, no. 3, pp. 192–195, Apr. 2001, doi: 10.1016/S0014-5793(01)02323-7.

[221] K. Brew and H. Nagase, “The tissue inhibitors of metalloproteinases (TIMPs): An ancient family with structural and functional diversity,” Jan. 2010. doi: 10.1016/j.bbamcr.2010.01.003.

[222] M. K. Majumdar *et al.*, “Double-knockout of ADAMTS-4 and ADAMTS-5 in mice results in physiologically normal animals and prevents the progression of osteoarthritis,” *Arthritis Rheum*, vol. 56, pp. 3670–3674, 2007, doi: 10.1002/art.23027.

[223] T. Manon-Jensen, Y. Itoh, and J. R. Couchman, “Proteoglycans in health and disease: The multiple roles of syndecan shedding,” *FEBS Journal*, vol. 277, no. 19, pp. 3876–3889, 2010, doi: 10.1111/j.1742-4658.2010.07798.x.

[224] E. Okina, T. Manon-Jensen, J. R. Whiteford, and J. R. Couchman, “Syndecan proteoglycan contributions to cytoskeletal organization and contractility,” *Scand J Med Sci Sports*, vol. 19, pp. 479–489, 2009, doi: 10.1111/j.1600-0838.2009.00941.x.

[225] F. Gondelaud and S. Ricard-Blum, “Structures and interactions of syndecans,” *FEBS Journal*, vol. 286, pp. 2994–3007, 2019, doi: 10.1111/febs.14828.

[226] M. E. Strand *et al.*, “Shedding of syndecan-4 promotes immune cell recruitment and mitigates cardiac dysfunction after lipopolysaccharide challenge in mice,” *J Mol Cell Cardiol*, vol. 88, pp. 133–144, 2015, doi: 10.1016/j.yjmcc.2015.10.003.

[227] S. Gopal, “Syndecans in Inflammation at a Glance,” *Front Immunol*, vol. 11, 2020, doi: 10.3389/fimmu.2020.00227.

[228] A. Elfenbein and M. Simons, “Syndecan-4 signaling at a glance,” *J Cell Sci*, vol. 126, no. 17, pp. 3799–3804, 2013, doi: 10.1242/jcs.124636.

[229] J. Lambert *et al.*, “ADAMTS-1 and syndecan-4 intersect in the regulation of cell migration and angiogenesis,” *J Cell Sci*, vol. 133, 2020, doi: 10.1242/jcs.235762.

[230] J. Kreuger, D. Spillmann, J. Li, and U. Lindahl, “Interactions between heparan sulfate and proteins: the concept of specifi city,” *Journal of Biological Chemistry*, vol. 174, pp. 323–327, 2006, doi: 10.1074/jbc.M600806200.

[231] A. Woods and J. R. Couchman, “Syndecan-4 and focal adhesion function,” *Curr Opin Cell Biol*, vol. 13, pp. 578–583, 2001.

[232] S. A. Wilcox-Adelman, F. Denhez, and P. F. Goetinck, “Syndecan-4 modulates focal adhesion kinase phosphorylation,” *Journal of Biological Chemistry*, vol. 277, pp. 32970–32977, 2002, doi: 10.1074/jbc.M201283200.

[233] E. J. Nam and P. W. Park, “Shedding of cell membrane-bound proteoglycans,” in *Methods in Molecular Biology*, vol. 836, 2012, ch. 19, pp. 291–305. doi: 10.1007/978-1-61779-498-8_19.

[234] T. Pap and J. Bertrand, “Syndecans in cartilage breakdown and synovial inflammation,” *Nat Rev Rheumatol*, vol. 9, pp. 43–55, 2013, doi: 10.1038/nrrheum.2012.178.

[235] C. Y. Fears and A. Woods, “The role of syndecans in disease and wound healing,” *Matrix Biology*, vol. 25, pp. 443–456, 2006, doi: 10.1016/j.matbio.2006.07.003.

[236] A. N. Alexopoulou, H. A. B. Multhaupt, and J. R. Couchman, “Syndecans in wound healing, inflammation and vascular biology,” *International Journal of Biochemistry and Cell Biology*, vol. 39, pp. 505–528, 2007, doi: 10.1016/j.biocel.2006.10.014.

[237] C. Jessica Bertrand, J. Bertrand, and M. Bollmann, “Soluble syndecans: biomarkers for diseases and therapeutic options,” *Br J Pharmacol*, vol. 176, pp. 67–81, 2019, doi: 10.1111/bph.v176.1/issuetoc.

[238] M. S. Brown, J. Ye, R. B. Rawson, and J. L. Goldstein, “Regulated Intramembrane Proteolysis: A Control Mechanism Conserved from Bacteria to Humans,” *Cell*, vol. 100, pp. 391–398, 2000.

[239] T. Manon-Jensen, H. A. B. Multhaupt, and J. R. Couchman, “Mapping of matrix metalloproteinase cleavage sites on syndecan-1 and syndecan-4 ectodomains,” *FEBS Journal*, vol. 280, no. 10, pp. 2320–2331, 2013, doi: 10.1111/febs.12174.

[240] J. C. Rodríguez-Manzaneque *et al.*, “Cleavage of syndecan-4 by ADAMTS1 provokes defects in adhesion,” *International Journal of Biochemistry and Cell Biology*, vol. 41, pp. 800–810, 2009, doi: 10.1016/j.biocel.2008.08.014.

[241] F. Echtermeyer *et al.*, “Syndecan-4 regulates ADAMTS-5 activation and cartilage breakdown in osteoarthritis,” *Nat Med*, vol. 15, pp. 1072–1076, 2009, doi: 10.1038/nm.1998.

[242] G. Gao, A. Plaas, V. P. Thompson, S. Jin, F. Zuo, and J. D. Sandy, “ADAMTS4 (Agrecanase-1) Activation on the Cell Surface Involves C-terminal Cleavage by Glycosylphosphatidyl Inositol-anchored Membrane Type 4-Matrix Metalloproteinase and Binding of the Activated Proteinase to Chondroitin Sulfate and Heparan Sulfate on Syndendecan-1,” *J Biol Chem*, vol. 279, pp. 10042–10051, 2004.

[243] E. H. M. Kerkvliet, I. D. C. Jansen, T. A. M. Schoenmaker, A. J. P. Docherty, W. Beertsen, and V. Everts, “Low molecular weight inhibitors of matrix metalloproteinases can enhance the expression of matrix metalloproteinase-2 (Gelatinase A) without inhibiting its activation,” *Cancer*, vol. 97, pp. 1582–1588, 2003, doi: 10.1002/cncr.11193.

[244] E. Nuti *et al.*, “Arylsulfonamide inhibitors of aggrecanases as potential therapeutic agents for osteoarthritis: Synthesis and biological evaluation,” *Eur J Med Chem*, vol. 62, pp. 379–394, 2013, doi: 10.1016/j.ejmech.2012.12.058.

[245] F. Gondelaud *et al.*, “Extended disorder at the cell surface: The conformational landscape of the ectodomains of syndecans,” *Matrix Biol Plus*, vol. 12, 2021, doi: 10.1016/j.mbplus.2021.100081.

[246] B. Seminotti, M. Grings, P. Tucci, G. Leipnitz, and L. Saso, “Nuclear Factor Erythroid-2-Related Factor 2 Signaling in the Neuropathophysiology of Inherited Metabolic Disorders,” *Front Cell Neurosci*, vol. 15, 2021, doi: 10.3389/fncel.2021.785057.

[247] A. P. Shanbhag and P. Bhowmik, “Cancer to Cataracts: The Mechanistic Impact of Aldo-Keto Reductases in Chronic Diseases,” *Yale J Biol Med*, vol. 97, pp. 179–204, 2024, doi: 10.59249/VTBV6559.

[248] A. P. Rolo and C. M. Palmeira, “Diabetes and mitochondrial function: Role of hyperglycemia and oxidative stress,” *Toxicol Appl Pharmacol*, vol. 212, no. 2, pp. 167–178, Apr. 2006, doi: 10.1016/j.taap.2006.01.003.

[249] C. Peng, Y. Ouyang, N. Lu, and N. Li, “The NF-κB Signaling Pathway, the Microbiota, and Gastrointestinal Tumorigenesis: Recent Advances,” *Front Immunol*, vol. 11, 2020, doi: 10.3389/fimmu.2020.01387.

[250] M. Dean, T. Fojo, and S. Bates, “Tumour stem cells and drug resistance,” *Nat Rev Cancer*, vol. 5, no. 4, pp. 275–284, 2005, doi: 10.1038/nrc1590.

[251] J. Jayachandran, H. Srinivasan, and K. P. Mani, “Molecular mechanism involved in epithelial to mesenchymal transition,” *Arch Biochem Biophys*, vol. 710, 2021, doi: 10.1016/j.abb.2021.108984.

[252] I. Desanlis, H. L. Felstead, D. R. Edwards, and G. N. Wheeler, “ADAMTS9, a member of the ADAMTS family, in Xenopus development,” *Gene Expression Patterns*, vol. 29, no. May, pp. 72–81, 2018, doi: 10.1016/j.gep.2018.06.001.

[253] F. Shaik, M. J. M. Balderstone, S. Arokiasamy, and J. R. Whiteford, “Roles of Syndecan-4 in cardiac injury and repair,” *International Journal of Biochemistry and Cell Biology*, vol. 146, 2022, doi: 10.1016/j.biocel.2022.106196.

ACKNOWLEDGMENT

This thesis is the result of the hard work and passion that have accompanied me over the past three years. None of this would have been possible without the support and motivation I received from my supervisor. Thank you, Roby, you have been much more than a tutor: you have made these three years an unforgettable experience. I will always treasure your valuable advice, and it will not be easy to lose the enthusiasm for this work that you so wonderfully inspired in me.

A heartfelt thanks also goes to the entire biochemistry group, my second family over these three years. Each of you has contributed significantly to this work, and for that, I am deeply grateful.

Thank you to Salvo and his team for welcoming me and making me feel at home during the months spent in Guildford. This journey would not have been the same without meeting you.

An enormous thank you goes to my family, to my mom, dad, Ale, Franci, Pippo, to tato and Marta, and my amazing grandmothers. No one knows better than you the effort and sacrifices this journey has required. If I have reached this goal, it is entirely thanks to you, and as long as your eyes continue to shine with pride at my achievements, I will not stop.

Finally, thank you to an extraordinary person who stands by my side despite my hectic and chaotic life. Thank you, who, despite countless challenges, always make me feel like a priority, who listen to my fears, guide me in my choices, celebrate my victories, and support me in difficult moments. Thank you, because when something goes wrong, all it takes is looking into your eyes to feel happy again. Thank you France, since you've been in my life, everything has been brighter.

Questa tesi è il frutto del duro lavoro e della passione che hanno accompagnato gli ultimi tre anni. Nulla di tutto questo sarebbe stato possibile senza il sostegno e la motivazione che ho ricevuto dalla mia supervisor, che ringrazio di cuore. Grazie, Roby, sei stata molto più di una tutor: hai reso questi tre anni un'esperienza indimenticabile. Porterò sempre con me i tuoi preziosi consigli, e non sarà facile perdere l'entusiasmo per questo lavoro che hai saputo trasmettermi.

Grazie di cuore anche a tutto il gruppo di biochimici, la mia seconda famiglia in questi tre anni. Ognuno di voi ha contribuito in modo significativo a questo lavoro, e di questo vi sono profondamente grata.

Grazie a Salvo e al suo gruppo, per avermi accolta e fatta sentire a casa durante i mesi trascorsi a Guildford. Questo percorso non sarebbe stato lo stesso senza avervi incontrato.

Un enorme grazie va alla mia famiglia, a mamma, babbo, Ale, Franci e Pippo, a tato e Marta e alle mie super nonne. Nessuno meglio di voi conosce la fatica e i sacrifici che questo percorso ha comportato. Se sono arrivata fino a qui è solo merito vostro e finché i vostri occhi continueranno a brillare di fronte ai miei successi, io non mi fermerò.

Infine, grazie ad una persona straordinaria che riesce a stare al mio fianco nonostante la mia vita frenetica e sconclusionata. Grazie a te che, nonostante le mille sfide, riesci sempre a farmi sentire al primo posto, che ascolti le mie paure, che mi guidi nelle scelte, che esulti con me per le vittorie e mi sostieni nei momenti difficili. Grazie, perché quando qualcosa va storto, mi basta guardarti negli occhi per ritrovare serenità. Grazie France, da quando sei con me tutto è più luminoso.